Thermal Conductivity Enhancement by Optical Phonon Sub-Band Engineering of Nanostructures Based on C and BN

DARPA CONTRACT MDA972-02-C-0044

SCIENTIFIC AND TECHNICAL REPORT

FINAL REPORT

Submitted by

NANOTECH INSTITUTE
UNIVERSITY OF TEXAS AT DALLAS (UTD)

Submitted To:
Dr. Leonard J. Buckley
DARPA/DSO Program Manager
Lbuckley@darpa.mil

Jim Troutman
Contracting officer
jtroutman@darpa.mil

NanoTech Institute, UTD, MS:BE26, 2601 N. Floyd Rd., Richardson, TX 75083

Report Documentation Page

Form Approved
OMB No. 0704-0188

1. REPORT DATE	2. REPORT TYPE	3. DATES COVERED
01 SEP 2005	**N/A**	**-**

4. TITLE AND SUBTITLE	5a. CONTRACT NUMBER
Thermal Conductivity Enhancement by Optical Phonon Sub-Band Engineering of Nanostructures Based on C and BN	5b. GRANT NUMBER
	5c. PROGRAM ELEMENT NUMBER
6. AUTHOR(S)	5d. PROJECT NUMBER
	5e. TASK NUMBER
	5f. WORK UNIT NUMBER
7. PERFORMING ORGANIZATION NAME(S) AND ADDRESS(ES) **Nanotech Institute University Of Texas At Dallas (UTD) Richardson, TX 75083**	8. PERFORMING ORGANIZATION REPORT NUMBER
9. SPONSORING/MONITORING AGENCY NAME(S) AND ADDRESS(ES)	10. SPONSOR/MONITOR'S ACRONYM(S)
	11. SPONSOR/MONITOR'S REPORT NUMBER(S)

12. DISTRIBUTION/AVAILABILITY STATEMENT
Approved for public release, distribution unlimited

13. SUPPLEMENTARY NOTES
See also ADM001801., The original document contains color images.

14. ABSTRACT

15. SUBJECT TERMS

16. SECURITY CLASSIFICATION OF:			17. LIMITATION OF ABSTRACT	18. NUMBER OF PAGES	19a. NAME OF RESPONSIBLE PERSON
a. REPORT	b. ABSTRACT	c. THIS PAGE			
unclassified	**unclassified**	**unclassified**	**UU**	**109**	

FINAL REPORT

TABLE OF CONTENTS

Section		Page
1. THEORY, MODELING AND DESIGN …….		**5**
1.1. Thermal Conductivity in CNT Bundles		
1.1.1.	**Introduction ……...**	**5**
1.1.2.	**Scattering problems ……..**	**5**
1.1.3.	**Thermal conductivity ……...**	**7**
1.1.4.	**Conclusions ……**	**8**
1.1.5.	**References …….**	**9**
1.2. Theory of Thermal Conductivity by Polaritons…….		**10**
1.3. Modeling of Phonons and Heat Transfer in Carbon Nanostructures …….		**11**
1.3.1.	**Phonon dynamics and thermal properties of zigzag and armchair carbon nanotubes …….**	**11**
	a. Phonon dynamics and thermal properties of zigzag carbon nanotubes…….	**11**
	b. Phonon dynamics and thermal properties of free armchair carbon nanotubes…….	**30**
1.3.2.	**Carbon heat radiators in polymer surroundings ……**	**52**
	a. Dynamics of carbon tubes laterally in contact with external medium ……	**53**
	b. Phonon dynamics of carbon tubes embraced by polymer molecule ……...	**57**
1.3.3.	**Sound propagation in molecular nets …….**	**59**

a. Phonons and Hypersound in Low-dimensional Molecular Nets ……. 60

b. Sound Boundary Conditions ……... 64

c. The Hypersound Frequency Bands in Periodic Molecular Nets ……. 68

d. Summary ……... 73

1.3.4. Conclusions ……... 73

1.3.5. References ……. 75

2. SYNTHESIS OF NANOSTRUCTURE……. 76

2.1. Synthesis of Zeolite Encapsulated Nanotubes …… 76

2.2. Synthesis of Conjugated Polymer-CNT Complexes ……. 84

3. CHARACTERIZATION AND OPTIMIZATION OF PHONON THERMAL SPECTRA, CONDUCTIVITY AND SUPERCONDUCTIVITY……. 91

3.1. Thermal Conductivity Measurements on Nanocomposites with CNTs…….. 91

3.1.1. Comparative method in PPMS……. 91

3.1.2. Tunable thermal conductivity in carbon nanotube paper……. 93

a. Experiment……. 93

3.1.3. References…….. 98

3.2. Thermal Conductivity of Carbon Inverse Opals…… 99

3.2.1. Experiment……. 100

3.2.2. Results and Discussion…….. 100

3.2.3. Conclusion…….. 106

3.2.4. References…… 107

4. SUMMARY AND CONCLUSIONS……..… 108

4.1. Summary on Carbon Nanotubes.....…… 108

4.2. Conclusions on Thermal Conductivity Enhancement…… 108

5. APPENDICES

5.1. Theory of Thermal Conductivity by Polaritons

5.2. "Vibrations of single-wall carbon nanotube: lattice models and low-frequency dispersion"

5.3. "Simple empirical model for vibrational spectra of single-wall carbon nanotubes"

5.4. “Phonon-Polariton Physics: Thermal Conductivity, Phonon-Polariton Lasers and Phonon Transistors in Nanostructures”

5.5. “Phonons and Thermal Transport in Carbon Nanotube Systems”

Chapter 1: THEORY, MODELING AND DESIGN

1.1 Thermal Conductivity in CNT Bundles

1.1.1. Introduction

It is expected that a single-wall carbon nanotube (SWCN) is a very promising object for creation of metamaterials with a high thermal conductivity (TC) [1,2]. The first reason for this expectation is that carbon-based materials, like diamond, have the largest known TC and, the second reason is a molecular perfection of the SWCNs [1]. However, to the best of my knowledge, the highest TC ever observed in SWCN bundles at room temperature is about 220 W/mK and it is ten times smaller than the TC of the natural diamond [3]. This highest result has been reported by Hone et al. [4] for a bulk sample of magnetically aligned nanotubes. The aligned SWCNs form a bundle in which all tubes have a preferable orientation in some direction. Hone et al. showed that the TC of the aligned SWCNs is strongly anisotropic with the largest value in the direction of the alignment.

The enhancement of the TC due to the alignment has been observed also by Zhou et al. [5] and by Choi et al. [6], but the absolute values of the reported TC have been significantly smaller than in [4].

There are many theoretical works on TC of the SWCNs. Some computational ones [7-10] are made by molecular dynamics simulations. The results of these simulations have different values and different T-dependences. They predict mostly very high values of the room temperature TC (for example 6000 in [7].)

Evidently, the main problem of all these works is the small size of the array that can be simulated. There are also some different analytical approaches to the problem [11,12] and wonderful reviews [13-15].

The purpose of this research is to estimate the maximum TC value of aligned nanotubes taking into account that they do necessarily consist of segments with a finite length. It is well known, that tubes in ropes are not infinitely long, but have brakes, because each method of synthesis is able to create separated tubes of only a certain length. It is believed that this length is of the order of a few microns (see [16] and references therein). Then, due to Van der Waals forces, the tubes stick together and create bundles wherein the end of a tube has no chance to make a strong chemical bond to the end of a neighboring tube.

There are many experiments that show that tubes inside bundles have free ends. The idea here is to argue that this effect may be responsible for the relatively low TC as compared to crystalline carbon materials.

1.1.2. Scattering problems

Consider a bundle of nanotubes perfectly aligned; each segment has a finite length with an average value L. The nanotubes are organized in an ideal triangular lattice with six nearest neighbors [17]. The cross section in a plane perpendicular to the nanotubes is shown in Fig.1.1(a). The cuts in each line of the nanotubes have random positions. Thus, on the

length of each segment there are in average six cuts of its nearest neighbors. A homogeneous interaction between infinite tubes does not cause the loss of the phonon momentum. However, a phonon flux has to overcome the openings between the segments at the termination points of each nanotube segment. Assume that these openings are so large that a jump of flux occurs with an assistance of all six neighboring rows of the tubes as shown in Fig.1.1(b). A slightly different mechanism of momentum scattering appears in a given nanotube ("0'') if one of the neighboring nanotubes has a termination point as shown in Fig.1.1(c).

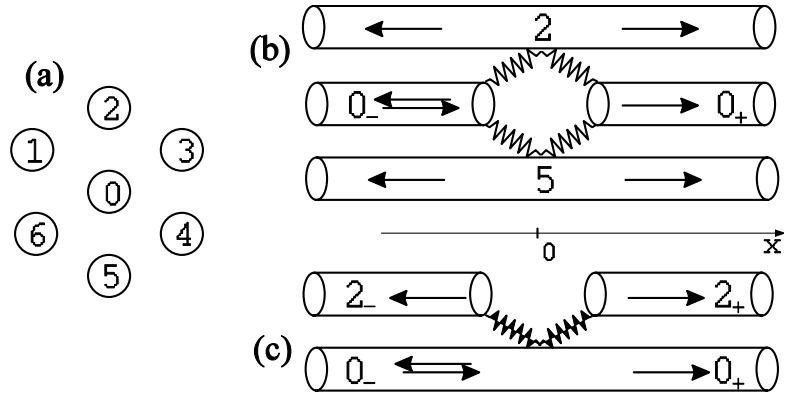

Fig. 1.1: (a) The cross-section of the bundle that shown a nanotube ``0'' and its nearest neighbors.
(b) The first scattering problem - cross-section by the plane of nanotubes 2-0-5. The wave incident from 0_- reflects backward and transmits through the opening into 0_+ with simultaneous excitation of the waves in all six neighboring tubes.
(c) The second scattering problem. The wave incident from 0_- is scattered by the cut in tube 2. It reflects backward, transmits into 0_+ and excites waves in tube 2_+.

The propagation of heat flux Q between the scattering points was assumed to be ballistic because the goal is to get a maximum estimate of the TC. Quick phonon exchange at the scattering points leads to a thermalisation of symmetrical parts of the distribution functions of phonons with temperatures that are determined by values of effective thermal resistances between scattering points. It should be noted that calculations could not be applied directly to multiwall carbon nanotubes.

Thus, there are two different scattering problems. Since the bottle neck of problem 1 is a jump through the opening, let us assume strong interaction between tubes as compared to the phonon energy. In this way, we can achieve the upper estimate of TC. In all cases, the scattering is determined by three coefficients: reflection D, transmission C and penetration to a neighboring nanotube A. In this case, the results for transmission and reflection are independent of the spectrum of the phonon mode and determined by the geometry of the problem only.

For the first scattering problem $|D|^2 = 36/49$, $|C|^2 = |A|^2 = 1/49$ and for the second problem $|D_1|^2 = |C_1|^2 = |A_1|^2 = 1/4$.

1.1.3. Thermal Conductivity

In the approximation of elastic scattering, the heat flux Q along each row of the aligned nanotube is conserved because the waves generated in neighboring nanotubes due to scattering have zero total momentum. This leads to a conservation of Q along the row because in the theory of phonon thermal conductivity any relaxation of Q is the result of momentum loss. It is important, however, that at the points of scattering of both types considered above, the numbers of phonons in each mode changes. Therefore the symmetric parts of the distribution functions in these points can be considered as in equilibrium with different temperatures for each point. Assume that the propagation is ballistic between the scattering points of both types.

In average every section of a nanotube can be divided into seven ballistic regions such that each boundary of the region corresponds to a cut in one of the six neighboring rows of the nanotubes. The part of one row is shown in Fig. 1.2. The energy flux is the same along the row. Since the scattering is different, the temperature intervals between neighboring boundaries are also different. To calculate the TC, the total temperature difference through all the nanotube at a given flux Q was found.

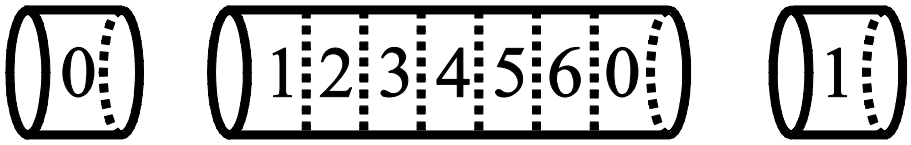

Fig. 1.2: Part of the row of nanotubes with two cuts. Dotted lines in the nanotubes correspond to cuts of the neighboring nanotubes. The regions between them are considered to be ballistic.

Consider one region *i* of a nanotube and assume that each end of the region perfectly matches a thermal bath. The temperature difference of the left and right boundaries of the region is t_i. Thermal flux produced in this region is $Q=G(T)t_i$, where the function G(T) is called thermal conductance. It can be written in the form [18]:

$$G(T) = \frac{k_b^2 T}{h} \sum_a \int_{z_1}^{z_2} \frac{x^2 e^x}{\left(e^x - 1\right)^2} dx \qquad \textbf{(1.1)}$$

where $z = hw/k_BT$ and the sum is over all monotonously increasing segments of spectrum $w_s(k)$, z_1 and z_2 are the lower and upper boundaries of such segments. Here k_B and h are the Boltzmann and the Plank constants respectively. To calculate the above integrals one should know the vibration spectra of nanotubes. They have been calculated previously within different frameworks such as an empirical force constant model [17,19]. The function G(T) calculated by Yu. Gartstein [20] is used in this experiment. Finally, an equation for TC was obtained,

$$k = NLG(T)/B \qquad (1.2)$$

where N is the number of tubes in the bundle per square meter (assuming triangular lattice, it is easy to get N=4 x 10^{17} m^{-2} for (10,10) nanotubes), L is the length of a nanotube, $B = \frac{6}{1- |D_1|^2} + \frac{1}{1- |D|^2} - 6|C_1|^2 - |C|^2$ **=1/0.0976.**

Since the interaction is assumed to be strong, coefficients in B are independent of the frequency. As a result the TC can be expressed in terms of G(T) . Thus, the final result is

$$k = 0.0976G(T)LN \qquad (1.3)$$

Fig. 1.3 shows the results at L=1, 0.87, 0.7μm together with the results by Hone et al. [4]. One can see that the theory reflects well enough both the magnitude and the temperature behavior. In fact, the only parameter here is the average length of a nanotube. The deviation at high temperatures is probably related to the Umklapp processes.

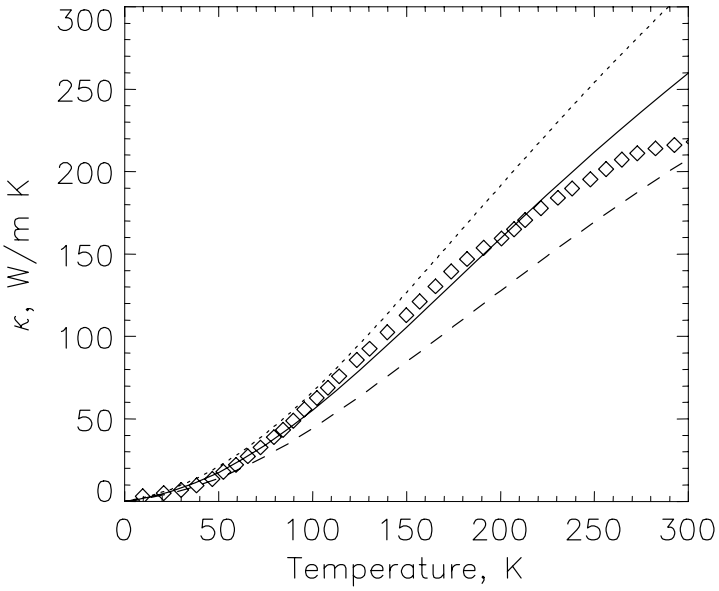

Fig. 1.3: Thermal conductivity as calculated theoretically for the (10,10) tube with L=0.7μm (dashed line), 0.87μm (solid) and 1.0μm (dotted). The experimental data of [4] are shown by diamonds.

1.1.4. Conclusions

In this paper, the maximum estimate of the TC of perfectly aligned nanotubes, taking into account the scattering of phonons by the terminal points of the nanotubes, was presented. This estimate gives a quantitatively correct description of the thermal conductivity of aligned nanotubes as obtained experimentally by Hone et al. [4] assuming that the length of segments is of the order of 1μm. It follows from these results that the way to make the thermal conductivity of the aligned nanotubes at room temperature larger than 300 W/m K is to increase their lengths. Of course, the TC will not increase indefinitely with

length (L), as it follows from (1.3), because, sooner or later, the mean free path, due to other scattering processes, will be smaller than L/7. However, some additional gain may be achieved with increasing L.

The paper is published in cond-mat/0405499 and sent to Phys. Rev. B

1.1.5. References

[1] Guo-Dong, J. D. Kuntz, J. Wan, and A. K. Mukherjee, Nature Materials 2, 38 (2002).

[2] R. S. Ruo and D. C. Lorents, Carbon 33, 925 (1995).

[3] T. R. Anthony, W. Banholzer, J. F. Fleisher, L. Wei, P. K. Kuo, R. L. Thomas, and R. W. Pryor, Phys.Rev. B 42, 1104 (1990).

[4] J. Hone, M. Llaguno, N. Nemes, A. Johnson, J. Fischer, D. Walters, M. Casavant, J. Schmidt,and R. Smalley, Appl. Phys. Letters 77, 666 (2000).

[5] W. Zhou, J. Vavro, C. Guthy, K. I. Winey, J. E. Fisher, L. M. Ericson, S. Ramesh, R. Saini, V. Davis, C. Kittrell, et al., Journal of Appl. Physics 95, 649 (2004).

[6] E. S. Choi, J. S. Brooks, D. L. Eaton, M. S. Al-Haik, M. Y. Hussaini, H. Garmestani, D. Li, and K. Dahmen, Journal of Appl. Physics 94, 6034 (2003).

[7] S. Berber, Y.-K. Kwon, and D. Tamanek, Phys. Rev. Lett. 84, 4613 (2000).

[8] S. Maruyama, Physica B 323, 193 (2002).

[9] M. Osman and D. Srivastava, Nanotechnology 12, 21 (2001).

[10] J. Che, T. Cagin, and W. Goddard, Nanotechnology 11, 65 (2000).

[11] Q. Zheng, G. Su, J. Wong, and H. Guo, Eur. Phys. J. B 25, 233 (2002).

[12] J. X. Cao, X. H. Yan, Y. Xiao, Y. Tang, and J. W. Ding, Phys. Rev. B 67, 045413 (2003).

[13] M. Dresselhaus, G. Dresselhaus, and P. Avouris, eds., Carbon Nanotubes: Synthesis, Structure, Properties and Applications (Springer, Berlin, 2000).

[14] D. Cahill, W. Ford, K. Goodson, G. Mahan, A. Majumdar, H. Maris, R. Merlin, and S. Phillpot, J. Appl. Phys. 93, 793 (2003).

[15] R. Baughman, A. A. Zakhidov, and W. A. de Heer, Science 297, 787 (2002).

[16] Y. Yosida, Journal of Appl. Physics 87, 3338 (2000).

[17] M. Dresselhaus and P. Eklund, Adv. Phys. 49, 705 (2000).

[18] K. Schwab, E. Henriksen, J. Worlock, and M. Roukes, Nature 404, 974 (2000).

[19] R. Saito, G. Dresselhaus, and M. Dresselhaus, Physical Properties of Carbon Nanotubes (Imperial College Press, London, 1998).

[20] Yu. N. Gartstein, unpublished, I am grateful to Dr. Gartstein for calculation of the function G(T).

1.2 Theory of Thermal Conductivity by Polaritons

See APPENDIX 5.1 and 5.4

1.3 Modeling of Phonons and Heat Transfer in Carbon Nanostructures

1.3.1. Phonon dynamics and thermal properties of zigzag and armchair carbon nanotubes

Report-2b: "Strategies to Increase Thermal Conductivity. Enhancement by Optical Phonon Sub-Bands Engineering in 3-D Nanostructures Based on C and BN Nanotubes"

1.3.1a. Phonon dynamics and thermal properties of zigzag carbon nanotubes

Content

I. Introduction

II. Phonon dynamics in a zigzag carbon nanotube

III. Generalized equation of thermal conductivity in a single nanotube

IV. Thermodynamics and statistics for a carbon nanotube

V. Summary

VI. References

VII. Attachment - Short investigation plan

I. Introduction

This report presents the second stage of investigation of phonon fluxes in carbon and BN nanostructures in the framework of the tasks for *"Strategies to Increase Thermal Conductivity. Enhancement by Optical Phonon Sub-Bands Engineering in 3-D Nanostructures Based on C and BN Nanotubes"*.

Here, the dynamics of the heat transfer problem for closed carbon nets (planned point 1c), zigzag tubes (point 2c) and macroscopic manifestations (point 3c) are presented. Phonon eigenstates, density of states and vibration amplitude distribution for each phonon along the molecular fragment are considered for two main tubulene geometries: zigzag and armchair.

The idea of the PQDM approach proposed in the previous report is to use a discrete microscopic model for phonon dynamics of relatively small molecular fragments approximately of phonon mean free path sizes. The dynamics of such a cluster may be described classically in Born approach [1, 2] and all the important data may be obtained: eigenfrequences, density of states and phonon amplitude distribution inside the molecular fragment during its lifetime. Neighboring fragments of a molecular net are in an uninterrupted process of exchange by phonons. Due to the weak fragment-surrounding medium interaction, the process may be described by Fermi's "golden rule" which determines the value of the transfer rate. This quantum characteristic is a transport process consideration that enables the introduction of a microscopic thermal conductivity coefficient that depends on the temperature difference between opposite sides of the fragment in contact with the baths.

An averaged classical picture of phonon energy (heat) transport and temperature distribution in the big 2D carbon nets, both open (graphene) and closed (tubulenes), and other kinetic and statistical phenomena may be obtained in rough space scale. The transition to rough scale leads to the generalized phonon kinetics equation describing heat propagation in 2D molecular nets. Results obtained in the previous report for flat nets have important meaning for comparison with that for closed nets. Considering here phonon dynamics and statistics in tubes with zero-chirality and of zigzag geometry, comparison with data for flat nets will be made.

The general picture of connected subjects for the problem of phonon propagation in molecular nets is shown in Fig.1.

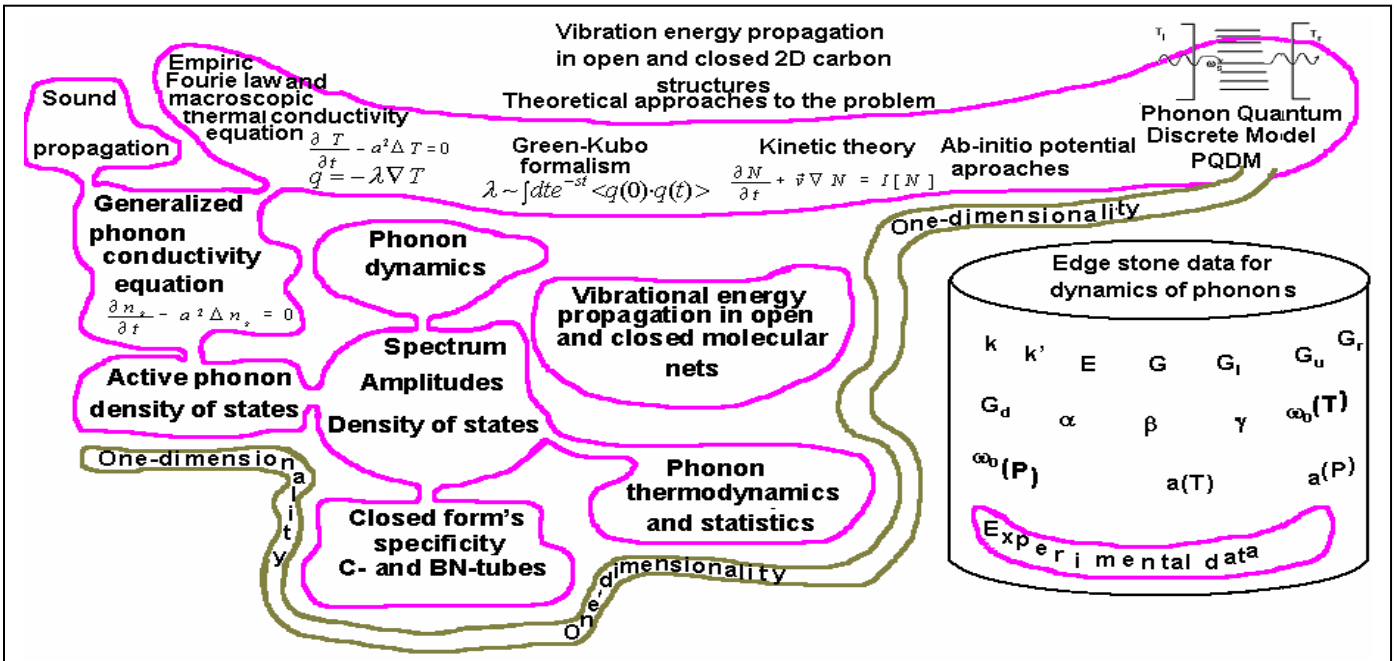

Fig.1. General picture of connected subjects for the problem of phonon propagation in molecular nets.

In Fig.1, fundamental data such as elastic modulus E, G and elastic coefficients *k, k'* describing forces when shifts are directed along the main axes of the bond potential ellipsoid are presented. *U(r)* is the site potential energy of an atom which has to be determined in other approaches; the same for thermal expansion coefficient β, pressure coefficient γ(T), characteristic frequency (or phonon band width) temperature dependence $\omega_0(T)$.

II. Phonon dynamics in a zigzag carbon nanotube

Linear approximation in phonon dynamics is based on the supposition that small atomic vibrations have harmonic character at least in the case of not too high temperatures. It means that a potential equienergetical surface in the vicinity of atomic equilibrium positions has an ellipsoidal form. Classical motion of atoms near their equilibrium points is described by elastic constants *k* that characterizes atom-atom bonds in Born approach [1]. For atomic shifts perpendicular to bond we will use nonzero elastic constant *k'* << *k* coming out the framework of linear approximation.

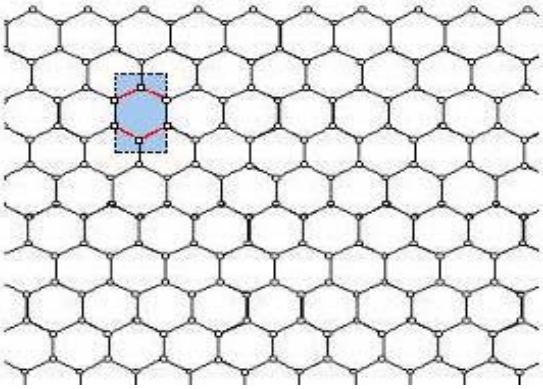

Fig.2. Fragment of hexagonal lattice. Shaded is the conventional elementary cell containing four atoms. Two types of bonds are presented by different colors.

The symmetry of carbon structures dictates three main vibration types (radial ρ-mode, tangential φ-mode and axial z-mode) shown in Fig.3. It should be marked that principal difference between vibration branches originates from bonds direction relative the direction of symmetry axes connected with given freedom's degree. This difference manifests itself in phonon band structure for tangential and axial branches in pure zero-chirality case. In presence of helicity the difference vanishes.

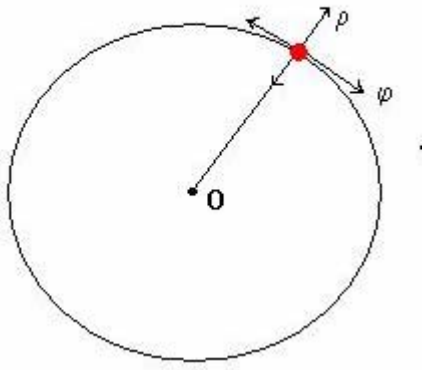

Fig.3. The problem's geometry. Z-axes is perpendicular to the figure plane. It's shown φ and ρ shifts of an atom.

In Fig.4, the case when φ-mode and axial z-mode have approximately equal orientation shifts relative to both red and blue bonds inside a chosen elementary cell is

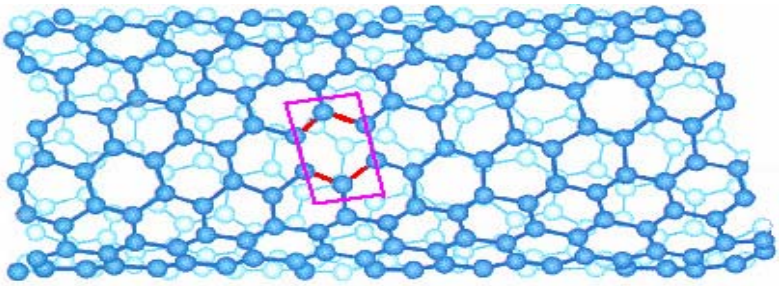

Fig.4. Fragment of armchair tubulene (10,5) with non-zero chirality created from a graphene sheet {14,10} by rolling up around the armchair direction. Picked out is the conventional elementary cell containing four atoms. Two types of bonds are marked by different colors.

presented.

Systems of dynamical equations for all three branches of vibrations are calculated taking into account that the motion of each atom is three-dimensional. The zero-approximation approach supposes that radial ρ-mode, tangential φ-mode and axial z-mode should be considered independently.

Consider a zigzag tube (n,0) produced from the fragment shown in Fig.2 by rolling around vertical direction without any shift. In this case, each of the tube fragments is connected with the same fragment. Therefore, contrary to the case of flat fragments connecting external media (Report-1b) all atomic positions and their bonds are described similarly by the same dynamical equations. The difference exists with different vibration types or branches only.

For shifts directed normal to the tube surface, the equation is the following

$$\{m\ddot{\rho}_i = -k'(3\rho_i - \rho_{i1} - \rho_{i2} - \rho_{i3}),$$

(1)

where i_1, i_2, i_3 are indexes for atom i neighbors. Atomic coordinates are not important here. The united atomic number i is defined using its position in the row and column of initial flat fragment creating the tube. For tangential atomic shifts having in view that atom space coordinates on the tube surface $x=\varphi R$, where R is the tube radius and φ is the azimuth angle. The zigzag case with the absence of chirality is described by the system:

$$\{m\ddot{x}_i = -0.75k(2x_i - x_{i1} - x_{i2}) - k'(x_i - x_{i3})$$

(2)

where coefficient 0.25 characterizes two weak bonds for this vibration. For axial atomic shifts we have

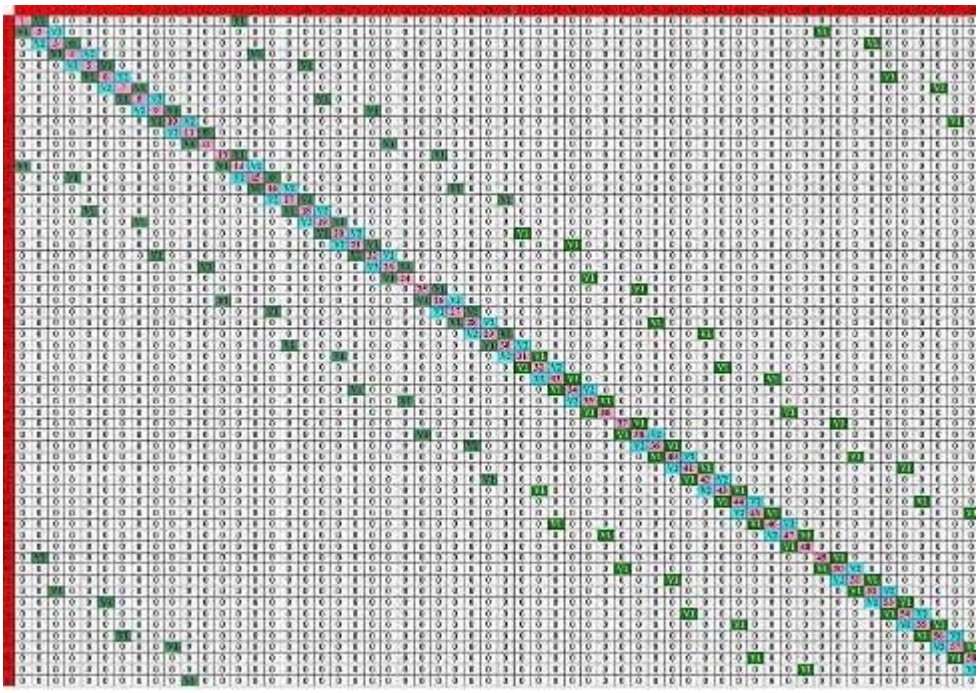

Fig.5. Sketch of the dynamical matrix for zigzag tubulene created from a graphene sheet {5,5} containing 60 atoms by its rolling up. Rose-colored spots are diagonal elements, green and blue show two types of bonds, rest elements equal to zero, left and upper red bands contain atomic numbers.

$$\left\{ m\ddot{z}_i = -k(z_i - z_{i1}) - 0.25k(2z_i - z_{i2} - z_{i3}) \right. \tag{3}$$

Matrix structure of all equations (1-3) corresponding zigzag (n,0) case is shown in Fig.5.

Fig. 5 shows a zigzag tubulene matrix and vibration amplitudes. Atomic coordinates become important when mode amplitude distribution is presented in the space.

The square of vibration mode s=1 of any type is shown in Fig.6. There are considerable differences in amplitude distribution over the tube surface relative open carbon net. The differences are caused by a change in the topology of the system. The difference between mode frequencies and density of states at the same number of state exists but it is not essential.

The calculations given are for eigenvectors $|C_{si}|^2$ which is a well known standing wave picture with corresponding number of knot's lines depending on the number of state *s*. Increasing the number of states leads to lateral (parallel to z-axes) divided by transversal (circular) knot's lines the tube's surface.

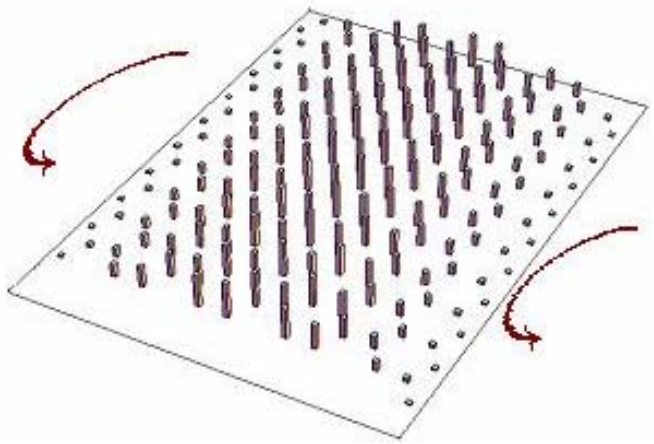

Fig.6a. Calculated ρ-branch amplitude distribution along zigzag tubulene created from a graphene sheet {8,10} by rolling up around marked direction. Ground state.

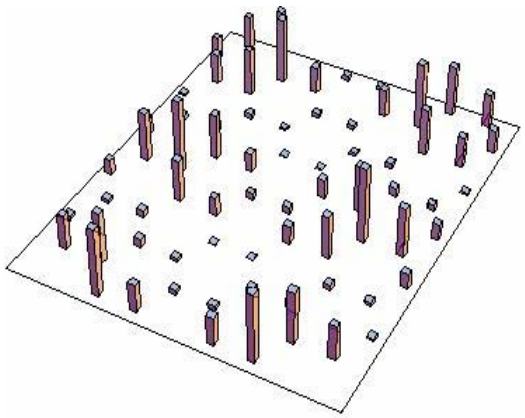

Fig.6b. ρ-branch amplitude distribution along zigzag tubulene created from a graphene sheet {5,5} by rolling up around marked direction. 5th state. Transversal knot's line is degenerated.

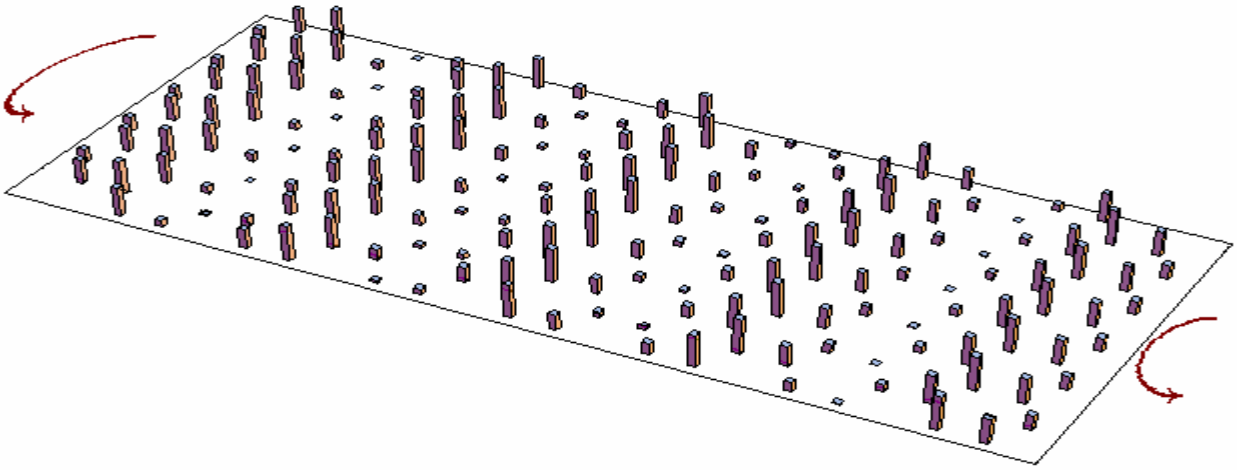

Fig.6c. ρ-branch square amplitude distribution along zigzag tubulene created from a graphene sheet {14,5} by rolling up around marked direction. Four transversal knot's lines correspond to 5th-state.

The Low frequency ground state is shown in Fig.6a. The picture is typical for mean amplitudes distribution: maximal amplitudes situates near the tube's middle. The Fig.6b illustrates amplitude distribution for 5^{th} (or r-4^{th}) state where twice degenerated line of knots crossing two non-degenerated lateral lines of knots.

Increasing the tube's length leads to a considerable change in the picture of vibrations. The same 5^{th} (or r-4^{th}) state presented in Fig.6c has another combination of knot's lines. The transversal line vanishes and two additional lateral lines of knots arise.

The mean vibration amplitudes A_j averaged on the state populations n_s decrease from the lateral ends to the middle axes of the nanobridge.

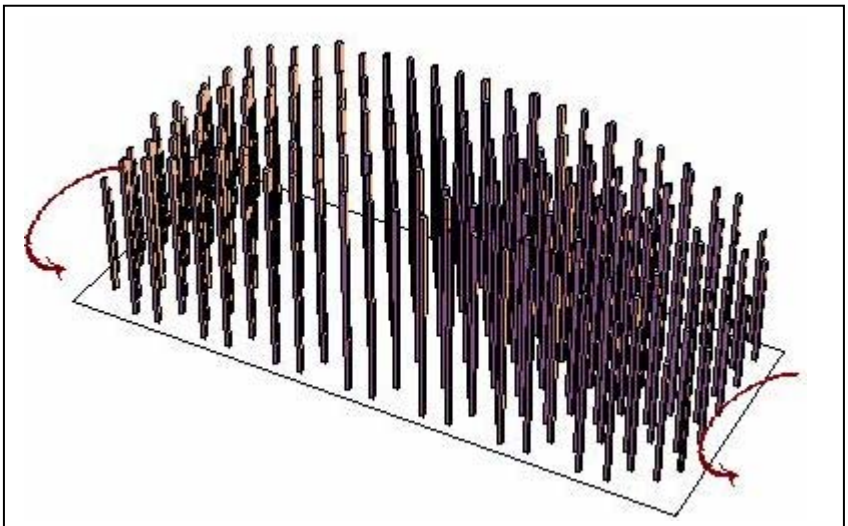

Fig.6d. Calculated mean square amplitude distribution along zigzag tubulene created from a graphene sheet {15,5} by rolling up around marked direction. T=0.03 eV. Circular arrows show rolling up of the structure.

More free lateral atoms have bigger vibration amplitudes.

$$A_j = \sum_{s,\sigma} \left| C_{sj} \right|^2 n_{s\sigma} \quad , \tag{4}$$

where $n_{s\sigma}$ is the population of s,σ state, j numbers atoms situated on the tube surface and C_{sj} is the s-state probability amplitude at j-position of the net. Mean square amplitudes calculated for temperature T=0.03eV by expression (4) are shown in Fig.6d. The averaging was made here on all phonon branches σ. One can see that in contrary with flat carbon terminated nets with free edge atoms the closed structure is harder near the edges and greatest amplitudes of vibrations take place in the middle of the tube. The greater are temperatures the lesser is this effect of hard tube ends. Tube ends are frozen at low temperatures.

The density of states (DOS) for a zigzag tubulene spectrum is shown in Fig 7a.

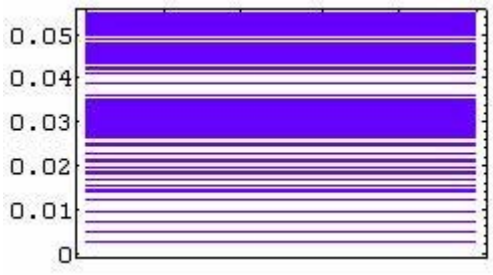

Fig 7a. Radial mode spectrum of zigzag tubulene created from a graphene sheet {5,15} by rolling up around z-axes. The unity of frequency is ω_0

The density of states may be approximately defined by the expression :

$$g(\omega_{s\sigma}) \approx \frac{1}{\omega_{s\sigma} - \omega_{s-1,\sigma}} \tag{5}$$

that transfers to an exact one if the number of degrees of freedom becomes big enough. More correctly, the density of states function may be calculated providing preliminary state grouping and density determination inside the each group. DOS calculation were made with preliminary state grouping using dividing the whole frequency band interval into h=Int[35r/50] sub-intervals (or near this value) where the number of eigenmodes was counted. The integer numbers are present on vertical axes in figures 7b, 8b and 9b. Frequency spectrum and DOS function in case of zero chirality are presented in Fig 7-9. The figures 7a, 7b were obtained by numerical calculation in system (1) described by the matrix of eigenvalues problem shown in Fig.5a

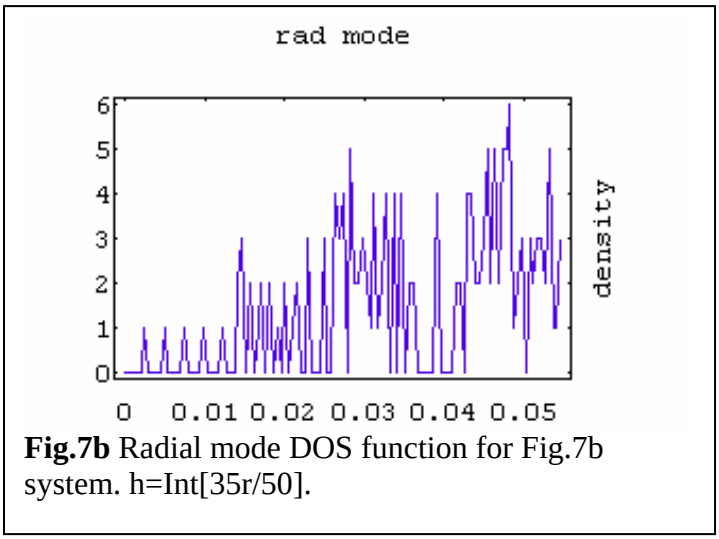

Fig.7b Radial mode DOS function for Fig.7b system. h=Int[35r/50].

The comparison of these results obtained for the tube radial mode spectrum and DOS function for a graphene fragment of the same number of atoms and zigzag orientation shows the absence of any significant differences. Thus, the process of sheet rolling up into a tube has no influence on spectrum and density of states in this type of vibration case. But vibration amplitudes distribution (Fig.6) differs from that for graphene (see Report-1b, Fig.3, Fig.9a, Fig.9b) where the mean vibration amplitudes of the sheet free edges were bigger than that in the middle (Fig.9a). One can see that the tube has hard edges and soft middle part (Fig. 6a, 6d)

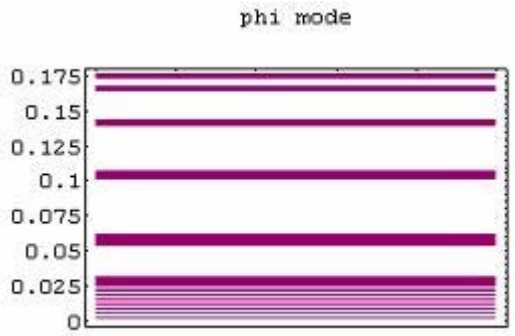

Fig 8a. Azimutb mode spectrum of zigzag tubulene created from a graphene sheet {5,15} by rolling up around z-axes. The unity of frequency is ω_0 .

Calculated by system (2), the frequency spectrum and DOS function for azimuth mode are shown in Fig. 8a, 8b. Fig 8c presents the result of numerical calculation for azimuth mode existing in graphene sheet {15,5}, consisting 190 atoms.

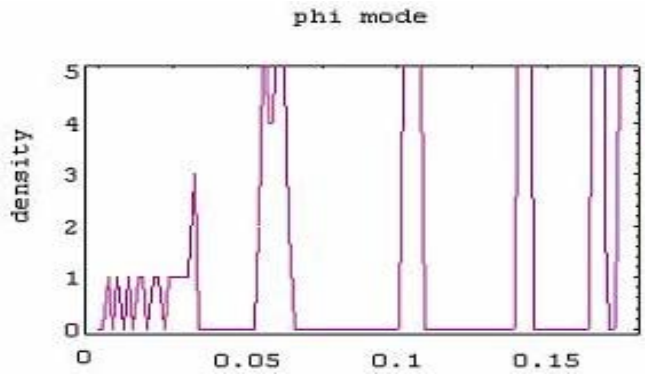

Fig.8b Azimuthal mode DOS function (arbitrary units) for tubulene fragment created from a graphene sheet {5,15} by rolling around z-axes. h=Int[35r/50].

The comparison of results in Fig.8b obtained for tube with azimuthal mode spectrum and DOS function for graphene fragment of the same number of atoms Fig.8c shows some differences. Thre tube's number of bands is twice less than that of a plane sheet. The reason lies in the double degeneration of athimuthal motion around the tube axes. For this type of vibrations, the process of rolling a sheet into a tube has an influence on the spectrum and density of states. The tube creating process is accompanied by subbands uniting due to the fact that rotational symmetry arises.

Vibration amplitudes distribution or space density distribution are similar for all types of phonons as shown in Fig 6.

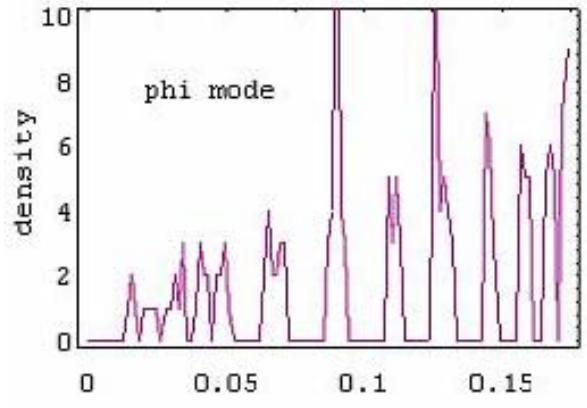

Fig.8c Azimuthal mode DOS function (arbitrary units) for graphene sheet {5,15} h=Int[35r/50].

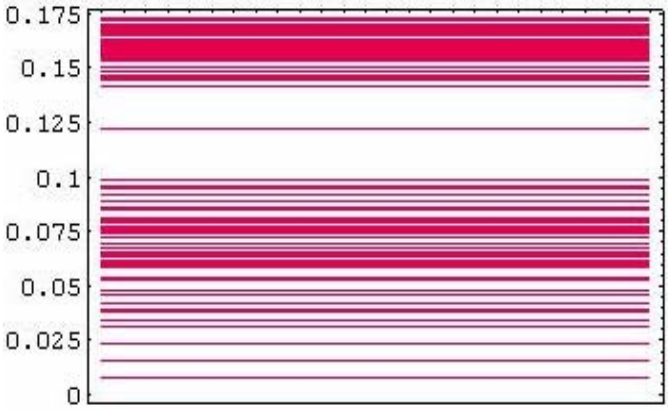

Fig 9a. Axial mode spectrum of zigzag tubulene created from a graphene sheet {5,15} by rolling up around z-axes. The unity of frequency is ω_0 .

Calculated from the system of equations (3), the frequency spectrum for z-branch modes is shown in Fig. 9a. The arising of a narrow subband near $0.125\omega_0$ that plays the role of a characteristic "mark" for the changed topology of the system is of great interest. The density of states function for h=Int[35r/50] is shown in figure 9b. Superposition of two DOS functions presented in Fig. 9c gives an opportunity to immediately compare the spectra of open and closed graphene structures. In the case of z-type vibrations for zigzag tubulene, one can say that the only consequence is the arising of a narrow subband containing 2*n levels in the middle of the gap. This is because the new topology permits circular standing waves for z-type vibrations that were forbidden before in the plane structure.

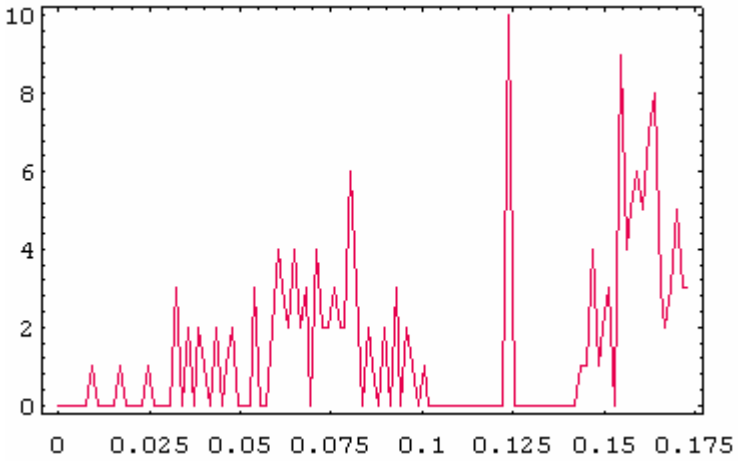

Fig 9b. Axial mode DOS function (arbitrary units) for tubulene fragment created from a graphene sheet {5,15} by rolling around z-axes. Horizontal axes, frequency in ω_0

There exist different opinions as to the spectrum transformation when a graphite sheet is rolled up into a tube [3, 4]. These results show that only some of the graphene spectrum characteristics change significantly (case φ-mode and z-mode). As to the low-frequency ρ-branch, one can talk about spectra similarity.

III. Generalized equation of thermal conductivity in a single nanotube

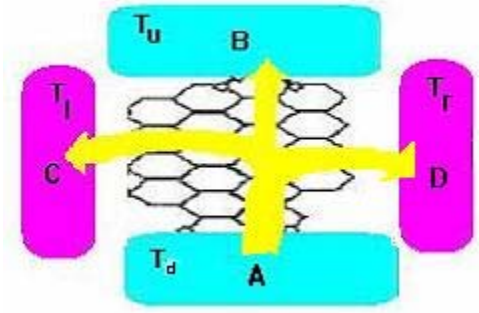

Fig.10a. Heat transistor (4-polar contact) on a flat carbon structure connecting four baths at different temperatures T_l , T_u , T_d and Tr.

The PQDM analysis, proposed in Report-1b, considered heat processes from "first principles" using microscopic characteristic on a quantum level including phonon jump probability, phonon-phonon interaction, calculated spectrum and amplitudes distribution along the structure and macroscopic kinetic approach operating by length of phonon decoherence l_{ph} or phonon mean free path. The time of the phonon state establishing in area l_{ph} x l_{ph} is much less than the phonon lifetime. The **latter is determined by phonon-phonon scattering and may lay in interval (10^{-8}-10^{-7})s [???]. This supposition allows one to consider propagation of phonons as a sequence of jumps from one fragment to another with relatively long life on each one. Figures 10a, 10b illustrate 2D phonon propagation by jumps between mean free path-sized areas. Neighboring areas play a role of leads having some fixed temperatures. Taking into account that phonon scattering processes are weak ones we have obtained generalized equation of phonon dynamics.(Report-1b, paperzd-a.doc).**

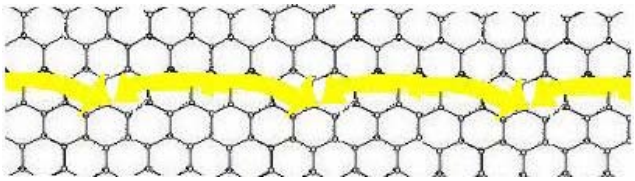

Fig.10b. Phonon jumps over a carbon armchair structure (arrows). One-dimensional phonon dynamics in tubulenes.

Temperature distribution along the tube

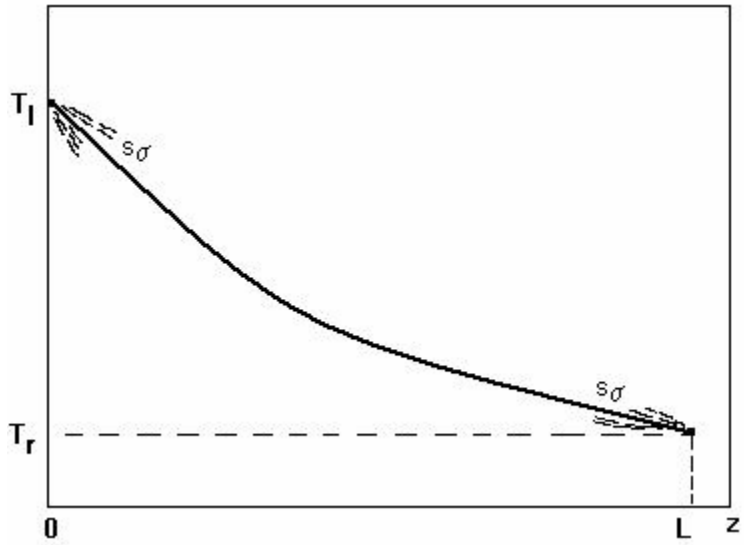

Fig.11. One dimensional phonon dynamics. Exact temperature distribution along the tube given by (7). T_l ,T_r.are end temperatures, L is the tube length. End points come together all modal (partial) temperatures for each sσ.

The phonon mean free path l_{ph} decreases with increasing of temperature. Evaluations made in different sources give interval from hundred Angstroms to several micrometers at room temperatures. In any case azimuthal phonon motion may be considered as ballistic one and

jumps or diffusion in tubes may occur only in axial direction. In relation to phonon propagation nanotubes embody an ideal one-dimensional system. In stationary case it is ease to write the exact solution of the 1D variant of equation (6).

$$T(z)=\frac{\omega_{s\sigma}}{\ln\left(1+\frac{L}{Ln_l(\omega_{s\sigma})+(n_r(\omega_{s\sigma})-n_l(\omega_{s\sigma}))z}\right)} \qquad (7)$$

Here L is tube's length, z is axial coordinate along the tube, n_l n_r are population numbers $n_{s\sigma}$ taken at left and right temperatures of both tube ends T_l ,T_r. Indeed on the macroscopic level local populations n_l n_r obeys equilibrium Planck law. The approximate behavior of temperature distribution is shown in Fig.11. The bundle of partial modal temperatures comes together in end points. With increasing temperature, all modal dependences become equal. The difference may be essential at low temperatures.

Thermal conductivity and phonon mean free path

Thermal conductivity was calculated here in PQDM approach for tubes of zigzag geometry by expression

$$\lambda'(l_{ph})=\frac{2\pi l_{ph}}{T^2}\sum_{s,\sigma}\left|G_{ls}\right|^2\left|G_{rs}\right|^2\omega_{s\sigma}^2 g(\omega_{s\sigma})\frac{N(\omega_{s\sigma})(N(\omega_{s\sigma})+1)}{\left|G_{ls}\right|^2+\left|G_{rs}\right|^2}, \qquad (8)$$

where l_{ph} is phonon mean free path, square modulus reflect connections of end atoms of the tube fragment with the rest part of the tube.

$$G_{ls}=\sum_{i_l}G_{i_l}C_{i_l s} \qquad (9)$$

Left and right end atoms numbered i_l and i_l were taken into account with its bonds orientations. Formula (8) is a partial case of obtained in Report-1b expression (16) for thermal conductivity when left and right DOS functions coincides with own density of states $g_r=g_l$.

The l_{ph} is playing here in some sense the double role. From one side it dictates the length of tube fragment where phonon states occur in ballistic regime. For a zigzag tube made from a graphene sheet {n,m} we have $l_{ph}=2ma$, where a is the bond length. In accordance with PQDM approach l_{ph} coincides with the length of calculated fragment with phonon standing waves inside. In contrary, DOS function $g(\omega_{s\sigma})$ describes the left (=right)

medium. From the other side l_{ph} depends on phonon-phonon collisions that in own turn depend on the temperature.

It is worth to evaluate temperature dependence of l_{ph}. General expression for phonon mean free path is given by the surface density of phonons S/N.

$$l_{ph} \approx \sqrt{\frac{S}{N}} = \sqrt{\frac{l_d \cdot l_{ph}}{N}} \qquad l_{ph} \approx \frac{l_d}{< N >} \quad , \tag{10}$$

$$< N >= \frac{1}{\Delta}\int n(\omega) g(\omega) d\omega \tag{11}$$

where S is the tube surface where phonons propagate, l_d is the tube circle length, Δ is the phonon band width and <N> is mean number of phonons. Taking into account that <N>∝T we have

$$l_{ph} \sim \frac{1}{T} \tag{12}$$

Implicitly l_{ph} is contained in upper limit of summation in (8), in $|G_{ls}|^2$ and in $g(\omega_{s\sigma})$. The size dependence for zigzag tubes of given diameter and at given temperature was calculated by (8). The Fig.12 presents typical picture of linear λ increasing vs phonon mean free path.

$$\lambda \sim l_{ph} \tag{13}$$

Relations (13), (14) contain an explanation for the well-known experimental fact of thermal

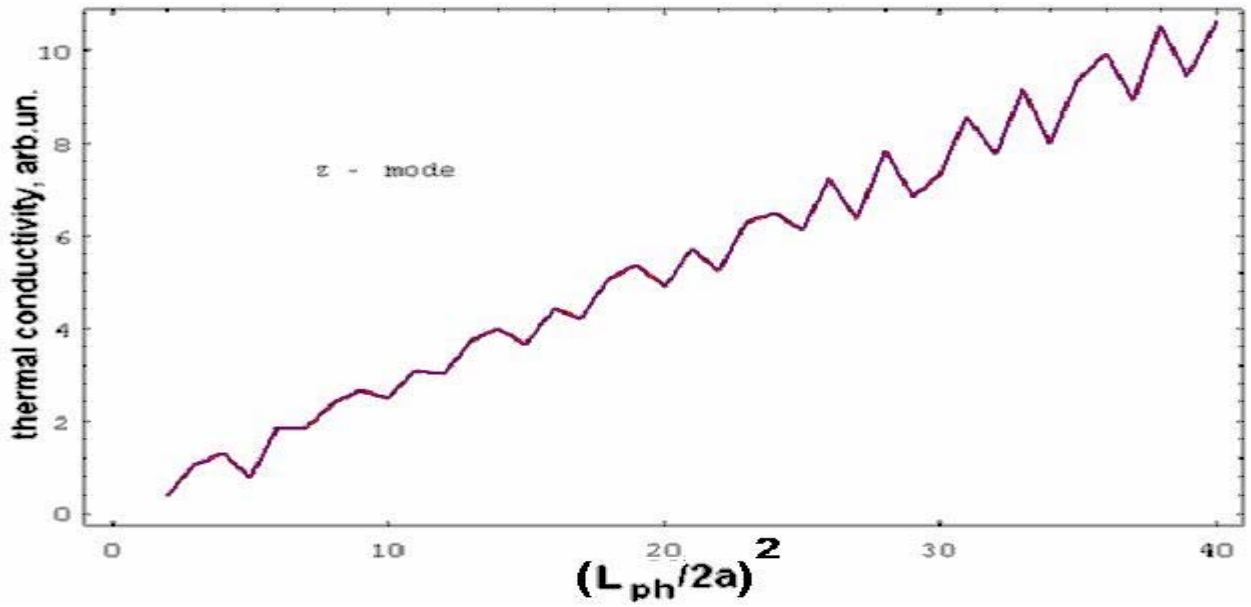

Fig.12. One dimensional phonon dynamics. Thermal conductivity size dependence for axial branch of vibrations. L_{ph} is phonon mean free path, a is carbon bond length. For radial and athimuthal branches dependence has the same character.

conductivity temperature damping at high temperatures by 1/T law. It is of interest also that the PQDM gives a simple opportunity to connect heat propagation with the definition of phonon mean free path.

The result of thermal conductivity numerical calculations for radial, azimuthal and axial phonon branches (σ=1,2,3) is presented in Fig.13. It is easy to see that the sum on all σ will be very close to curve 3 connecting with radial ρ-band. Unity λ_0 determined from (8) and (16) from Report-1b is measured in *W·m/K*

$$\lambda_0 = \frac{2\pi a G_0^2}{\hbar\omega_0} k \quad , \qquad (13)$$

where *a*=1.2 Angstrom is unity of length, *k* is Boltzmann constant, ω_0 is accepted here phonon energy unity and G_0 is the constant of phonon-phonon interaction. Evaluations [4-8] give for characteristic phonon energy interval $\omega_0 \in$[0.8-1.2]eV.

It should be marked that weak temperature dependence has also the structure constant (bond length *a*) of the system. Thermal expansion of single walled nanotubes was investigated in [9-12] but the result obtained there for radial expansion is not a reliable one. Elastic constants and the constant of phonon-phonon interaction G_0 depend on the temperature too.

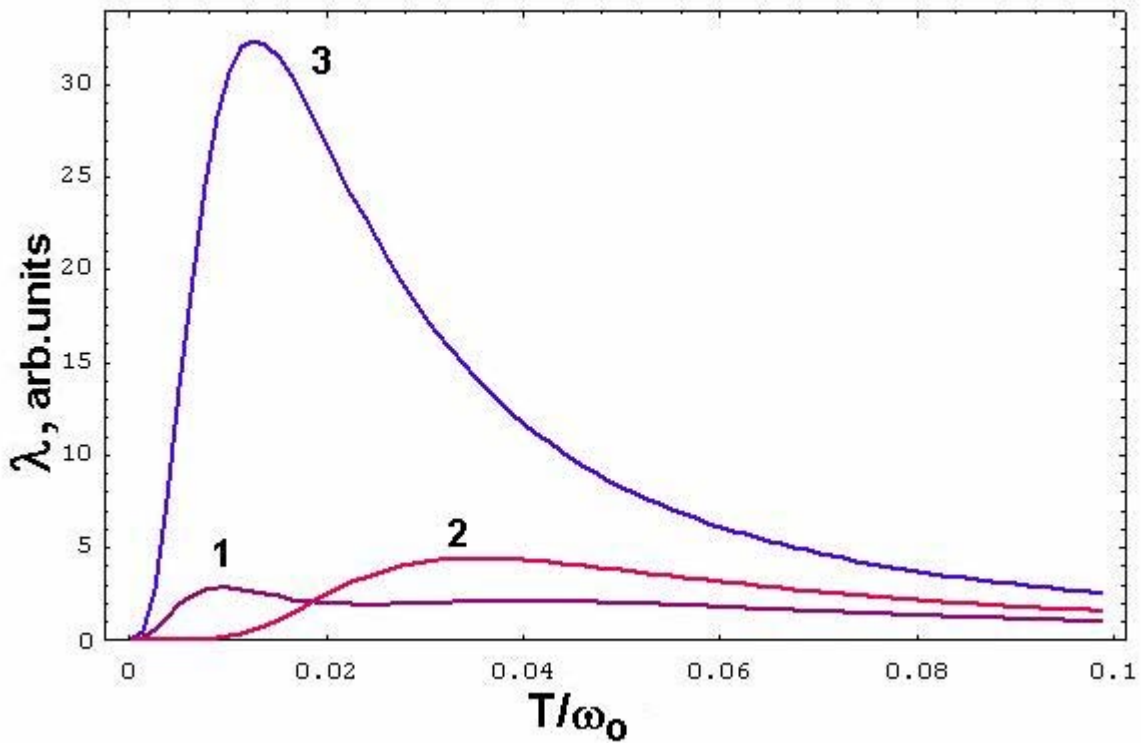

Fig.13. Thermal conductivity temperature dependence. Zigzag NT. Curve 1 corresponds to z-branch contribution, curve 2 to φ-branch and ρ-branch contribution is presented by curve 3.

The conclusion that radial mode contribution into heat transfer is dominating in temperature interval under consideration is based on the supposition that phonon-phonon interaction constant G_0 (see (8), (9), (13)) participating in end atoms constants G_{il} does not depend on the phonon type (ρ, φ or z). Then due to big density of states in narrow low-frequency ρ-band comparatively with that for φ- and z-vibrations essential prevail of ρ-vibrations arises. So at actual temperatures ρ-branch of phonons determines heat propagation through single-walled nanotube. One should wait the same effect and for armchair geometry too. The problem of phonon-phonon constants for different vibration types is open now and should be investigated in detail in following study.

IV. Thermodynamics and statistics of zigzag nanotubes

Static thermodynamic characteristics of non-helical zigzag nanotubes of different sizes have been calculated. If the system exists in equilibrium state, the atomic heat capacitance *C(T)* and entropy *S(T)* are as follows,

$$C(T)=\frac{1}{r}\sum_{s,\sigma}\omega_{s\sigma}\frac{\partial N(\omega_{s\sigma})}{\partial T}=\frac{1}{rT^2}\sum_{s,\sigma}\omega_{s\sigma}^2 N(\omega_{s\sigma})(N(\omega_{s\sigma})+1), \qquad (14)$$

where *r=2n(m+1)* is the number of atoms in a zigzag tube of length *2ma* and radius *a/(2sin(π/n))*.

$$S(T)=\int\frac{C(T)dT}{T}=\frac{1}{r}\int\frac{dT}{T^3}\sum_{s,\sigma}\omega_{s\sigma}^2 N(\omega_{s\sigma})(N(\omega_{s\sigma})+1), \qquad (15)$$

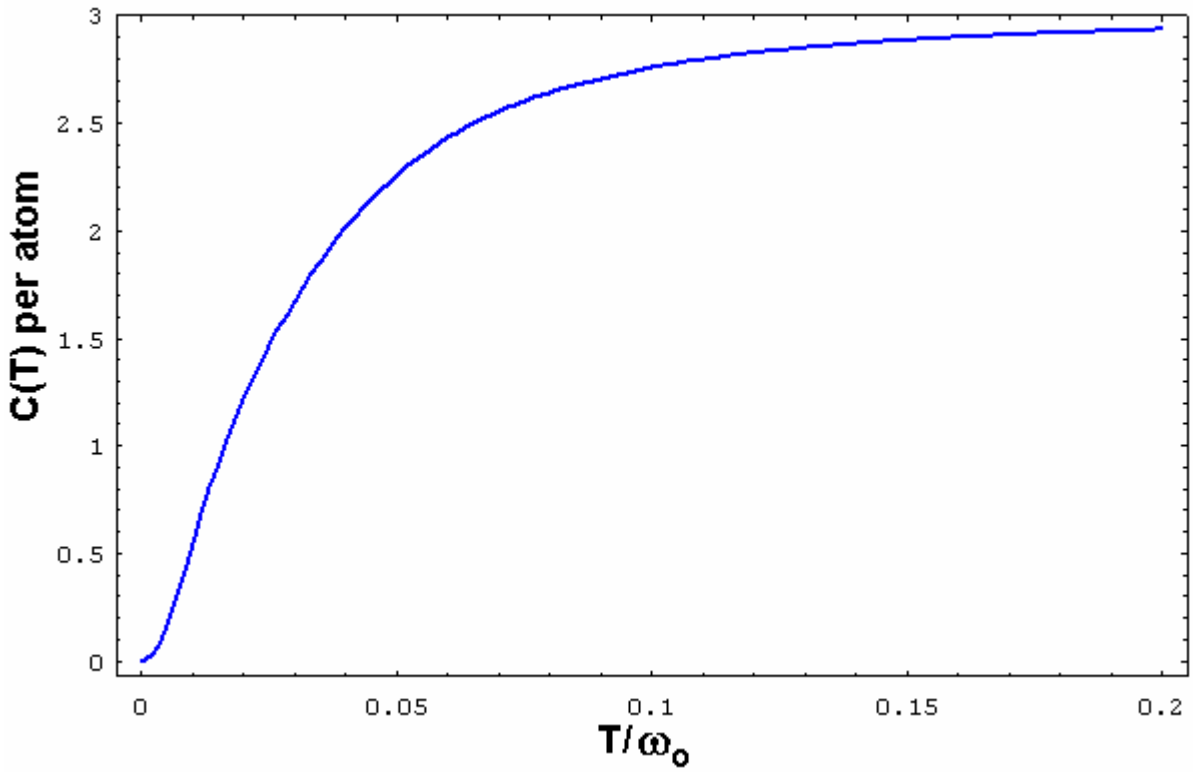

Fig.14. Heat capacitance vs temperature dependence for zigzag nanotube. Dulong-Petit law and W.Nernst theorem. $\omega_0 \in (0.8, 1.2)$eV.

The calculated temperature dependence for heat capacitance is shown in Fig.14. The curve illustrates the third thermodynamical law (W.Nernst theorem) at low temperatures and Dulong-Petit law at high temperatures ($T>0.1\omega_0$). The entropy behavior has similar character at low temperatures and shows logarithmic growth at high temperatures.

V. Summary

A complex approach PQDM was applied to describe dynamics, kinetics and statistics of phonons in carbon nanotubes with zero-chirality.

Atom vibration dynamics was considered for carbon nanotubes of zigzag geometry in comparison with the results obtained for graphene sheets. Vibrational eigenmodes, density of states and amplitude distribution for tube fragments of the length up to 40 hexagons were calculated in linear approximation for three types of vibration: athimuthal or tangential φ-mode, radial ρ-mode and longitudinal z-mode.

Thermal fluxes and thermal conductivity were considered in PQDM. Temperature dependences were obtained. The mechanism of heat conductivity temperature damping was analyzed.

The exact solution of generalized thermal conductivity equation was obtained for nanotubes. Temperature distribution along the tube was derived analytically.

Size dependences were considered for thermal conductivity. It was shown the linear increasing of heat conductivity with the growth of the phonon mean free path.

Statistical properties were investigated. Heat capacitance and the entropy of carbon linear tubes were calculated as the function of temperature.

VI. References

1 M.Born, K.Xuang Dynamical Theory of Crystal Lattice. London: Oxford Univ.Press, 1954.

2 J.Tersoff. New empirical approach for the structure and energy of covalent systems. Phys.Rev. **B37**, 6991 (1988).

3 N.G.Chopra, A.Zettl. Measurement of the elastic modulus of a multi-well BN nanotube. Sol.St.Commun. **105**, 297 (1998).

4 L.X.benedict, S.G.Louie, M.L.Cohen. Sol.St.Commun. **100**, 177 (1996).

5 J.Yu, R.K.Kalia, P.Vashishta. Phonons in graphitic tubules: a tight binding molecular dynamics study. J.Chem.Phys. **103**, 6697 (1995).

6 J.Hone, M.Whitney, C.Piskoti, A.Zettl. Thermal conductivity of single-walled carbon nanotubes. Phys.Rev. **B59**, R2514 (2000).

7 J.W.Kang, H.J.Hwang. Thermal properties of ultra-thin copper nanobridges. Nanotechnology **13**, 503 (2002).

8 D.Tomanek. “Thermal and electrical conductance of carbon nanostructures” in Nanostructured Carbon for Advanced Applications, ed. G.Benedek et al. , NATO Science Series, **24**,263 (2000). S.Berber, Y.-K. Kwon, D.Tomanek. Unusually high thermal conductivity of carbon nanotubes. E-archive: cond-mat/0002414.

9 Yu.Maniwa et.al Thermal expansion of single-walled carbon nanotube bundles: X-ray diffraction study. Phys.Rev. **B64**, 241402 (2002).

10 C.G.Ho, R.W.Powell, P.E.Lilley Thermal conductivity of simples chemical compaunds, J.Che.Ref.Data, **1** , 279-425, (1972).

11 R.Berman, Thermal conductivity in solids, Clarendon Press, Oxford, 1976.

12 M.D.Ventra, S.G.Kim, S.T.Pantelides, N.D.Lang. Temperature effects on the transport properties of materials. Phys.Rev.Lett. **86**, 288 (2001).

VII. Attachment: Short investigation plan

1. Phonon(vibron) bands. Direct calculation in elastic approximation.

a) Graphene molecules of various kinds, free and contacting with two leads. Influence of the number of bounding atoms on phonon structure.
b) Phonon structure of 3-polar and 4-polar molecular bridges.
c) Carbon tubes of various radii. Short fragments. Free and contacting with leads.
d) BN- flat structures. Free and contacting.
e) BN-tubes of various radii. Short fragments. Free and contacting with leads.
f) More complicate geometry. Torus. Two wall C-tube as a heat conductor.

2 Heat transport investigation in PQDM.

b) Linear carbon chains connecting electrodes (analytical approach)
c) Graphene molecules of various kinds contacting with leads. Calculation.
d) Carbon tubes of various radii. Short fragments. Free and contacting with leads.
e) BN- flat structures. Free and contacting.
f) BN-tubes of various radii. Short fragments. Free and contacting with leads

3 Macroscopic manifestations of phonon propagation in carbon nets.

a) Generalized 2D and 3D equation of thermal conductivity in carbon nets.
b) Boundary problem and temperature distribution in macroscopic carbon nets.
c) Boundary problem for heat conductivity in carbon and BN tubulenes and temperature distribution along tubulene bridge..
g) Carbon tubes of various radii. Short fragments. Free and contacting with leads.

4 Phonon-phonon effects in charge and heat transport.

a. Spectrum modification due to phonon-phonon processes;
b. Non-linear transport through flat carbon structures;
c. Non-linear transport along carbon tubulenes;

5 Thermodynamics and statistics of closed and open carbon nets

a. Statistical sum and entropy of carbon nets (graphene and tubulene).
b. Heat capacitance of graphene and tubulene structures

6 Heat-transistor effects.

a. Three pole systems;
b. Four pole systems;

7 Electron-phonon effects in charge and heat transport.

a. Transport through linear carbon chains connecting electrodes (analytical approach). Dragging in linear bridges.
b. United transport in graphene molecules of various kinds, free and contacting with leads. Calculation.
c. Electron-vibron interaction in carbon tubes of various radii. Short fragments. Free and contacting with leads.

1.3.1b. Phonon dynamics and thermal properties of free armchair carbon nanotubes

Report-3a: "Strategies to Increase Thermal Conductivity. Enhancement by Optical Phonon Sub-Bands Engineering in 3-D Nanostructures Based on C and BN Nanotubes"

Content

VIII. Introduction

IX. Phonon dynamics in an armchair carbon nanotube

X. Generalized equation of thermal conductivity in armchair single-walled nanotube

XI. Thermodynamics and statistics for a carbon nanotube

XII. Summary and discussion

XIII. References

XIV. Attachment - Short investigation plan

I. Introduction

The content of Report-3a presents the third stage of the investigation of phonon fluxes in carbon and BN nanostructures in the framework of the tasks for "*Strategies to Increase Thermal Conductivity. Enhancement by Optical Phonon Sub-Bands Engineering in 3-D Nanostructures Based on C and BN Nanotubes*".

Here, dynamics (planned point 1c, see attachment), heat transfer problem for closed carbon nets – armchair tubes (point 2c) and macroscopic manifestations (point 3c) are presented. Two main tubulene geometries: zigzag and armchair are compared with respect to phonon eigenstates, density of states, vibration amplitude distribution and thermal conductivity.

The idea of the PQDM approach proposed before is to use a discrete microscopic model for phonon dynamics of relatively small molecular fragments approximately of phonon mean free path (MFP) sizes.

The dynamics of such a cluster may be described classically in Born approach [1, 2] and all the important data may be obtained: eigenfrequences, density of states and phonon amplitude distribution inside the molecular fragment during its lifetime. Neighboring parts of the nanotube are in an uninterrupted process of exchange by phonons. Due to the weak fragment-surrounding medium interaction, the process may be described by Fermi's "golden

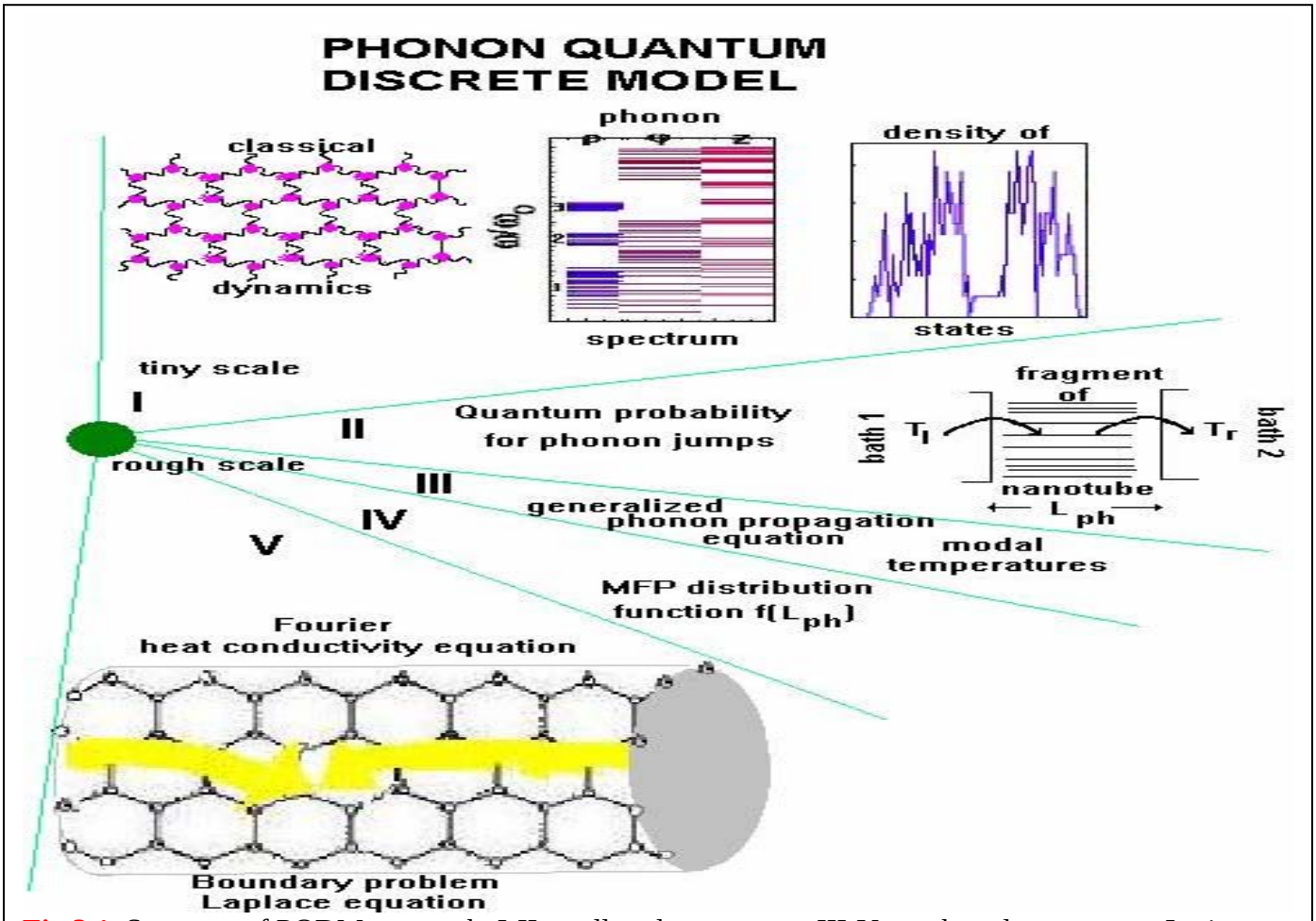

Fig.2.1. Structure of PQDM approach. I-II small scale processes, III-V rough scale processes. L_{ph} is phonon mean free path. I stage, classical dynamics, atomic scale; II stage, phonon jumps between nanotube areas. III stage, transition to averaging, The notion of statistical temperature erases at IV stage. V stage , macroscopic thermodynamics and kinetics.

rule" which determines the value of the transfer rate. This quantum characteristic is a transport processes consideration that enables the introduction of a microscopic thermal conductivity coefficient that depends on the temperature difference between opposite sides of the fragment in contact with the baths. An averaged classical picture of phonon energy (heat) transport and temperature distribution along pulled carbon nanotubes and other kinetic and statistical phenomena may be obtained in rough space scale. The rough scale leads to the generalized phonon kinetics equation describing heat propagation in 2D molecular nets.

The general scheme of the developed PQDM approach is shown in Fig.1.1. The tiny scale stages (I-II) involve classical dynamics on the atomic level and weak phonon-phonon transformations and jumps. The parameters of this model are the elastic constants determined from atom-atom quantum-mechanical potentials, the geometry and symmetry of the system, the lattice constants, and the phonon-phonon interaction constant. At this level processes are ballistic. **The discrete system of contacting separate atoms vibrates and the complicate motion is represented as the superposition of modes that group into three branches**. **Each mode (=degree of freedom=standing wave) is described by the eigenfrequency and distribution of atomic amplitudes inside the corresponding standing wave**. **On the second stage, phonon standing waves jump between neighboring areas along the nanotube. Due to the actual "compactification" of circular degrees of freedom (φ) the phonon motion is a purely one-dimensional process (Report-2a). The rough scale processes occur on distances of the order of (or slightly greater than) phonon mean free path lengths (L_{ph}) (stages III-V). The transition to averaging (stage III) gives a picture for phonon population along the molecular system. If the phonon-phonon interaction is elastic, there arise local or modal temperatures describing thermodynamic equilibrium between phonons of a given mode. The notion of statistical temperature is erased at stage IV when the averaging of different phonon mean free path lengths is performed. After the transition to a macroscopic description (stage V), the ballistic processes vanish and macroscopic thermodynamics and kinetics can be used.**

Taking the phonon band structure and dividing by different phonon branches has significant meaning in describing thermal conductivity. This investigation shows a dominating contribution from the radial branch of vibration in heat propagation in zigzag NT and graphene sheets. The radial breathing mode (RBM) was investigated experimentally and theoretically in [3-5]. The mean frequency of RBM vibrations was estimated there within the interval (100-300)cm^{-1} that corresponds to estimations made here for the radial phonon band width (0.004-0.007)eV for graphene and single walled zigzag nanotubes.

Phonon engineering of low-dimensional structures and heat conductivity properties of nanotubes are actively discussed in physical literature [6-8]. Establishing a concrete law for the temperature dependence of thermal conductivity at high temperatures as well as a law for the increasing at low temperatures is among the most common current problems. Different sources give the data for maximal thermal conductivity for a solitary carbon tube in a wide interval from 200 W/mK to 3000 W/mK. The temperature of maximal thermal conductivity for many carbon tubes also varies within a wide interval from 150 K to 300 K from different authors. Another point of interest is the differences in thermal conductivity for solitary carbon tubes depending on type (armchair or zigzag), chirality and size.

Phonon dynamics and kinetics in tubes with armchair geometry and zero-chirality are considered below and compared with data for zigzag nanotubes.

I. Phonon dynamics in an armchair carbon nanotube

Linear approximation in phonon dynamics is based on the supposition that small atomic vibrations have harmonic character at least in the case of not too high temperatures. It means that the potential iso-energy l surface in the vicinity of atomic equilibrium positions has an ellipsoidal form. Classical motion of atoms near their equilibrium points is described by elastic constant *k* that characterizes atom-atom bonds in the Born approximation. In this investigation, nonzero elastic constant *k'* << *k*, from the framework of linear approximation, is used for atomic shifts perpendicular to the bond. The symmetry of carbon structures dictates three main types of vibration (radial ρ-mode, tangential φ-mode and axial z-mode)

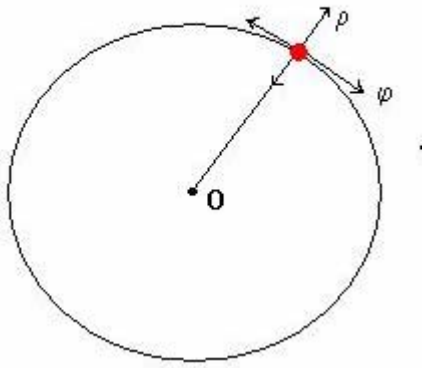

Fig.2.1 The problem's geometry. Z-axes is perpendicular to the figure plane. It's shown φ and ρ shifts of an atom.

Fig.2.1.

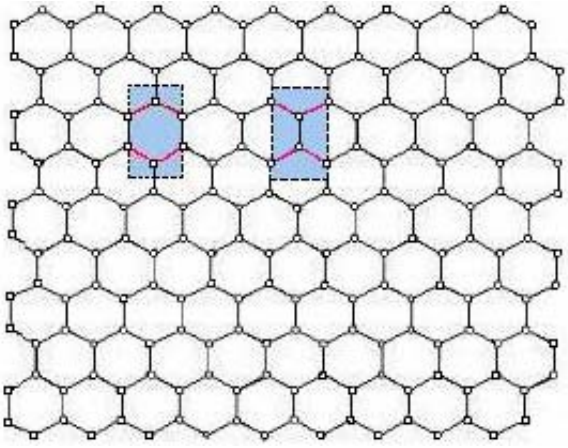

Fig.2.2. A fragment {9,9}of hexagonal lattice. Shaded are two equivalent conventional elementary cells containing four atoms. Two types of bonds are presented by different colors. Rolling around horizontal axes could be implemented only for even number horizontal rows {8,9}

It should be noted that the principal difference between the vibration branches originates from the direction of bonds relative to the direction of the axes of symmetry associated with the given degree of freedom (Fig.2.2). This difference manifests itself in the phonon band structure for the tangential and axial branches in the case of pure zero-chirality. In the presence of helicity the difference vanishes. In Fig.2.3 (the case with non-zero chirality), the situation when the tangential φ-mode and axial z-mode have approximately equal orientation shifts relative to both red and blue bonds inside a chosen elementary cell is presented.

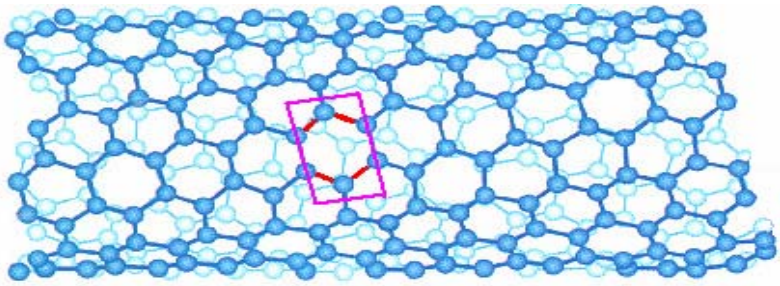

Fig.2.3. Fragment of armchair tubulene (10,5) with non-zero chirality created from a graphene sheet {14,10} by rolling up around the armchair direction. Picked out is the conventional elementary cell containing four atoms. Two types of bonds are marked by different colors.

Dynamical equations for all three branches of vibrations can be calculated taking into account that the motion of each atom is three-dimensional. The zero-approximation

approach supposes that the radial ρ-mode, tangential φ-mode and axial z-mode should be considered independently.

Consider an armchair tube (n,0) produced from the fragment shown in Fig.2.2 by rolling around horizontal direction without any shift. In this case each of the tube fragments is connected with the same fragments. Therefore, contrary to the case of flat fragments connected to the external media, all atomic positions along with their bonds are described by the same dynamical equations. The difference exists between different vibration types or branches only.

For shifts directed normal to the tube surface the equation is the following:

$$\{ m\ \ddot{\rho}_i = -k'(3\rho_i - \rho_{i1} - \rho_{i2} - \rho_{i3}),$$

(2.1)

where i_1, i_2, i_3 are indexes for atom i neighbors. Atomic coordinates are not important here. The universal atomic number i is defined using its position in the row and column of the initial flat fragment creating the tube. This type of vibration is called the radial breathing mode (RBM) in literature [3-5].

For tangential atomic shifts, taking into account the atom space coordinates on the tube surface $x=\varphi R$, where R is the tube radius and φ is the azimuth angle, the armchair case with the absence of chirality is described by the system:

$$\{ m\ \ddot{x}_i = -k(x_i - x_{i1}) - 0.25k(2x_i - x_{i2} - x_{i3})$$

(2.2)

where coefficient 0.25 characterizes two weak bonds for this vibration.

For axial atomic shifts we have

$$\{ m\ \ddot{z}_i = -0.75k(2z_i - z_{i1} - z_{i2}) - k'(z_i - z_{i3})$$

(2.3)

The matrix structure of all equations (1-3) corresponding to the armchair (n,0) case is shown in Fig.4.

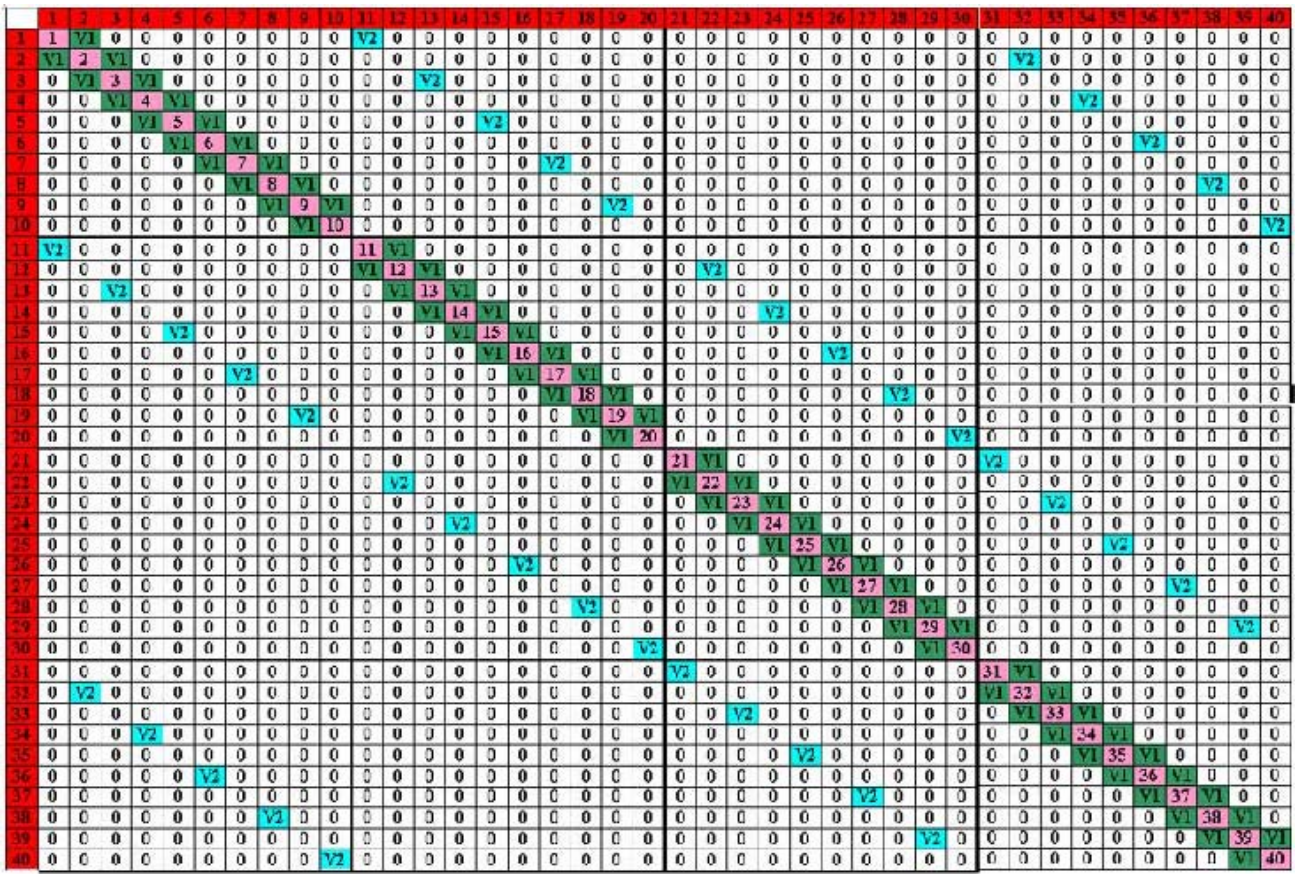

Fig.2.4. Sketch of the dynamical matrix for armchair tubulene created from a graphene sheet {5,5} containing 60 atoms by its rolling up. Rose-colored spots are diagonal elements, green and blue show two types of bonds, rest elements equal to zero, left and upper red bands contain atomic numbers.

Armchair tubulene matrix and vibration amplitudes

Atomic coordinates become important when the mode amplitude distribution is presented in the space. The vibration amplitudes for mode s=5 of any type are shown in Fig.2.5. As in the case of zigzag NT, there are considerable differences in amplitude distribution over the armchair tube surface compared to the open carbon net. The differences are caused by the changed topology of the system. A difference exists between the frequency of modes and density of states at the same state but it is not essential.

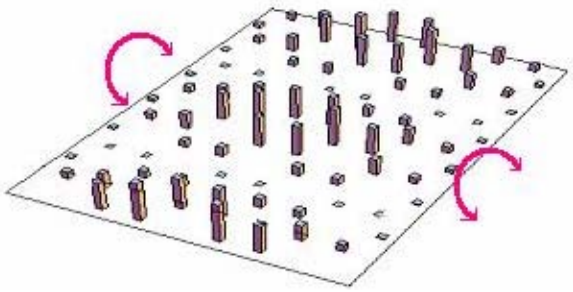

Fig.2.6. ρ-branch amplitude distribution along zigzag tubulene created from a graphene sheet {6,5} by rolling up around marked direction. 5th state. Longitudinal knot's lines are degenerated.

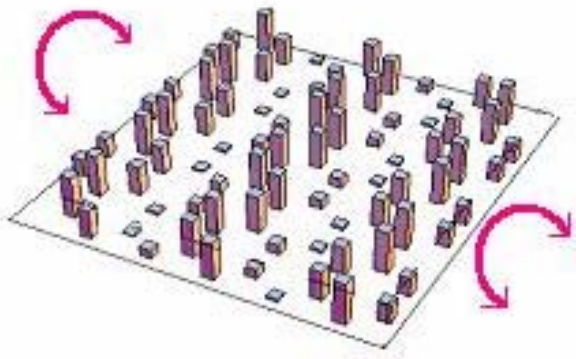

Fig.2.5. Calculated ρ-branch amplitude distribution s=5 along armchair tubulene created from a graphene sheet {6,5} by rolling up around marked direction. Transversal knot's lines are degenerated.

The calculations performed with the system of equations (1-3) give $|C_{si}|^2$ for eigenvectors which is a well known standing wave picture with the corresponding number of knot's lines depending on the state number *s*. Increasing the number of states leads to the formation of lateral (parallel to z-axes) and transverse (circular) knot's lines dividing the tube's surface. Fig.2.5 illustrates the well known knot's theorem for the 5th (or *r*-4th) state where two twice degenerated knot's lines cross circularly to the tube's surface. Increasing the

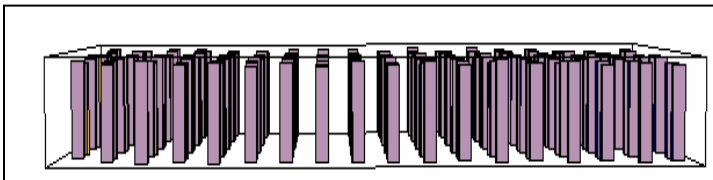

Fig.2.7. Calculated mean square amplitude distribution along armchair tubulene created from a graphene sheet {15,5} by rolling up around marked direction. T=0.03 eV. Circular arrows show rolling up of the structure.

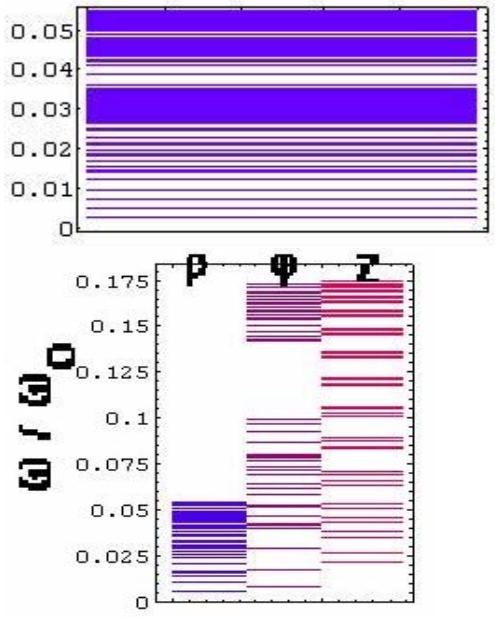

Fig.2.8. **Lower part.** Three branches of phonon spectrum for armchair tubulene created from a graphene sheet {8,15} by rolling up around z-axes. **Upper part.** Radial phonon band for zigzag {8,15} NT.

tube's length leads to a considerable change in the picture of vibrations. The same 5th (or r-4th) state in the zigzag case, presented in Fig.2.6, has knot's lines perpendicular to those of the armchair case.

The mean vibration amplitudes A_j, averaged for the state populations n_s, are almost constant and do not deviate sufficiently along the tube surface. There is a difference in zigzag nanotubes where $|C_{si}|^2$ decreases from the lateral ends to the middle axes of the nanobridge.

$$A_j = \sum_{s,\sigma} \left| C_{sj} \right|^2 n_{s\sigma} \quad , \tag{2.4}$$

where $n_{s\sigma}$ is the population of s, σ state, j numbers atoms situated on the tube surface and C_{sj} is the s-state probability amplitude at j-position of the net. Coefficients C_{sj} are the components of eigenvectors arising as the solution of systems (1-3). Mean square amplitudes calculated for temperature T=0.03eV by expression (4) are shown in Fig.2.7. The averaging was made here over all phonon σ-branches. One can see that in contrast with flat carbon terminated nets with free edge atoms (Report-1b) and to some extent zigzag carbon tubes (report-2b), the closed armchair structure has almost constant amplitudes along all directions over the surface of the tube.

Phonon mode frequencies are obtained from expressions (1-3) as eigenvalues. In Fig.2.8, three branches of the phonon spectrum for an armchair tubulene having 8 honeycombs in the circumference are presented.

<u>Armchair tubulene spectrum and DOS</u>

The density of states may be approximately defined by the following expression.

$$g(\omega_{s\sigma}) = \frac{\partial N_{s\sigma}}{\partial \omega_{s\sigma}} \tag{2.5}$$

This transforms into an exact equation if the number of degrees of freedom becomes large enough. Here, $N_{s\sigma}$ numbers phonon states with frequency $\omega_{s\sigma}$. More correctly, the density of states function may be calculated providing preliminary state grouping and density determination inside each group.

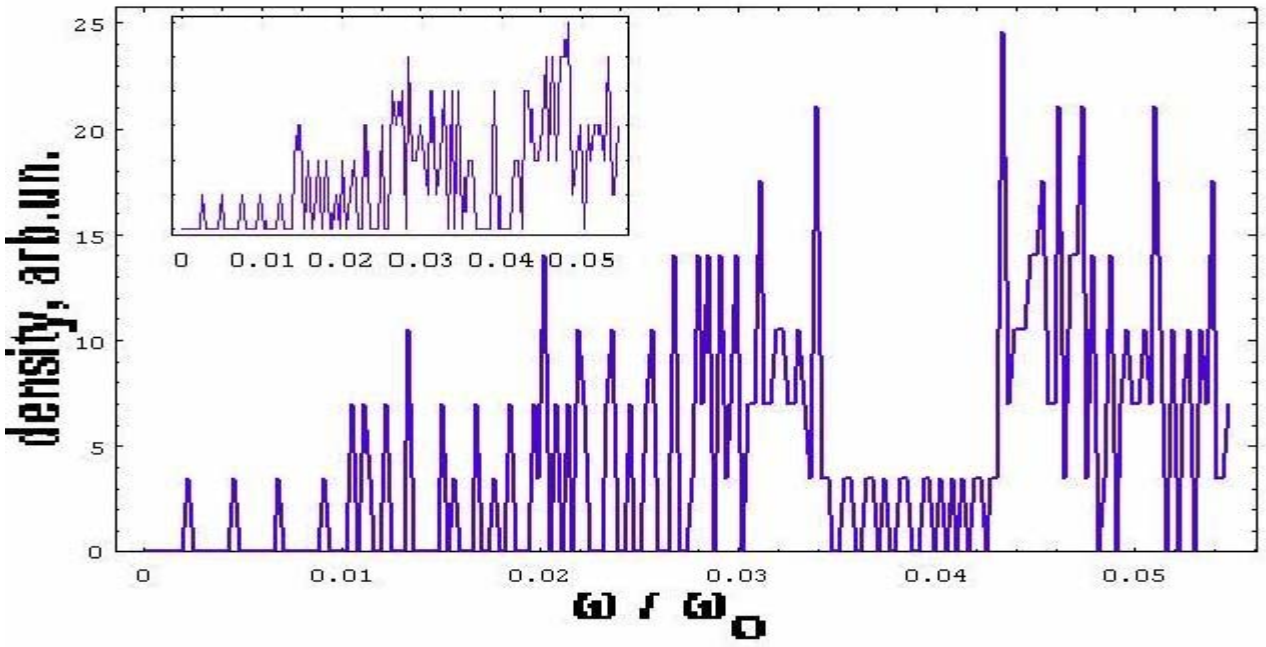

Fig.2.9. Radial mode density of states for armchair tubulene created from a graphene sheet {8,15} by rolling up around z-axes. Insertion the same for zigzag tubulene.

DOS with preliminary state grouping have been calculated by dividing the whole frequency band interval into h=Int[4r/5] sub-intervals (or near this value) within which the number of eigenmodes were counted. The frequency spectrum and DOS function in the zero chirality armchair nanotube case are presented in Figs. 9-11. Fig. 9 was obtained by numerical calculation of system (1) described by the matrix of eigenvalues problem shown in Fig.2.4.

The comparison between results obtained for armchair tube radial mode spectrum and DOS functions for a zigzag tube and a graphene fragment with the same number of atoms shows the absence of any significant differences.

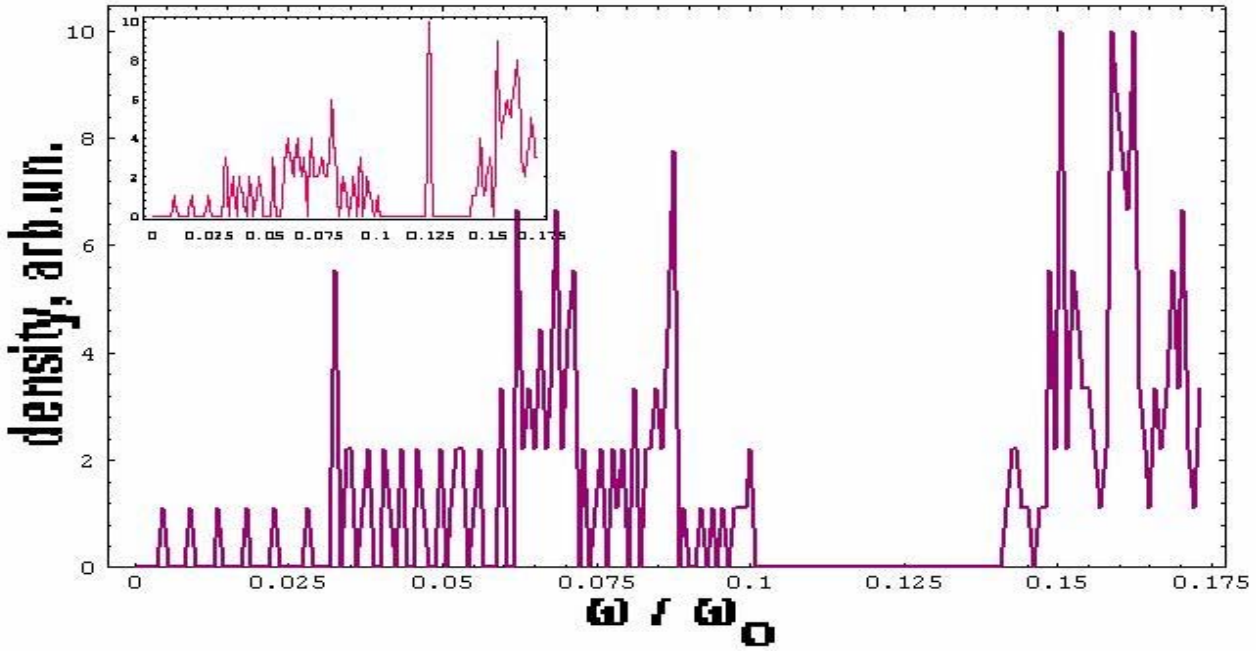

Fig.2.10. Tangential φ-mode density of states for armchair tubulene created from a graphene sheet {8,15} by rolling up around z-axes. Insertion is zigzag equivalent for this that is z-mode DOS. h=Int[4r/5].

Thus, the process of rolling a sheet up into a tube does not influence the spectrum and density of states in this type of vibration case. But the distribution of vibration amplitudes (Fig.7) differs from that for graphene (see Report-1b, Fig.3, Fig.9a, Fig.9b) where the mean vibration amplitudes of the sheet's free edges were bigger than that in the middle.

The density of states frequency function for the tangential branch of vibrations calculated with equation (2) is shown in Fig. 2.10. The insertion shows the result of numerical calculations performed before for the φ-branch in an armchair geometry equivalent to the z-branch in a zigzag NT. Note the narrow subband near $0.125\omega_0$ (see insertion) that plays the role of a characteristic "mark" for the changed topology of the system. This subband contains *2*n* levels in the middle of the gap that occur because the new topology now permits circular standing waves z-type vibrations that were forbidden before in the plane structure. In the armchair geometry, circular atomic chains are absent (for φ-type vibrations) and the middle-gap subband vanishes again.

Comparing results obtained for zigzag and armchair tubes for the DOS function shows some differences. The subband inside the gap (see insertion) originates from circular chains of equivalent atoms in zigzag geometry while for armchir geometry the circles are absent. On the other hand, graphene z-branch DOS is very similar to tangential armchair due to the absence of circular symmetry.

The frequency spectrum for z-branch modes calculated from the system of equations (3) is shown in Fig.2.11.

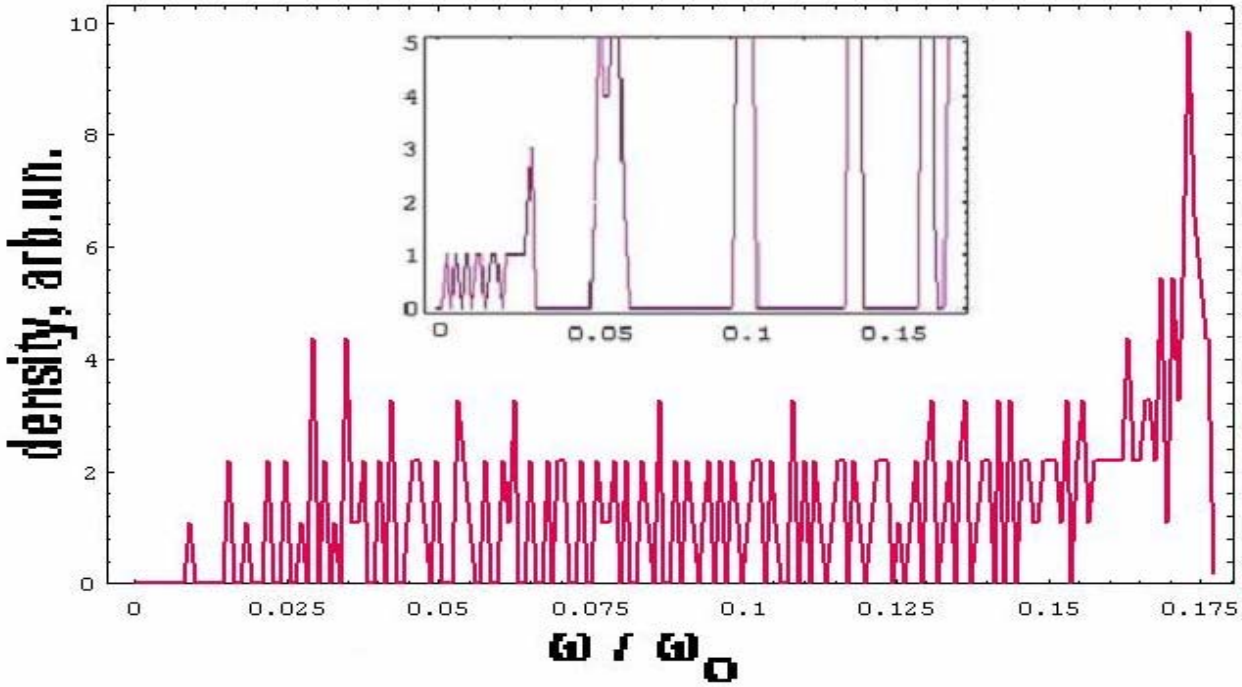

Fig.2.11. Axial z-branch density of states for armchair tubulene created from a graphene sheet {8,15} by rolling up around z-axes. Insertion is zigzag equivalent for this that is φ-mode DOS.

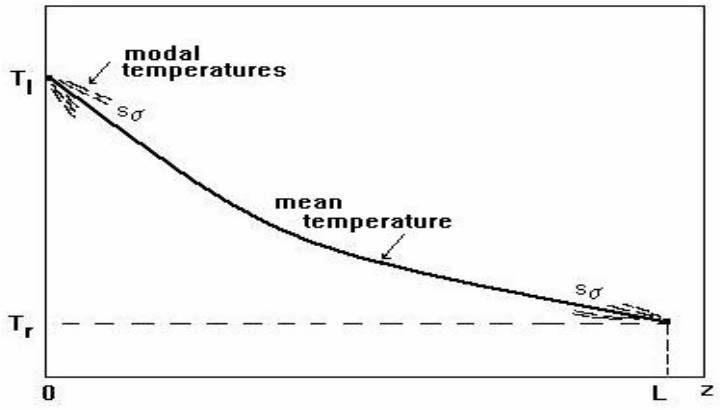

Fig.3.1. One dimensional phonon dynamics. Exact temperature distribution along the tube given by (4.4). T_l ,T_r.are temperatures of baths connecting with tube ends, L is the tube length. End points come together all modal (partial) temperatures for each sσ.

II. Generalized equation of thermal conductivity in a single nanotube

The PQDM analysis proposed in Report-1b consider heat processes from "first principles" both using microscopic characteristic on quantum level including phonon jump probability, phonon-phonon interaction, calculated spectrum and amplitudes distribution along the structure and macroscopic

kinetic approach operating by length of phonon decoherence l_{ph} or phonon mean free path. The time of the phonon state establishing in area l_{ph} x $2\pi R$ is much less than the phonon lifetime. The latter is determined by phonon-phonon scattering and may lay in interval (10^{-8}-10^{-7})s [2]. This supposition allows one to consider propagation of phonons as a sequence of jumps from one fragment to another with relatively long life on each one. In a tube of not too big radius R the phonons propagate by jumps between mean free path-sized areas. Neighboring areas play a role of leads having some fixed temperatures. Taking into account that phonon scattering processes are weak ones we have obtained generalized equation of phonon dynamics (Report-1b, paperzd-a.doc). In 1D case it has the form

$$\frac{\partial n_{s\sigma}}{\partial t} = D_z^{s\sigma} \frac{\partial^2 n_{s\sigma}}{\partial z^2} \qquad \textbf{(3.1)}$$

Temperature distribution along the tube

The phonon mean free path l_{ph} decreases with increasing of temperature. Evaluations made in different sources give interval from hundred Angstroms to several micrometers at room temperatures. In any case azimuthal phonon motion may be considered as ballistic one and jumps or diffusion in tubes may occur only in axial direction. In relation to phonon propagation nanotubes embody an ideal one-dimensional system. In stationary case it is ease to write the exact solution of the one-dimensional equation (1) if to start from generalized equation written for populations $n_{s\sigma}$ (Report-2b).

$$T(z) = \omega_{s\sigma} / Ln\left(1 + \frac{L}{n_l(\omega_{s\sigma}) + [n_r(\omega_{s\sigma}) - n_l(\omega_{s\sigma})]z}\right) \qquad \textbf{(3.2)}$$

Here L is tube's length, z is axial coordinate along the tube, n_l n_r are population numbers $n_{s\sigma}$ taken at left and right temperatures of both tube ends T_l ,T_r. Indeed on the macroscopic level local populations n_l n_r obeys equilibrium Planck law. The approximate behavior of temperature distribution is shown in Fig.3.1. The bundle of partial modal temperatures comes together in end points. With increasing of temperature all modal dependences become equal. The difference may be essential at low temperatures.

Thermal conductivity and phonon mean free path

Thermal conductivity was calculated here in PQDM approach for tubes of armchair geometry by expression obtained in previous reports 1b and 2b.

$$\lambda'(l_{ph}) = \frac{2\pi l_{ph}}{T^2} \sum_{s,\sigma} \left|G_{ls}\right|^2 \left|G_{rs}\right|^2 \omega_{s\sigma}^2 g(\omega_{s\sigma}) \frac{N(\omega_{s\sigma})(N(\omega_{s\sigma})+1)}{\left|G_{ls}\right|^2 + \left|G_{rs}\right|^2},$$

(3.3)

where l_{ph} is phonon mean free path, square modulus reflect connections of end atoms of the tube fragment with the rest part of the tube.

$$G_{ls} = \sum_{i_l} G_{i_l} C_{i_l s}$$

(3.4)

Left and right end atoms numbered i_l and i_l were taken into account with its bonds orientations. Formula (3) is a partial case of obtained in Report-1b expression (16) for thermal conductivity when left and right DOS functions coincides with own density of states $g_r = g_l$.

The l_{ph} is playing here in some sense the double role. From the one side it dictates the length of tube fragment where phonon states occur in ballistic regime. For an armchair tube made from a graphene sheet {n,m} we have $l^2_{ph} = 3m^2a^2/4$, where a is the bond length. In accordance with PQDM approach l_{ph} coincides with the length of calculated fragment with phonon standing waves inside. In contrary, DOS function $g(\omega_{s\sigma})$ describes the left (=right) medium. From the other side l_{ph} depends on phonon-phonon collisions that in own turn depend on the temperature.

It is worth to evaluate temperature dependence of l_{ph}. General expression for phonon mean free path is given by the surface density of phonons S/N.

$$l_{ph} \approx \sqrt{\frac{S}{N}} = \sqrt{\frac{l_d \cdot l_{ph}}{N}} \qquad l_{ph} \approx \frac{l_d}{< N >},$$

(3.5)

$$< N > = \frac{1}{\Delta} \int n(\omega)\, g(\omega)\, d\omega$$

(3.6)

where S is the tube surface where phonons propagate, l_d is the tube circle length, Δ is the phonon band width and <N> is mean number of phonons. Taking into account that $<N> \propto T$ we have

$$l_{ph} \sim \frac{1}{T}$$

(3.7)

Implicitly l_{ph} is contained in upper limit of summation in (3), in $|G_{ls}|^2$ and in $g(\omega_{s\sigma})$. The size dependence for armchair tubes of given diameter and at given temperature was calculated by (3). The Fig.3.2 presents typical picture of quadratic increasing for λ vs phonon mean free path.

$$\lambda \sim l_{ph}^2$$

(3.8)

Relations (7), (8) contain an explanation for the well-known experimental fact of thermal conductivity temperature damping at high temperatures by $1/T^2$ law. This phenomenon is observed both in 3D and low-dimensional systems. Proposed here PQDM approach gives a simple opportunity to connect heat propagation with the definition of phonon mean free path.

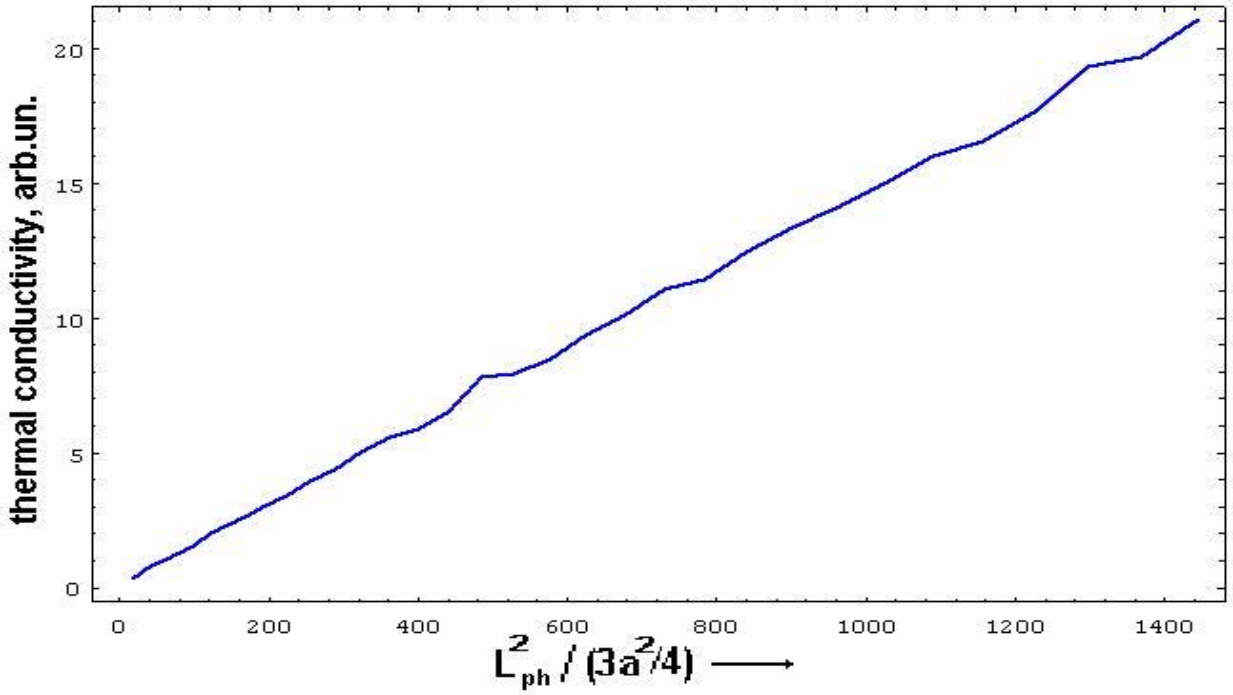

Fig.3.2. One dimensional phonon dynamics. Calculated total thermal conductivity length dependence that includes all vibration branches of armchair NT. L_{ph} is phonon mean free path, a is carbon bond length.

The thermal conductivity dependence on the radius of SWNT is also approximately quadratic (Fig.3.2, insertion).

The result of thermal conductivity numerical calculations for radial, azimuthal and axial phonon branches (σ=1,2,3) is presented in Fig.3.3. It is easy to see that the sum on all σ will be very close to curve 1 connecting with radial ρ-band (Fig.3.4). The unity λ_0 determined from (3) and formula (16) from Report-1b is measured in *W·m/K*

$$\lambda_0 = \frac{2\pi a G_0^2}{\hbar \omega_0} k \quad , \qquad \textbf{(3.9)}$$

where *a*=1.2 Angstrom is unity of length, *k* is the Boltzmann constant, ω_0 is accepted here phonon energy unity and G_0 is the constant of phonon-phonon interaction. Evaluations using data of [8] and [9] give for
characteristic phonon energy very wide interval $\omega_0 \in$[0.8-1.6]eV.

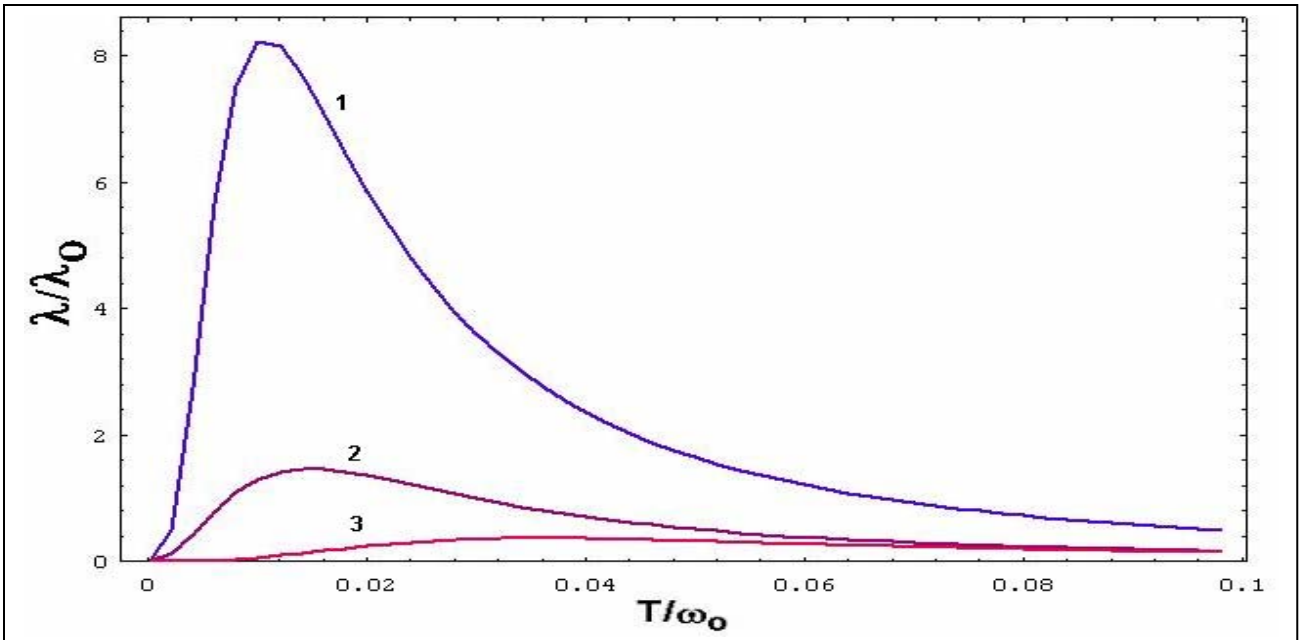

Fig.6 *. Thermal conductivity temperature dependence. Armchair NT. Curve 1 corresponds to z-branch contribution, curve 2 to φ-branch and ρ-branch contribution is presented by curve 3.*

It should be noted that the weak temperature dependence also has the structure constant (bond length *a*) of the system. Thermal expansion of single walled nanotubes was investigated in [10] but the result obtained there for radial expansion is not a reliable one and deviates from negative to positive values. Elastic constants and the constant of phonon-phonon interaction G_0 depend on the temperature too.

The maximum is situated near $1.5\omega_0$ both in armchair (Fig.3.4) and zigzag case (Report-2b, Fig.13). It means that the difference between two geometries exists only on the dynamical level of tiny scale processes and vanishes after the transition to rough scale processes. The insertion to Fig.3.4 presents the law of initial temperature rising of thermal conductivity at low temperatures. Our conclusion $\lambda \sim T^2$ for an isolated SWNT coincides with experimental data obtained in direct measurement for MWNT by [11] and is in contradiction

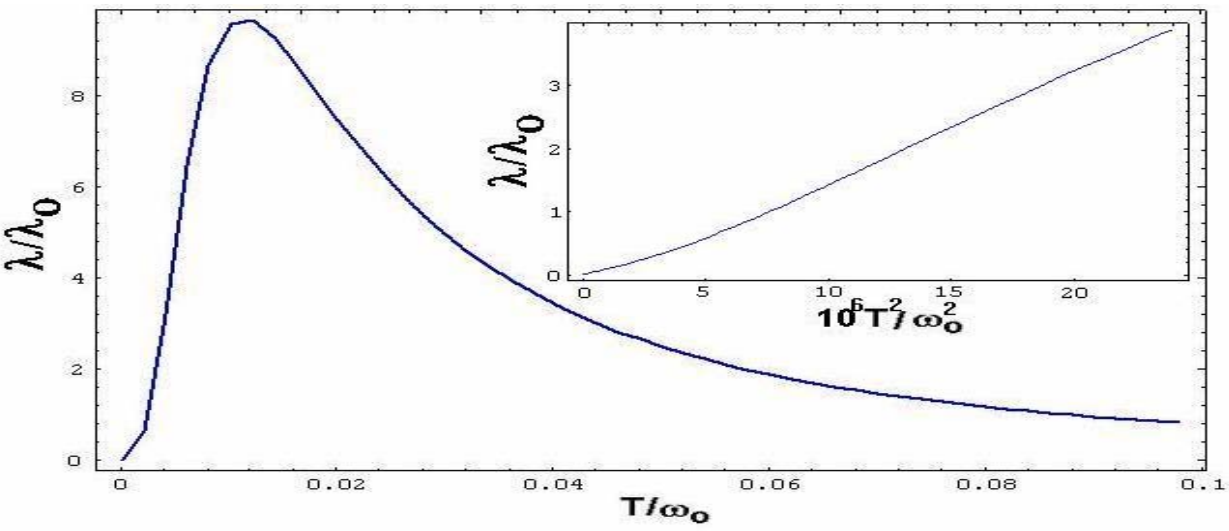

Fig.3.4 . Total thermal conductivity temperature dependence. Armchair NT. Eight honeycombs along the circumference. Insertion: the law of increasing at low temperatures: $\lambda \sim T^2$, $T \in (0, 0.005)\omega_0$.

with linear temperature law obtained in [12] for SWNT bundles.

The conclusion that the radial mode contribution to heat transfer is dominating in the temperature interval under consideration is based on the supposition that the phonon-phonon interaction constant G_0 (see (3), (4), (9)) participating in end atoms constants G_{il} does not depend on the phonon type (ρ, φ or z). Then due to the large density of states in narrow low-frequency ρ-band comparatively with that for φ- and z-vibrations essential prevail of ρ-vibrations arises. So at actual temperatures ρ-branch of phonons determines heat propagation through single-walled armchair nanotube. The same effect was obtained before and for zigzag geometry too. Of course, the problem of phonon-phonon constants G_0 for different vibration types exists now and should be investigated in detail in following study. It should be mentioned also very important in PQDM starting constant ω_0 that have to be found from comparison with experimental data for isolated SWNT. As well the problem of mean free path distribution function is open and should be investigated more detail.

IV Thermodynamics and statistics of armchair nanotubes

Static thermodynamic characteristics of non-helical armchair nanotubes of different sizes have been calculated. If the system exists in equilibrium state, the atomic heat capacitance $C(T)$ and entropy $S(T)$ are given by the following expressions,

$$C(T) = \frac{1}{r}\sum_{s,\sigma} \omega_{s\sigma} \frac{\partial N(\omega_{s\sigma})}{\partial T} = \frac{1}{rT^2}\sum_{s,\sigma} \omega_{s\sigma}^2 N(\omega_{s\sigma})(N(\omega_{s\sigma})+1), \tag{4.1}$$

where $r=2n(m+1)$ is the number of atoms in a armchair tube of length $1.7ma$ and radius $a/\sin(\pi/n)$.

$$S(T) = \int \frac{C(T)dT}{T} = \frac{1}{r}\int \frac{dT}{T^3}\sum_{s,\sigma} \omega_{s\sigma}^2 N(\omega_{s\sigma})(N(\omega_{s\sigma})+1), \tag{4.2}$$

The calculated temperature dependence for heat capacitance is shown in Fig.4.1.

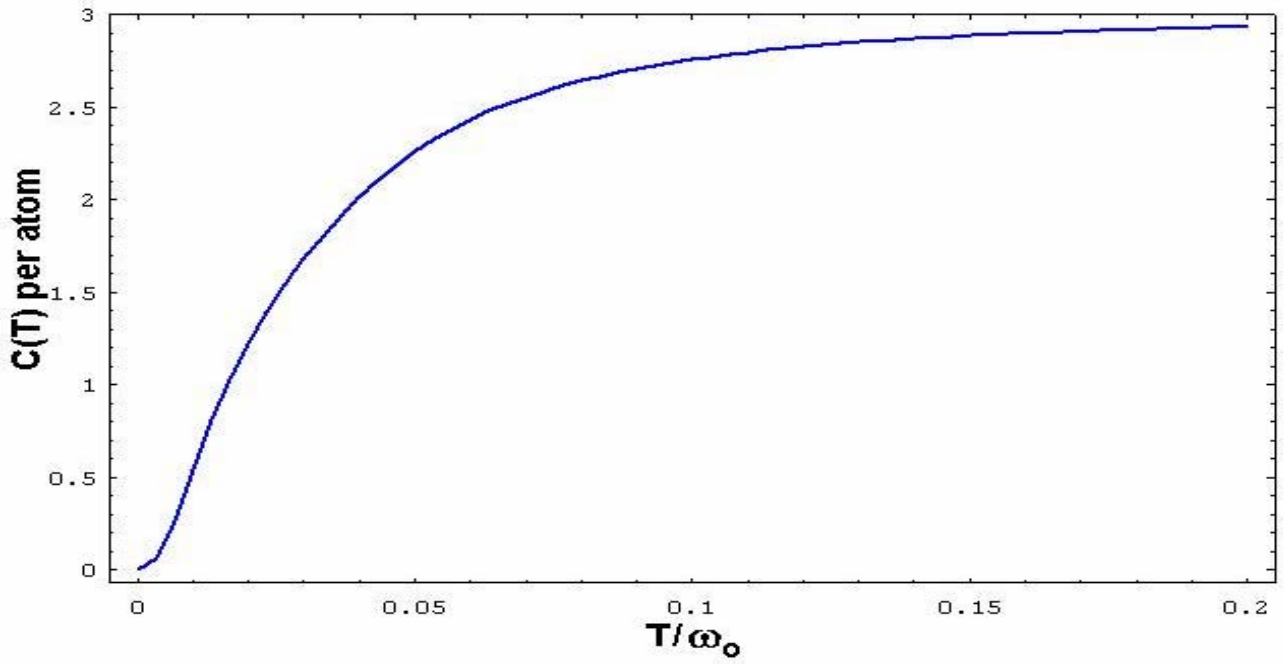

Fig.4.1. Heat capacitance vs temperature dependence for armchair nanotube. Dulong-Petit law and W. Nernst theorem. $\omega_0 \in (0.8, 1.2)$eV.

The curve illustrates the third thermodynamical law (W.Nernst theorem) at low temperatures and Dulong-Petit law at high temperatures ($T>0.1\omega_0$). An absolutely equivalent curve was obtained before for zigzag NT (Report-2b). This means that from a thermodynamical point of view both NT symmetries, armchair and zigzag, are equivalent at all temperatures.

The Dulong-Petit law is a tag in thermodynamics that embodies the classic systems. It is clear from the Fig.4.1 that the notion "high temperatures=classical system" begin to act from $0.15\omega_0$, that is approximately 1400K, for carbon single-walled nanotubes. Thus, in real temperature intervals, single-walled nanotubes are non-classical objects.

The entropy behavior has similar characteristics at low temperatures and shows logarithmic growth at high temperatures both for zigzag and armchair nanotubes.

V. Summary and discussion

A complex approach PQDM applied gives an opportunity to describe dynamics, kinetics and statistics of phonons in carbon nanotubes with zero-chirality. Fig.5.1 illustrates

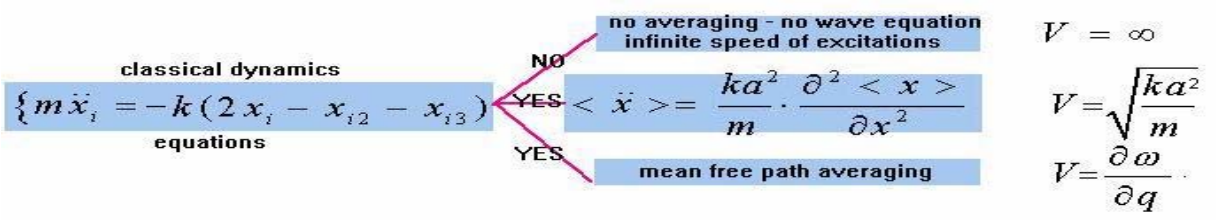

Fig.5.1. Averaging procedures and speed of propagation.
a is interatomic distance, <*x*> is mean atomic shift , *x* is extended coordinate of the freedom's degree, *V* is excitation velocity, *m* is atom mass, *k* is elasticity coefficient.

the important role of averaging procedures in understanding of phonon, sound and heat propagation in low-dimensional atomic nets. The classical dynamical equations don't contain retardation in non-relativistic approach. This causes the infinite speed of vibrational excitation propagation along the net or nanotube (Fig.5.1, second column, upper row).

The first stage averaging is transition to presentation of dynamical equations in the finite differences (second column, middle row). Evaluations by data [9,10] (k=4.65·10^{-12}N/m) and our data [13] give for second row velocity V=18.3 km/s. This value is close to sound velocity in diamond (1,1,0) direction.

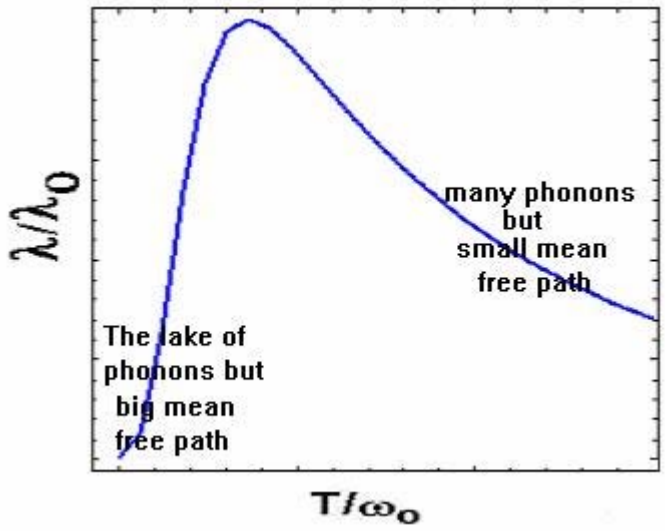

Fig.5.2. Temperature dependence of thermal conductivity coefficient. Two competitive tendencies.

More rough averaging at the phonon mean free path distances is used to describe heat spreading along carbon nets (Fig.5.1, second column, lowest row). Found from RBM frequency band width value of phase velocity $V= a\cdot\Delta_\rho/\pi$ is more than twenty times less (0.85km/s) than for the pure sound.

Atom vibration dynamics was considered for carbon nanotubes of armchair geometry in comparison with the results obtained for graphene sheets. Vibrational eigenmodes, density of states and amplitude distribution for tube fragments of the length up to 40 hexagons were calculated in linear approximation for three types of vibration: athimuthal or tangential φ-mode, radial ρ-mode and longitudinal z-mode.

It's shown that phonon propagation in actual nanotubes is characterized by a kind of "compactification" of circular freedom's degree due to the big phonon mean free path. Nanotubes of actual diameters are ideal one-dimensional phonon qnd heat conductors.

Phonon band structure was investigated for armchair nanotubes on the base of hierarchical law and system symmetry.

Thermal fluxes and thermal conductivity were considered in PQDM. Temperature dependences were obtained. The mechanism of heat conductivity high temperature damping is reflected in Fig.5.2. Two competitive tendencies produce thermal conductivity maximum at intermediate temperatures (100-300)K.

The exact solution of generalized thermal conductivity equation was obtained for nanotubes. Temperature distribution along the tube was derived analytically.

Size dependences were considered for thermal conductivity. It was shown the linear increasing of heat conductivity with the growth of the phonon mean free path.

Statistical properties were investigated. Heat capacitance and the entropy of carbon linear tubes were calculated as the function of temperature.

Our theoretical approach (Fig.1.1) explains the nature of good thermal conductivity in carbon and carbon-like materials by existing of the soft vibration branch (low frequency RBM phonons with high DOS at thermal energies) accompanied by structure hardness (high frequency φ- and z-branches) providing big mean free path for phonons (Fig.5.2).

Adding of new layers or new walls to single-walled NT makes breathing ρ-branch of vibrations harder. That causes the sharp decreasing of phonon density of states at the same phonon mean free path. Phonons leave the active thermal zone and heat conductivity decreases. Therefore, atomic monolayers and isolated single-walled nanotubes have to be champions in thermal conductivity. Uniting SWNT into the tight bundles quenches breathing mode too. PQDM approach predicts the sufficient worsening of thermal conductivity in SWNT tight bundles comparatively with free SWNT. The way of thermal conductivity enhancement in this case is "dissolving" of inter-tubes bonds and turning out tight bundles into the system of almost free tubes.

Pressure decreases thermal conductivity [14]. The effect is connected with total hardening of all bonds and phonon modes going away from active thermal zone.

Melting decreases thermal conductivity by another reason: the phonon's mean free path becomes small.

In conclusion we mark that the problem of creating "heat superconductors" may have a perspective on the way of hardness-softness uniting. It seems, the natural limit is given by isolated fragments of carbon-like structures: carbon sheets and single-walled nanotubes. The question is in the existing of possibility to create more complicate artificial heat superconductivity aimed systems.

VI. References

13 M.Born, K.Xuang **Dynamical Theory of Crystal Lattice.** London: Oxford Univ.Press, 1954.

14 R.Berman, **Thermal conductivity in solids,** Clarendon Press, Oxford, 1976.

15 V.N.Popovl, L. Henrard **Evidence for existence of two breathing-like phonon modes.** Phys.Rev., **B63**(23), 233407 (2001).

16 P.Dubot, P. Cenedese **Modelling of molecular hydrogen on Li adsorption on single-wall NT.** Phys.Rev., **B63**(24), 241402 (2001).

17 A.G.S. Filho, A.Jorio, J.H. Hafner. **Electronic transition energy… .** Phys.Rev., **B63**(24), 241404 (2001). Phys.Rev.Lett, **86**, 1118 (2001).

18 J.Chen, **Phonon heat conduction in nanostructures** Int.Journ.Therm.Sci., **39**(4), 471-480 (2000).

19 A.Balandin, A.Khitun, J.Chen, **J.L.** Liu; K.L. Wang, T. Borca-Tascuic. **Optimization of thermoelectric properties of low-dimensional structures via phonon engeneering.** Proceedings of 18th Int.Conf. on Termoelectricity, p189-192 (1999).

20 D.G.Cahill, W.K. Ford, K.E.Goodson; G.D.Mahan, A.Majuindar; H.J.Maris, R.Merlin, S.R.Philpott, **Nanoscale Thermal Transport.** J.Appl.Phys., **93**(2), 793-818 (2003).

21 J.Yu, R.K.Kalia, P.Vashishta. **Phonons in graphitic tubules: a tight binding molecular dynamics study**. J.Chem.Phys. **103**, 6697-6705 (1995).

22 Yu.Maniwa et.al **Thermal expansion of single-walled carbon nanotube bundles: X-ray diffraction study.** Phys.Rev. **B64**, 241402 (2002)

23 Shi, Li; Kim, Philip; McEuen, Paul L.; Majumdar, Arunava. **A microdevice for measuring thermophysical properties of nanowires and nanotubes.** Proceedings of the ASME Heat Transfer Division, Volume **1**, 359-362 (2001).
24 M. Llaguno, J. Hone, T.Johnson, J. E.Fischer, **Thermal properties at single wall carbon nanotubes: diameter and annealing dependence. management** Preprint Archive, Condensed Matter (2001), arXiv:cond-mat/0108142
25 E.Ya.Glushko, V.A.Khrisanov, **Vibrational modes of the terminated atomic chain.** Low Temp.Phys., **23**(11), 910-916 (1997).
26 S. Anderson, L.Dzavadov, **Thermal conductivity and heat capacity of amorphous SiO_2 :pressure and volume dependence.** J.Phys.: Cond.Matter, **4**(29), 6209-6216 (2001).

VIII. Attachment: Short investigation plan

2. Phonon(vibron) bands. Direct calculation in elastic approximation.
- a) Graphene molecules of various kinds, free and contacting with two leads. Influence of the number of bounding atoms on phonon structure.
- b) Phonon structure of 3-polar and 4-polar molecular bridges.
- c) Carbon tubes of various radii. Short fragments. Free and contacting with leads.
- d) BN- flat structures. Free and contacting.
- e) BN-tubes of various radii. Short fragments. Free and contacting with leads.
- f) More complicate geometry. Torus. Two wall C-tube as a heat conductor.

2 Heat transport investigation in PQDM.
- a. Linear carbon chains connecting electrodes (analytical approach)
- h) Graphene molecules of various kinds contacting with leads. Calculation.
- i) Carbon tubes of various radii. Short fragments. Free and contacting with leads.
- j) BN- flat structures. Free and contacting.
- k) BN-tubes of various radii. Short fragments. Free and contacting with leads

3 Macroscopic manifestations of phonon propagation in carbon nets.
- a. Generalized 2D and 3D equation of thermal conductivity in carbon nets.
- b. Boundary problem and temperature distribution in macroscopic carbon nets.
- c. Boundary problem for heat conductivity in carbon and BN tubulenes and temperature distribution along tubulene bridge..
- d. Carbon tubes of various radii. Short fragments. Free and contacting with leads.

4 Phonon-phonon effects in charge and heat transport.
- a. Spectrum modification due to phonon-phonon processes;
- b. Non-linear transport through flat carbon structures;
- c. Non-linear transport along carbon tubulenes;

5 Thermodynamics and statistics of closed and open carbon nets
- a) Statistical sum and entropy of carbon nets (graphene and tubulene).
- b) Heat capacitance of graphene and tubulene structures

6 Heat-transistor effects.
- a) Three pole systems
- b) Four pole systems

7 Electron-phonon effects in charge and heat transport.

a) Transport through linear carbon chains connecting electrodes (analytical approach). Dragging in linear bridges.
b) United transport in graphene molecules of various kinds, free and contacting with leads. Calculation.
c) Electron-vibron interaction in carbon tubes of various radii. Short fragments. Free and contacting with leads.

1.3.2. Carbon heat radiators in polymer surroundings

Here we consider the heat transfer problem for a solitary carbon nanotube (NT) inserted into a solid matrix with low thermal conductivity. Phonon eigenstates, density of states and vibration amplitude distribution along the molecule will be investigated for a NT laterally in contact with the continuous external medium. The temperature distribution inside a low-conducting medium containing a high-conducting channel will be calculated in the framework of boundary problems (point 3d). Concentration dependences of the effective conductivity of the composite will be evaluated. Also, the influence of the embracing polymer molecule on the phonon dynamics and the heat spreading along the nanotube will be calculated.

Heat conductivity properties of nanotubes are actively discussed in this literature. The following is a list of questions and problems under investigation:

- **the general features of the temperature dependence of thermal conductivity - the mechanism of temperature damping at high temperatures and concrete law of increasing at low temperatures.**
- **the maximum thermal conductivity for a solitary carbon tube has not been measured reliably. Current values vary on a wide interval from 200 W/mK to 3000 W/mK from different authors.**
- **the temperature for maximum thermal conductivity for carbon tubes has not been reliably measured and also varies on a wide interval from 150 K to 300 K from different authors.**
- **the question is whether there exist differences in the thermal conductivity of solitary carbon tubes depending on the type (armchair or zigzag), chirality and diameter.**
- **are the differences between thermal conductivity of solitary carbon tubes, flat carbon structures like graphene and graphite (in plane) essential?**

Different authors give different answers to these questions. Another complex problem arises in composites containing nanotubes as a mixture element. Experiments show that a medium like epoxy, having very low thermal conductivity, may change its thermal properties dramatically when a small amount of nanotubes is dissolved in it.

In [1], the single-walled carbon nanotubes (SWNTs) were used to augment the thermal transport properties of industrial epoxy. It was shown that the thermal and mechanical properties of SWNT-epoxy composites were improved significantly. Samples loaded with 1wt% unpurified SWNT material showed a 70% increase in thermal conductivity at 40 K, rising to 125% at room temperature.

The phenomenon of SWNT thermal conductivity was discussed in [2]. The comparison made in this article shows that the measured heat conductivity of single-walled nanotubes differs from that of both 2D graphene and 3D graphite, especially at low temperatures, where 1D quantization of the phonon band structure is observed. For aligned bundles of SWNTs a thermal conductivity of more than 200 W/mK was obtained at room temperature. A linear temperature dependence up to approximately 40 K was observed in [2] for SWNTs. Contradicting results, between quadratic and linear laws at low temperatures, were obtained

for the T-dependence of thermal conductivity of multi-wall NT (MWNT) [3]. The thermal conductivity of a MWNT bundle was measured in the interval $T \in [8\text{-}350]$ K and a maximum of 1200 W/mK was reached at 300 K. In [4] it is shown that the heat processes of nanotubes are similar to that of two-dimensional graphene at high temperatures but is sensitive to the effects of rolling the graphene sheet into a small cylinder at low temperatures.

Measurements for tube bundles show that inter-tube coupling is relatively weak, and the thermal conductivity of nanobundles reflects the on-tube phonon structure [4]. The temperature dependence of electrical conductivity and thermopower were studied theoretically in [5] for single-wall carbon nanotubes using a Green's-function theory. It is shown that armchair and zigzag tubes exhibit quite different temperature dependencies of transport coefficients. The thermal conductivity and thermoelectrical power of a single carbon nanotube were measured in [6] using a micro-device. The observed thermal conductivity is more than 3000 W/Km at room temperature. The temperature dependence of the thermal conductivity exhibits a peak at 320 K. The molecular dynamics method was used in [7] to simulate heat conduction along a single walled carbon nanotube with the Tersoff-B Renner bond order potential [8]. SWNT models with different chiralities (5,5), (8,1), and (10,10) were investigated for the typical length about 125 Angstroms. Thermal conductivity values from 200-300 W/mK were obtained and the dependence on the length of the tube was relatively small. The thermal conductivity for (8,1) chiral tube was measured to be a little smaller than the armchair system. The phonon density of states were measured as the power spectra of velocity fluctuations and compared with the experimental Raman spectra.

Measurements of the thermal conductivity made in [9] show graphite-like behavior for MWNTs but a quite different behavior for SWNTs, specifically a linear temperature dependence at low temperatures, which is consistent with one-dimensional phonons. The room-temperature thermal conductivity of highly aligned SWNT samples is over 200 W/mK, and the thermal conductivity of individual nanotubes is likely to be higher still. Carbon nanotubes have very high thermal conductivity; comparable to diamond crystal and in-plane graphite sheet [10]. The nanotube bundles show very similar properties to graphite crystal in which dramatic differences exist in thermal conductivities along different crystal axis.

We will consider problems relevant to heat propagation in composites containing nanotubes weakly connected with the surrounding medium. Only zigzag and armchair single-walled nanotubes will be taken into account.

1.3.2a. Dynamics of carbon tubes laterally in contact with external medium

The idea of the phonon quantum discrete model (PQDM) is to use a discrete microscopic model for phonon dynamics of relatively small molecular fragments that are approximately of phonon mean free path sizes. The dynamics of such a cluster may be described classically in the Born approach and all the important data may be obtained: eigenfrequences, density of states and phonon amplitude distribution inside the molecular fragment during its lifetime. Connected fragments of a molecular net are in an uninterrupted process of phonon exchange. Due to the weak fragment-surrounding-medium interaction the process may be described by Fermi's "golden rule" that determines a value for the transfer rate. This quantum characteristic is a transport processes consideration and enables us to introduce a microscopic thermal conductivity coefficient that depends on the temperature difference between opposite sides of a fragment that is in contact with the baths.

The model developed here is based on fundamental data characterizing the structure with elastic modulus and elastic coefficients *k*, describing forces acting along the main axes of the bond potential ellipsoid. Thermal expansion coefficient, pressure coefficient, characteristic frequency (or phonon band width) temperature and pressure dependences may be included in the proposed model.

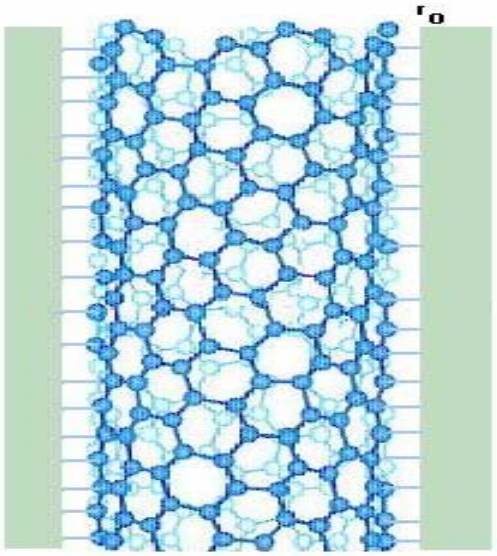

Fig.1.4: Armchair-nanotube inserted into solid matrix. Horizontal blue lines show tube-medium bonds. r_o is tube radius, medium is shown by green.

In this section, we consider a nanotube inserted into the solid matrix – a continuous medium of relatively small heat conductivity. Suppose here that the tube-matrix bonds are weak, that is, the bond is of a physical adsorption type. An armchair nanotube of radius r_o that is weakly connected with the walls of the channel by horizontal bonds is presented in Fig. 1.4.

The vibration dynamics of the armchair tube is represented by three equations for the main types of atomic motion. The adsorption bond will be described by elastic constant κ if the shift is directed along the bond and κ' if it is in the perpendicular direction. We assume that adsorption is weak and $\kappa \approx k/5$, $\kappa' \approx \kappa/10$.

The equation for shifts, ρ_I, directed normal to the tube surface is as following:

$$m\ddot{\rho}_i = -\kappa\rho_i - k'(3\rho_i - \rho_{i1} - \rho_{i2} - \rho_{i3}), \qquad \textbf{(1.4)}$$

where i_1, i_2, i_3 are indexes for the neighbors of atom i, κ and k' are the elastic constants of external adsorption bond and intrinsic respectively. The united atomic number i is defined using its position in the row and column of the initial flat fragment creating the tube.

For tangential atomic shifts we will take into account the atomic space coordinates on the tube surface $x=\varphi R$, where R is the tube radius and φ is the azimuth angle. The armchair case with the absence of chirality is described by the system:

$$m\ddot{x}_i = -0.25k(2x_i - x_{i1} - x_{i2}) - k(x_i - x_{i3}) - \kappa' x_i \qquad \textbf{(1.5)}$$

where coefficient 0.25 characterizes two weak bonds laying on the tube's surface for tangential atomic shift. Another bond directed along the atomic shift is most intensive. The bond of adsorption connection with the external medium is relatively weak for this motion.

For axial atomic shifts we have:

$$m\ddot{z}_i = -k(z_i - z_{i1}) - 0.75k(2z_i - z_{i2} - z_{i3}) - \kappa' z_i \qquad \textbf{(1.6)}$$

where the coefficient 0.75 is connected with two strong bonds and κ' is the elastic constant describing motion perpendicular to the absorption bond κ.

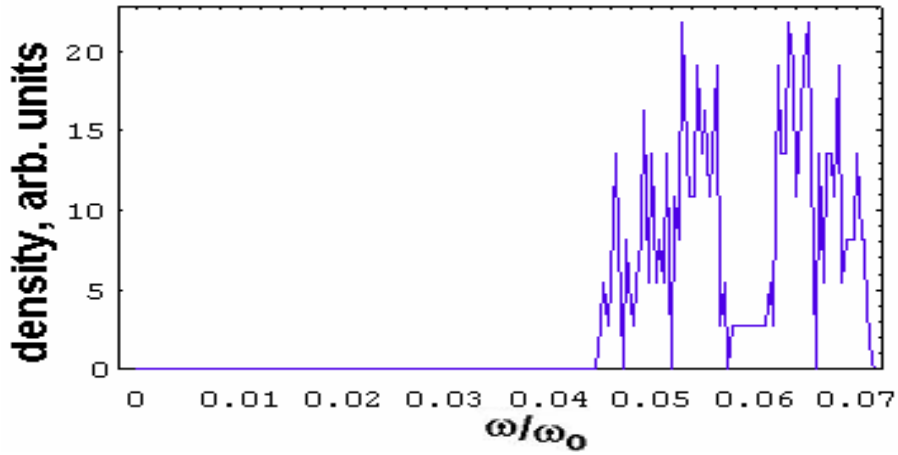

Fig.1.5: Calculated DOS function for radial-branch phonons in laterally adsorbed carbon NT. $\kappa=0.2k$, $\kappa'=\kappa/10$

Calculations show significant differences in phonon band characteristics for the radial branch of vibrations compared to that of a free armchair tube. In Fig.1.5, we see the DOS function for the ρ-branch of phonons found from (1.4) at $\kappa=0.2k$ and $\kappa'=\kappa/10$. The bottom of this band rises at about $0.04\omega_0$ though the top of the band remains almost at the same position. The effect has its explanation in an interesting quality of atomic radial motion. For radial shifts, even relatively weak adsorption bonds have elasticity coefficients bigger than inner bonds. This means that the radial band for a free nanotube transforms to a band of a system of almost non-connected atoms adsorbed onto the intrinsic medium surface.

The eigenstates are grouped in this case near the characteristic frequency of the adsorption bond. Radial vibrations occur as if each carbon atom is almost independent from the neighboring carbon atoms in the nanotube. Due to the band narrowing, the mean density of states becomes several times greater for a nanotube connected by adsorption bonds with a medium surrounding the nanotube surface. Comparison with the data for a free armchair tube shows that only the density of states of radial modes changes essentially with a shift and redistribution.

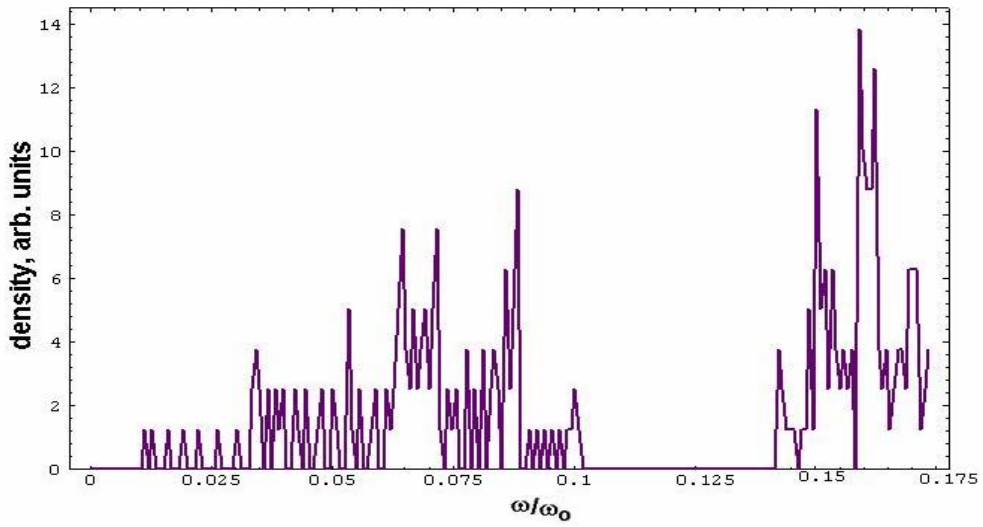

Fig.1.6: Calculated DOS function for tangential branch of phonons in armchair nanotube having 8 hexagons in circumference and laterally adsorbed by external medium. $\kappa=0.2k$, $\kappa'=\kappa/10$.

The DOS function calculated for the φ-branch of molecular vibrations found from (1.5 at $\kappa=0.2k$ and $\kappa'=\kappa/10$ is plotted in Fig.1.6. Minimal differences may be observed in the density of states distribution for the lowest phonon modes that are shifted up by approximately $0.01\omega_0$. The upper part of the band density remains unchanged.

Similar small deviations are observed for longitudinal z-branch vibrations in a laterally adsorbed armchair nanotube. The band bottom also shifts up by about $0.01\omega_0$ at the immovable band top. The calculated DOS function for the z-branch of molecular vibrations, found from (1.6) at parameters given above, is plotted in Fig.1.7. Minimal differences in comparison with free armchair nanotube may be observed as well.

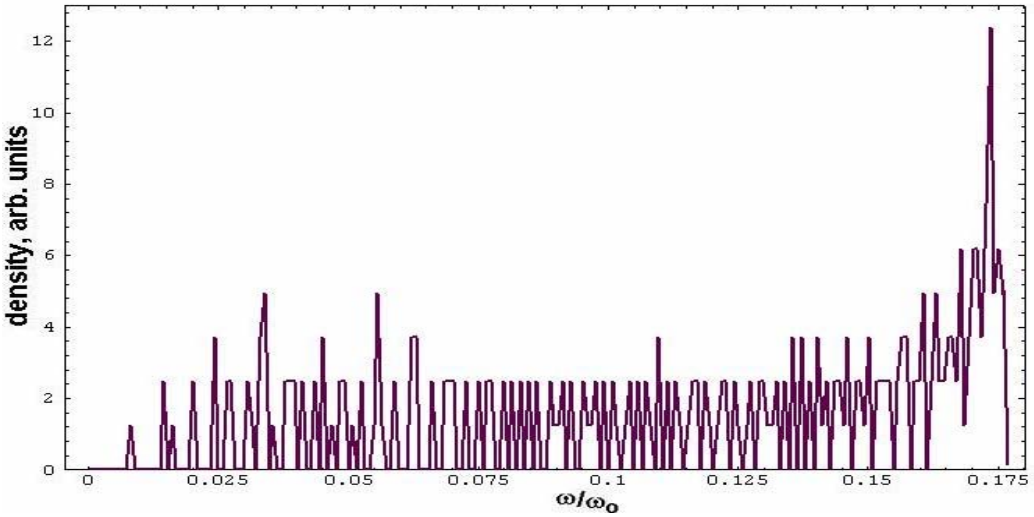

Fig.1.7 Calculated DOS function for axial branch of phonons in armchair nanotube having 8 hexagons in circumference and laterally adsorbed by external medium. $\kappa=0.2k$, $\kappa'=\kappa/10$

It should be marked that considerable changes arise only for radial the branch of vibration due to the direct influence of adsorbtion bonds on breathing modes. As radial vibrations play the key role in heat transport processes through nanotubes one should wait for a significant transformation of the thermal conductivity coefficient $\lambda(T)$.

The densities of phonon states for all three vibrational branches were found to have the same shape for different NT radii (parameter *n*) and different lengths of fragment (parameter *m*). The proportionality coefficient depends on the number of atoms in a fragment.

1.3.2b. Phonon dynamics of carbon tubes embraced by polymer molecule

We have also undertaken the investigation of a two-molecule system: a single-walled nanotube embraced by a polymer molecule like polyacetylene. The calculation of the system was made in the PQDM framework for two molecules: an armchair NT {n,m} (created from a graphene sheet {n,m}) and a polyacetylene chain $(CH)_{2m+1}$, adsorbed by the outer surface parallel to the tube axes. Here the index *n* describes the hexagon number along the tube circumference and index *m* is the same along the tube axes. In the armchair case the length of the tube equals *2ma*, where *a* is the bond length. In zero-approximation, we consider carbon-hydrogen bonds in the polymer as absolutely rigid which leads to an effective mass of the polymer carbon equal to 13. The order of this problem's dynamical matrix becomes equal to *2n(m+1)+2m+2* and for the matrix shown in Fig.1.8 the (*2m+2)* subspace has to be added.

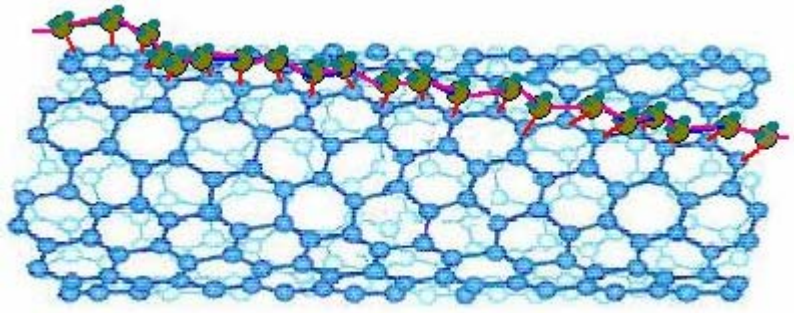

Fig.1.8 A polymer molecule absorbed by armchair nanotube. Absorption bonds are shown by red lines, C-C bonds of the polymer are shown by violet color.

The most important for heat transport radial motion is described by equations for shifts ρ_i (nanotube atoms) and ρ_j (polyacetylene atoms) directed normally to the tube surface

$$m\,\ddot{\rho}_i = -\kappa(\rho_i - \rho_j) - k'(3\rho_i - \rho_{i1} - \rho_{i2} - \rho_{i3})$$
$$m'\ddot{\rho}_j = -\kappa(\rho_j - \rho_i) - k'(2\rho_j - \rho_{j1} - \rho_{j2}) \qquad (1.7)$$

where $m'=13m/12$, i_s and j_s, are indexes for the neighbors of NT-atom *i* and polymer atom *j*, κ and *k'* are elastic constants of external adsorption bond and intrinsic respectively. The united atomic number *i* is defined using its position in the row and column of the initial flat fragment creating the tube. For tangential atomic shifts we will take into account that atomic space coordinates on the tube surface $x=\varphi R$, where *R* is the tube radius and φ is the azimuth angle.

The armchair case with the absence of chirality is described by the system:

$$m\ddot{x}_i = -0.25k(2x_i - x_{i1} - x_{i2}) - k(x_i - x_{i3}) - \kappa'(x_i - x_j)$$
$$m'\ddot{x}_j = -k(2x_j - x_{j1} - x_{j2}) - \kappa'(x_j - x_i)$$

(1.8)

where coefficient 0.25 characterizes two strong bonds for tangential atomic shift. Another pair of bonds directed perpendicular to atomic shift is weak and includes a bond of absorption connection with external medium.
For axial atomic shifts we have:

$$m'\ddot{z}_j = -k(2z_j - z_{j1} - z_{j2}) - \kappa'(z_j - z_i)$$
$$m\ddot{z}_i = -k'(z_i - z_{i1}) - 0.75k(2z_i - z_{i2} - z_{i3}) - \kappa'(z_i - z_j)$$

(1.9)

where the coefficient 0.25 is connected with two weak bonds and κ' is elastic constant describing motion perpendicular to absorption bond κ.

In Fig.1.9, we present the general view of all branches of phonon spectra. In all cases, the spectrum is the superposition of nanotube and polyacetylene spectra deviated by additional bonds.

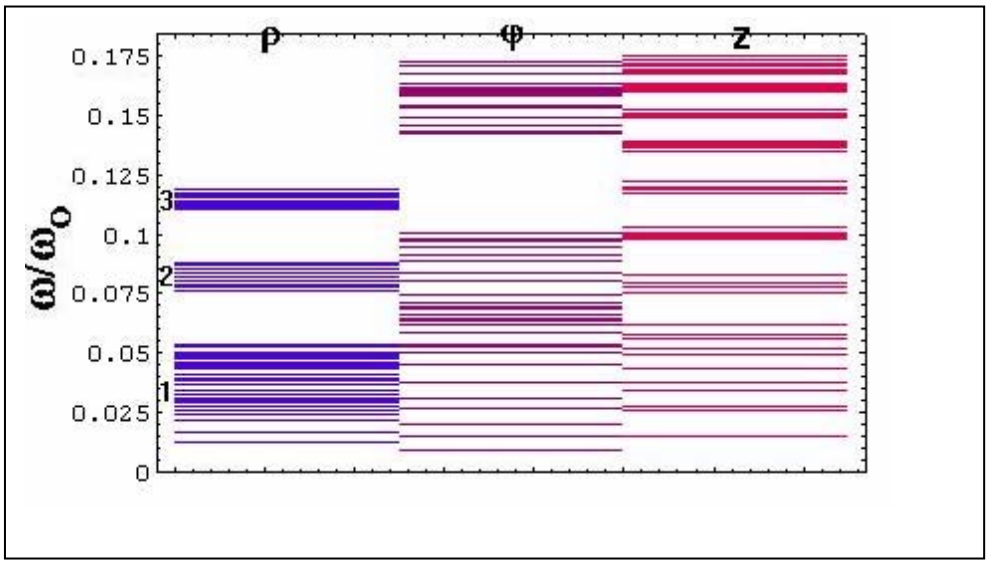

Fig.1.9: Calculated phonon spectra for radial (ρ), tangential *(φ)*, and axial (z) branches of NT-polyacetylene system. 1 shows the nanotube modes, 2 and 3 are two halves of $(CH)_n$ band. Here *κ=k/5, κ'=κ/10.* There are eight hexagons in NT circumference.

1.3.3. Sound propagation in molecular nets

Molecular nets based on carbon and carbon-like systems provide the perfect natural target for 2D and 1D systems that allow us to consider the relation between pure non-thermodynamical sound, called hypersound (or nanosound), and atomic vibrations and the structure of phonon band. Wave phenomena in small flat and closed carbon fragments, films, fulerenes and nanotubes attract close attention now as they are an important part of thermal and transport processes in nanoelectronic devices [1]. Bulk mechanical properties expressed by elastic modules determine sound wave characteristics [2]. The most studied carbon materials, both experimentally and theoretically, are 3D crystals and thin layers [3]. The elastic properties of separated low-dimensional nanosize carbon fragments, single-walled nanotubes etc., give some theoretical troubles connecting the transformation of bulk notions to 2D and 1D ones and with the influence of small sizes [1-4]. Structural and phonon properties of carbon tubulenes were calculated in [5] with the tight binding approach and comparison with flat graphene sheets and bulk graphite was made. The vibrational density of states for 2D hierarchical quasicrystals has been calculated in [6] with the use of the Born approximation [2]. Experimental study of the elastic modulus in a multi-wall nanotube was performed in [7]. Thermal expansion of single-walled carbon nanotube bundles in X-ray diffraction experiments was studied in [8].

The classical theory of sound passing through the interface relies on macroscopic representations in regards to the nature of sound. The phenomenon characteristic sizes (wavelength and the size of averaging) are big compared to the lattice constant. Classical sound is the thermodynamic process uniting both time and space averaging and containing many phonons. The boundary conditions (BC) are introduced into the theory as an external term describing the contact type (strong or weak) between the media [9]. In that case, the BCs are not connected immediately with the microscopic structure of the boundary and have approximate characteristics. Really, for macroscopic rough boundary, the existing exact conditions of the vibration wave passing through the boundary have to be averaged at the distance of the sound wavelength. Now that nanoengineering technology is close to creating hierarchical molecular nets consisting of regularly alternating fragments, the problem of sound propagation in systems with sharp atomic contact boundaries has become the topic of interest.

Carbon nanotubes may be modified by periodic liquid surrounding, periodic intrinsic contain, periodic embracing by polymer, periodic other atoms adsorbed areas, periodic alternating of zigzag and armchair NT, alternating of carbon and BN-tubes, periodic isotope saturated areas and so on. A few pretenders where sound with extremely small wavelengths could exist are presented in Fig.1.10.

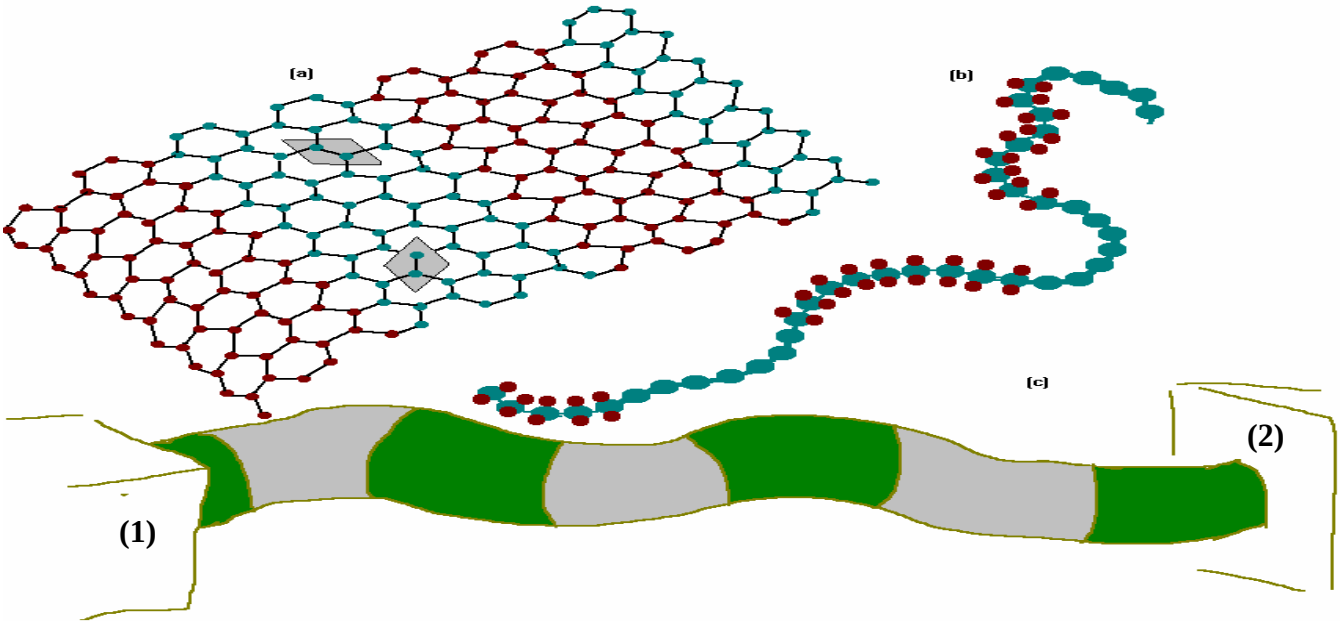

Fig. 1.10: Nanosize periodic structures – pretenders to detect nanosound interfierence.
(a) Cross-linked binary graphene sheet with zigzag type boundaries. Conventional elementary cells are shaded. (b) Carbine-polyethylene periodic linear chain. (c) Periodic fragments of a nanotube differed by elastic constants and (or) atomic mass. 1and 2 are hypersound generator and receiver.

Such tailored structures may play the same role for the hypersound as photonic band gap materials perform for electromagnetic waves [10]. One can suppose the existence of the similarity between acoustic and electromagnetic wave phenomena is due to the band structure and energy transport trough periodic systems [11].

It should be established that the connection between the nanostructure phonon dynamics and sound waves of small wavelengths is not investigated in detail for mesoscopic molecular nets, especially if it reaches the boundary condition problem in complex carbon nets. To obtain the exact BC for sound wave we propose here the integral procedure that starts from dynamical equations for atom vibrations in physically small areas near the boundary. The procedure includes averaging of discrete dynamical equations and transfer to a continuous description. The comparison of notions for native phenomena like phonons, sound and hypersound is used to emphasize the nanosound specifics in molecular nets. The hypersound band structure is calculated in linear approximation for periodically cross-linked nets of different nature. The structure and angular-frequency diagrams describing the sound band structure are obtained.

1.3.3a. Phonons and Hypersound in Low-dimensional Molecular Nets

The molecule vibrational eigenstates are called vibrons. In bulk crystals, the same are defined as "phonons". Low-dimensional molecular nets occupy an intermediate position between small molecules and big macroscopic crystals. Nano-engineering allows the production of complex molecular net systems containing alternating fragments [12, 13]. The external geometry of such cross-linked systems is similar to well-known photonic crystals so sound propagation should possess the same properties including frequency bands and gaps [11]. Electron transport, light absorption and other impact processes in periodically cross-

linked molecular nets may be accompanied by sound pulses of comparatively short wavelength. Characteristic wavelengths of the sound must be about 10^2 nanometers with frequencies of the order of terahertz.

The difference between crystal vibrational eigenstates, phonons and sound is illustrated by the well-known solution for an isolated damped linear oscillator with external driving force

$$\ddot{x} + 2\gamma \dot{x} + \omega_0^2 x = F_0 e^{i\omega t}$$

$$x(t) = x_0 e^{-\gamma t} \cos(\omega'_0 t + \varphi) + \frac{F_0 e^{i\omega t}}{\omega_0^2 - \omega^2 + 2i\gamma\omega} \qquad \textbf{(1.10)}$$

where x_0 is the vibration amplitude, ω_0 and ω'_0 are eigenfrequency and shifted eigenfrequency respectively, F_0 and ω are the external force amplitude and frequency respectively, γ is the damping constant, φ is the initial phase shift.

So, phonon modes have strongly determined frequencies and generally speaking they disappear with time but the sound that is connected with the external source of energy may be of any frequency. Principally, the same takes place for the net of linked oscillators. It is worthwhile to note that the solution for the system of linked oscillators also has a linear combination of partial solutions, like (1.10), and does not contain retardation or any sign of propagating waves.

Several remarkable features are present in periodic molecular nets that differ from bulk materials [9]. First, there exists a precise atomic scale of boundaries between the net fragments with the absence of intermediate layers. The second feature is that phonon branches participate in sound transportation independently in zero-approximation and obey separate boundary conditions. The third one is the strongly non-macroscopic characteristic of elastic waves in small molecular fragments containing a periodic net. This is the reason for the term "nanosound" to differentiate nanometer sound waves from macroscopic sound.

The averaging procedure plays an important role in understanding phonon, sound and heat propagation in low-dimensional atomic nets. Classical dynamical equations in the non-relativistic Born approximation do not contain retardation. This causes the infinite speed of initial vibrational excitation propagation along the net or nanotube.

The first stage of averaging is the presentation of dynamic equations in a finite differences view. More rough-averaging of the phonon mean free path distances is used to describe heat spreading along carbon nets.

	Hypersound	Phonon standing waves	Macro-sound
Frequency spectrum type	**Continuous**	**Discrete**	**Continuous**
Wavelength diapason	**0--10^3 nm**	**No wavelength**	**More than 1 mkm**
Size of state	**No**	**Mean free path(*)**	**No**
Frequency diapason	**(10^{10} - 10^{13}) c^{-1}**	**Phonon bandwidth**	**Less than 10^{10} c^{-1}**
Size of averaging range	**1nm (elementary cell)**	**No averaging**	**1-10 mkm**
Examples of activity processes	**Impact effects, external sources**	**Raman effect**	**External sources**
Transmitting energy	**Energy of atomic vibrations**	**Heat**	**Energy of elastic deformation**
Nature of phenomenon	**Extending waves of atomic vibration**	**Standing waves of vibrations(eigenstates)**	**Extending deformation waves**

***Note*: (*) determined from the phonon lifetime relatively the interaction with other particles and external medium.**

Table 1: Sound, hypersound and phonons

Non-linearity may be presented directly in the dynamic equations as a consequence of averaging and transfer to the rough scale of the phenomena. It should be noted that non-linearity is not connected with the damping of whole phonon states. The energy dissipation and the width of states arise formally when first derivatives are added into the system of classical dynamical equations.

Hypersound waves occur as the result of averaging of classical equations of atomic dynamics. The transfer from equations in finite differences to continuous representation gives second derivatives in both space and temporal. As the averaging acts at very small areas having sizes of an elementary (conventional) cell, the result depends on the concrete symmetry of the elementary cell.

a. Periodic linear chain:

The simple case corresponds to waves in a linear chain with periodically alternating fragments. Let us consider a molecular chain with regular alternation of equal fragments of two types. There exists three vibrational branches that correspond to three degrees of freedom for each atom *s=1,2,3*. Immediately, from atomic dynamical equations, we have

$$\frac{\partial^2 < x >_s}{\partial t^2} - V_s^2 \frac{\partial^2 < x >_s}{\partial z_s^2} = 0 \quad , \quad V_s = a\sqrt{\frac{\chi_s}{m}} \qquad \textbf{(1.11)}$$

where *a* is the interatomic distance, $<x>_s$ is the mean atomic shift in *s*-direction, z_s marks the extended coordinate of *s* degree of freedom. Evaluations by data [5,12] (χ=330 N/m) give for sound velocity along the carbon net *V*=18.3 km/s. This value is close to the velocity of sound in diamond in the (1,1,0) direction.

b. Square lattice:

Waves in hypothetical simple quadratic 2D lattice are described by equation

$$\frac{\partial^2 < x >_s}{\partial t^2} - V_s^2 \frac{\partial^2 < x >_s}{\partial z^2} + (V_s^{'})^2 \frac{\partial^2 < x >_s}{\partial y^2} = 0 \qquad \textbf{(1.12)}$$

Here we are taking into account that the elastic constant for motion transverse to the bond direction differs from that for motion along the band. In 2D structure it is convenient to mark the degrees of freedom through the generalized coordinates. In quadratic lattice *s=z, y, ρ*, the latter describes vibrations perpendicular to the lattice plane. (1.12) is anisotropic for separate branches *s=z, y*. The medium in-plane isotropy manifests in correlation $V_z = V_y^{'}$ and $V_y = V_z^{'}$.

c. Honeycomb lattice zigzag nanostructure, Z-branch:

The dynamics of longitudinal motion along the net or nanotube z-axes may be written for the whole elementary cell having two atoms. For any *i*–atom we have for s=1 degree of freedom,

$$m\ddot{x}_i = -k(2x_i - x_i^l - x_i^r) - 0.25k(2x_i - x_i^u - x_i^d) \qquad \textbf{(1.13)}$$

where the upper indexes mark coordinates of neighboring atoms in y- and z-directions. Two brackets in the right-hand part of (1.13) are transformed into the space coordinate second derivatives after averaging along z-direction and y-direction. In the zigzag case, the averaging distance between neighboring elementary cells equals to *3a/2* along z-axes and $3^{1/2}a$ along y-axes. Inserting these distances into the finite differences derivatives gives the wave equation:

$$\frac{\partial^2 < x >}{\partial t^2} - V_y^2 \frac{\partial^2 < x >}{\partial y^2} - V_z^2 \frac{\partial^2 < x >}{\partial z^2} = 0 \qquad \textbf{(1.14)}$$

where, due to the system anisotropy for z-branch of vibrations as to z- and y-directions, we get different wave velocities along z- and y-directions:

$$V_z = \sqrt{3} V_y / 2 = 1.5 a \sqrt{\tilde{k} / m} \qquad \textbf{(1.15)}$$

d. Honeycomb lattice, zigzag nanostructure, φ-branch:

This branch is connected with the s=2 circumferential degree of freedom in a tube-like net and y-motion in plane structure. For all *i*–atoms, we have the system of connected equations,

$$m\ddot{x}_i = -\tilde{k}(2x_i - x_i^u - x_i^d) - k'(2x_i - x_i^l - x_i^r), \qquad \textbf{(1.16)}$$

that transforms after the transfer to the finite difference view into the wave equation:

$$\frac{\partial^2 < x >}{\partial t^2} - 3V_y^2 \frac{\partial^2 < x >}{\partial y^2} - v_z^2 \frac{\partial^2 < x >}{\partial z^2} = 0 \qquad \textbf{(1.17)}$$

$$v_z = \frac{3a}{2}\sqrt{\frac{k'}{2m}} \qquad \textbf{(1.18)}$$

where ν_z is the φ-wave velocity along z-direction.

1.3.3b. <u>Sound Boundary Conditions</u>

Boundary conditions arise in this approach as a consequence of integrating dynamical equations and averaging in the vicinity of the boundary. In contrast to electromagnetic waves, the vibrational dynamics has the exact meaning immediately for a non-homogeneous range including both sides of the boundary. To take into account the exact bonds between contacting nets of different nature, one has to perform integration or summing before the averaging procedure. In a sense, the sound BCs are a more pure phenomenon than BCs for electromagnetic waves that represent correlation between averaged fields in contacting materials.

a. Periodic linear chain:

The illustration to the BC standards is given by linear chains with periodically alternating fragments. Examples may be carbine fragments alternated by polyethylene or polyacethylene fragments.

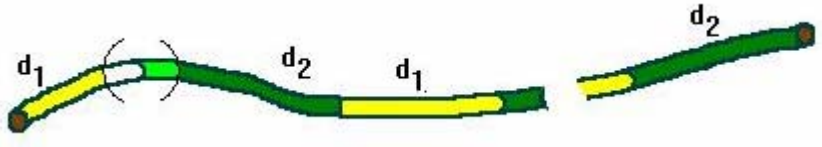

Fig.1.11: One-dimensional periodical chain. Tags d_1 and d_2 mark the length of alternating chain parts. Brackets show the physically small ranges of integration near the boundary.

Consider the range on both sides near the boundary of two molecular chains: from l_0 to the end atom *l* of the left fragment d_1 and from atom *r* to r_0 on the right chain d_2 (Fig.1.11).

$$\begin{cases} m\ddot{x}_l = -q(x_l - x_r) - \chi(x_l - x_{l-1}) \\ m\ddot{x}_r = q(x_l - x_r) - \chi'(x_r - x_{r+1}) \\ m\ddot{x}_{l-1} = -\chi(2x_{l-1} - x_l - x_{l-2}) \\ m\ddot{x}_{r+1} = -\chi'(2x_{r+1} - x_r - x_{r+2}) \\ ---------- \\ m\ddot{x}_{l_0} = -\chi(2x_{l_0} - x_{l_0+1} - x_{l_0-1}) \\ m\ddot{x}_{r_0} = -\chi(2x_{r_0} - x_{r_0-1} - x_{r_0+1}) \end{cases} \quad \textbf{(1.19)}$$

Summation gives:

$$\sum_{i=l}^{l_0} m\ddot{x}_i + \sum_{i=r}^{r_0} m'\ddot{x}_i = -\chi(x_{l_0} - x_{l_0-1}) - \chi'(x_{r_0} - x_{r_0+1}) \quad \textbf{(1.20)}$$

The averaging of the finite difference expressions, on the right side of (1.20), leads to continuous space derivatives. Besides, taking into account the balk wave equations, we change the time derivatives on the left side of (1.20 to the corresponding space derivatives.

$$\sum_{i=l_0}^{l} mV^2 \frac{\partial^2 < x >}{\partial z^2} + \sum_{i=r}^{r_0} m'V'^2 \frac{\partial^2 < x >}{\partial z^2} = -\chi(\frac{\partial < x >}{\partial z})_{l_0} + \chi'(\frac{\partial < x >}{\partial z})_{r_0} \quad \textbf{(1.21)}$$

On the left-hand side, we perform the transfer from summation to integration within the same limits and after the cancellation of end derivatives we get the exact BC,

$$\frac{mV^2}{a}(\frac{\partial < x >}{\partial z})_l = \frac{\bar{m}\bar{V}^2}{\bar{a}}(\frac{\partial < x >}{\partial z})_r \quad \textbf{(1.22)}$$

where *a* and *a* are lattice constants on both sides of the boundary.

(1.23) gives the first of two BCs for near itinerant ranges on both sides of the boundary between chains of two types.

$$\begin{cases} \chi^- a^- \frac{\partial < x >^-}{\partial z} = \chi^+ a^+ \frac{\partial < x >^+}{\partial z} \\ < x >^- = < x >^+ \end{cases} \quad \textbf{(1.23}$$

Another condition arises from the continuity of displacement <*x*> during the wave transition through the boundary.The first BC expression is a kind of material correlation like in the case of electromagnetic waves (EMW) in a medium.

An essential difference arises between sound waves and EMW when we begin considering the free edge of the molecular net. Sound waves are principally absent in the surrounding empty space. This leads to a special case of end boundary equations.

$$\left(\frac{\partial < x >}{\partial z}\right)_{l,r} = 0 \qquad \textbf{(1.24)}$$

Besides, in the EMW case, there is no need for a transfer from discreet equations to continuous ones due to the fact that the classical electromagnetic field is principally a continuous phenomenon.

b. Honeycomb lattice:

BCs in a honeycomb lattice may be obtained in an integral procedure similar to that considered above for a 1D periodical chain. The operation uses a substantially small summation range. The notion of an infinitely small range is a corner-stone of the electromagnetic theory in condensed matter. Its size (1-100nm) determines the size of a conventional point of continuous medium containing electromagnetic field. It is the same for the acoustics of hypersound extending in molecular nets where this has to be introduced on account of the reduced dimensionality and mechanical nature of sound waves. The left side of this interval may be active for hypersound, but in both cases the physically small element must contain many atoms. The summation of dynamical equations inside the small range on both sides near the boundary gives,

$$\sum_{j=d_0}^{u_0}\sum_{i=l_0}^{l} m\ddot{x}_{ij} + \sum_{j=d_0}^{u_0}\sum_{i=r}^{r_0} \bar{m}\ddot{x}_{ij} = -\chi\sum_{j=d_0}^{u_0}(x_{l_0,j} - x_{l_0-1,j}) - \bar{\chi}\sum_{j=d_0}^{u_0}(x_{r_0,j} - x_{r_0+1,j})$$

$$-0.25\chi\sum_{i=l_0}^{l}(x_{i,u_0} - x_{i,u_0+1}) - 0.25\bar{\chi}\sum_{i=r}^{r_0}(x_{i,u_0} - x_{i,u_0+1}) -$$

$$-0.25\chi\sum_{i=l_0}^{l}(x_{i,d_0} - x_{i,d_0-1}) - 0.25\bar{\chi}\sum_{i=r}^{r_0}(x_{i,d_0} - x_{i,d_0-1})$$

(1.25)

The parameters *χ-bar* and *m-bar* belong to the right-hand material. The averaging and transfer to continuous forms of derivatives and sums give:

$$\frac{m}{S_0}\int_{d_0}^{u_0} dy \int_{l_0}^{l} dz \ddot{<x>} + \frac{\bar{m}}{\bar{S}_0}\int_{d_0}^{u_0} dy \int_{r}^{r_0} dz \ddot{<x>} =$$

$$-\chi \frac{a_z}{a_y}\int_{d_0}^{u_0} dy \left(\frac{\partial <x>}{\partial z}\right)_{l_0} + \bar{\chi}\frac{\bar{a}_z}{\bar{a}_y}\int_{d_0}^{u_0} dy \left(\frac{\partial <x>}{\partial z}\right)_{r_0} +$$

$$+0.25\chi \frac{a'_y}{a'_z}\int_{l_0}^{l} dz \left(\frac{\partial <x>}{\partial y}\right)_{u_0} + 0.25\bar{\chi}\frac{\bar{a}'_y}{\bar{a}'_z}\int_{r}^{r_0} dz \left(\frac{\partial <x>}{\partial y}\right)_{u_0} -$$

$$-0.25\chi \frac{a'_y}{a'_z}\int_{l_0}^{l} dz \left(\frac{\partial <x>}{\partial y}\right)_{d_0} - 0.25\bar{\chi}\frac{\bar{a}'_y}{\bar{a}'_z}\int_{r}^{r_0} dz \left(\frac{\partial <x>}{\partial y}\right)_{d_0}$$

(1.26)

Here S_0 marks the half-area of left material elementary cell. Taking into account the wave equation (1.14) connecting time and spatial second derivatives, we have for the left side of (1.26),

$$V_z^2 \frac{m}{S_0}\int_{d_0}^{u_0} dy\left(\left(\frac{\partial <x>}{\partial z}\right)_l - \left(\frac{\partial <x>}{\partial z}\right)_{l_0}\right) + V_y^2 \frac{m}{S_0}\int_{l}^{l_0} dz\left(\left(\frac{\partial <x>}{\partial y}\right)_{u_0} - \left(\frac{\partial <x>}{\partial y}\right)_{d_0}\right)$$

$$\bar{V}_z^2 \frac{\bar{m}}{\bar{S}_0}\int_{d_0}^{u_0} dy\left(\left(\frac{\partial <x>}{\partial z}\right)_{r_0} - \left(\frac{\partial <x>}{\partial z}\right)_{r}\right) + \bar{V}_y^2 \frac{\bar{m}}{\bar{S}_0}\int_{l}^{l_0} dz\left(\left(\frac{\partial <x>}{\partial y}\right)_{u_0} - \left(\frac{\partial <x>}{\partial y}\right)_{d_0}\right)$$

(1.27)

Using explicit expressions for V_z and S_0, we may cancel edge z-derivatives in l_0 and r_0 points of (1.26) and (1.27) after substituting the left part of (1.26) by the expression in (1.27). Due to the fact that the boundary, in this case, is situated perpendicular to the z-axes and taking into account the limits $l_0 \to l$, $r_0 \to r$, $d_0 \to u_0$, we obtain the boundary condition of the type in (1.22):

$$\frac{mV_z^2}{S_0}\left(\frac{\partial <x>}{\partial z}\right)_l = \frac{\bar{m}\bar{V}_z^2}{\bar{S}_0}\left(\frac{\partial <x>}{\partial z}\right)_r \qquad \textbf{(1.28)}$$

If the boundary is situated perpendicular to the y-axes (armchair-type boundary), then the expressions for V_y and S_0 allow cancellation of the edge y-derivatives along the u_0 and d_0 lines in (1.26) and the boundary condition takes the form

$$\frac{mV_y^2}{S_0}\left(\frac{\partial <x>}{\partial y}\right)_u = \frac{\bar{m}\bar{V}_y^2}{\bar{S}_0}\left(\frac{\partial <x>}{\partial y}\right)_d \qquad \textbf{(1.29)}$$

(1.29) represents material correlation between contacting media. The kinematic part of the BC is similar to the zigzag type of boundary for the continuity of the displacement <*x*> when the wave transits through the boundary (see (1.23)). It should be noted that exact

cancellations during the derivation of the BC in the integral procedure performed above is a manifestation of the united nature of both itinerant 2D wave equation and boundary condition procedures. Contrary to electromagnetic waves where BCs are derived from the integral form of Maxwell equations, the analogous integral form of atomic dynamics equations are not very popular. Another significant difference with obtaining EMW boundary conditions consists of the direct presence of elementary cell parameters in material BCs ((1.22), (1.28) and (1.29)) and the atomic bonds elasticity.

1.3.3c. <u>The Hypersound Frequency Bands in Periodic Molecular Nets</u>

The hypersound wave of frequency ω is described by two amplitudes inside each net band.

$$< x >= A\, e^{i\omega t + ik_z z + ik_y y} + B\, e^{i\omega t - ik_z z + ik_y y} \qquad \textbf{(1.30)}$$

There exist two z-projections of the wave vector *k* in a periodic binary molecular net or linear chain depending on the hypersound velocities in the separated materials.

The system of BC equations is described by the matrix presented in Table 2. The intrinsic problem for hypersound eigenstates when external sources are absent and the system is isolated from another sound conductor may be solved analytically as in the case of EMW in layered structures [11, 12].

B_1	A'_1	B'_1	A_2	B_2	A'_2	B'_2	A_3	B_3		A'_{-1}	B'_{-1}	A_N	B_N	A'_N
Z_l	-1	-1	0	0	0	0								
Y_1	η_2	η_2^*	0	0	0	0								
0	σ_2	σ_2^*	-1	-1	0	0								
0	δ_2	δ_2^*	η_1	η_1^*	0	0								
0	0	0	σ_1	σ_1^*	-1	-1								
0	0	0	δ_1	δ_1^*	η_2	η_2^*	0	0						
0	0	0	0	0	σ_2	σ_2^*	-1	-1						
					δ_2	δ_2^*	η_1	η_1^*						
					0	0	σ_1	σ_1^*						
							…	…						
									…	…				
										…				
										η_2	η_2^*	0	0	
										σ_2	σ_2^*	-1	-1	
										δ_2	δ_2^*	η	η^*	
										0	0	σ_1	σ_1^*	Z_r
												δ_1	δ_1^*	Y_r

***Note*: Dotted lines show the minor μ that is matrix element Λ_{11}.**

Table 2: The matrix of boundary condition equations

The generalized dispersion equation is represented in row-matrix-column production

$$(Z_l, -Y_l)\hat{\Lambda}^n \begin{pmatrix} Y_r \\ Z_r \end{pmatrix} = 0,\ \hat{\Lambda} = \begin{pmatrix} \mu & \nu \\ \lambda & \bar{\mu} \end{pmatrix} \qquad \textbf{(1.31)}$$

where *n=N-1*; matrix elements μ, $\bar{\mu}$, ν *and* λ are minors of the dynamical matrix (Tab.2), index *l* corresponds to the left and index *r* corresponds to the right end of the net. The matrix Λ describing the lattice period in turn, is the product of each material matrix $\Lambda=\Lambda_1\Lambda_2$. The matrix elements for the first instance are as follows:

$$\bar{\mu}_1 = \mu_1 = -2i\chi k_z a_z \cos k_z d_1;\quad \nu_1 = -2i(\chi k_z a_z)^2 \sin k_z d_1;\quad \lambda_1 = 2i \sin k_z d_1$$

$$Z_l = \cos k_z d_1;\quad Z_r = -\cos \bar{k}_z d_2;\quad Y_r = -\bar{\chi}\bar{k}_z \bar{a}_z \sin \bar{k}_z d_2 \qquad \textbf{(1.32)}$$

The n-degree for transfer matrix Λ is found by canonical transformation, $\hat{\Theta}$, diagonalizing the matrix Λ.

$$\hat{\Theta} = \frac{1}{D}\begin{pmatrix} x_{22} & -x_{21} \\ -x_{12} & x_{11} \end{pmatrix};\ \hat{\Theta}^{-1} = \begin{pmatrix} x_{11} & x_{21} \\ x_{12} & x_{22} \end{pmatrix};\ D = \det(\hat{\Theta})^{-1};$$

$$\hat{\Lambda}^n = \frac{1}{D}\begin{pmatrix} x_{11}x_{22} f_1^{\,n} - x_{12}x_{21} f_2^{\,n} & x_{11}x_{21}(f_2^{\,n} - f_1^{\,n}) \\ x_{22}x_{12}(f_1^{\,n} - f_2^{\,n}) & x_{11}x_{22} f_2^{\,n} - x_{12}x_{21} f_1^{\,n} \end{pmatrix}, \qquad \textbf{(1.33)}$$

where x_{ij} are elements of matrix Λ eigenvectors: $\hat{X}_1^{+} = (x_{11}, x_{12})$ and $\hat{X}_2^{+} = (x_{12}, x_{22})$

$$x_{11} = x_{21} = \nu;\ x_{12} = f_1 - \mu,\ x_{22} = f_2 - \mu$$

The eigenvalues f_1, f_2 are,

$$f_{1,2} = (\mu + \bar{\mu})/2 \pm \sqrt{((\mu - \bar{\mu})/2)^2 + \lambda\nu} \qquad \textbf{(1.34)}$$

Taking into account (1.32)-(1.34) and (1.31), we obtain a generalized dispersion equation for hypersound in periodic structures, describing sound wave frequencies and type of state: local or band.

$$f_1^{\,n}(Y_r x_{22} - Z_r x_{21})(Z_l x_{11} - Y_l x_{12}) - f_2^{\,n}(Y_r x_{12} - Z_r x_{11})(Z_l x_{21} - Y_l x_{22}) = 0 \qquad \textbf{(1.35)}$$

Extended band states exist in the frequency range with a negative value of discriminant in f_1 or f_2. In this case, there are two parts on the left side of (1.35) which are conjugated and the partial dispersion equation for band states takes the form

$$\nu^2 \sin(n\varphi + \varphi_l + \varphi_r) = 0 \qquad \textbf{(1.36)}$$

where n_φ, φ_l and φ_r are complex phases of three multipliers in the first term of (1.35). A positive discriminant corresponds to frequency gaps. The result of band calculations using (1.35) is presented in Fig.4 for a 16-periodic carbine-polyethylene linear chain $C\text{-}CH_2$.
The frequency is normalized.

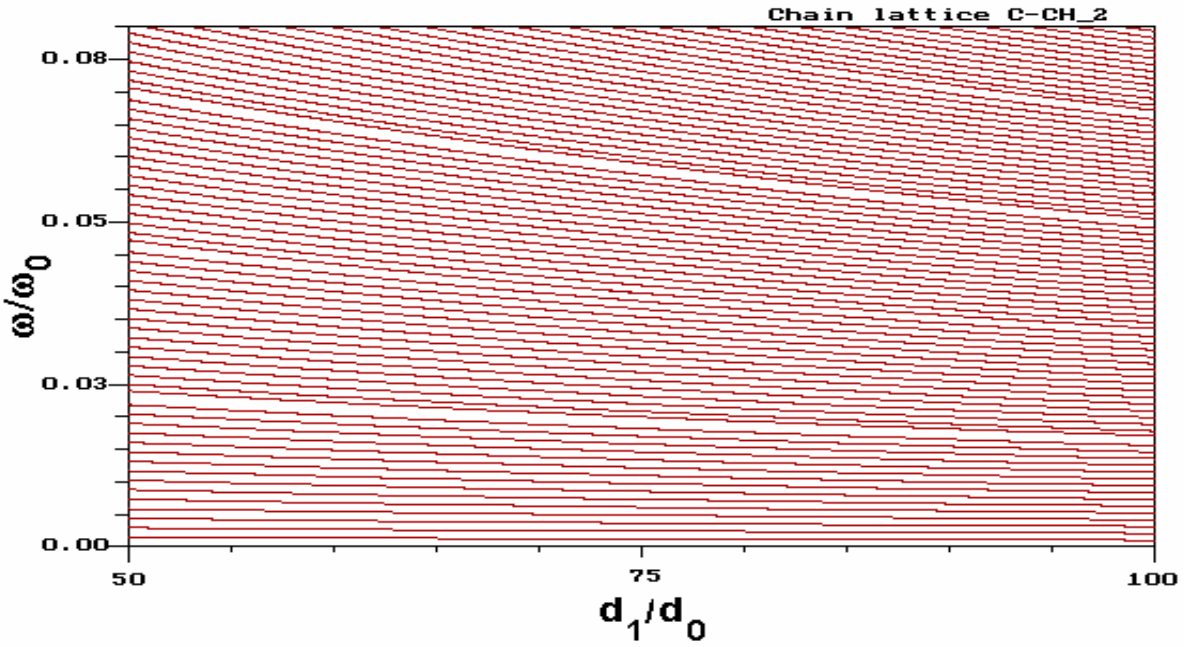

Fig.1.13: One-dimensional 16-periodic elastic chain carbon-CH_2. Frequency–size diagram. d_1/d_0 gives the dimensionless length of the "1-material" fragment, $d_2 = 80d_0$, $d_0 = 0.13$nm is the accepted length unity (for normalizing) and $\omega_0 = 20.48$ THz is the accepted frequency unity.

A value of ω_0 = 20.48 THz was obtained using the elasticity coefficient of the carbon-carbon bond χ =330 N/m: $\omega_0 = (\chi/m)^{1/2}$. The z-wave velocity of sound in pure 2D graphene sheet or tubulene is V_0=16730m/s. The velocity of sound in a hydrogenised graphene sheet is supposedly 7.5% less due to the bigger site mass. Characteristic frequencies are of the order of terahertz for chosen fragment sizes of the order a ten nanometers. If the fragments of chains that are in contact are taken to be near hundreds (10^2) nanometers one may observe the same picture in frequency range but ten times lesser.

Calculations undertaken for different frequency and size scales gave very high similarity in the obtained band pictures at scale transformation $\omega \to c\omega$, $d_1, d_2 \to d_1/c, d_2/c$. With increasing frequency, the bands and gaps became smaller and the slopes of the lines increase. Each frequency band contains the number of states (modes) that coincides with the number of periods in the structure. Only the lower band consists of one less state due to the absence of the trivial (zero-frequency) solution of (1.35). The width of the gap depends on the

difference between relations χ/m for contacting chains and it becomes approximately equal to the band width at $m_1 \approx 6m_2$.

In two-dimensional systems consisting of alternating flat or tube fragments of different kinds, the hexagonal lattices have a new parameter – the incidence angle of the hypersound wave. Standing waves existing in the isolated periodical net depend on the direction of the wave vector. Due to the principal anisotropy of the propagation of z-waves in the hexagonal lattice, the constant velocities in the z- and y-directions are different. Therefore, the wave vector depends on the angle θ of wave propagation.

$$k = \frac{\omega}{\sqrt{V_z^2 \cos^2\theta + V_y^2 \sin^2\theta}} \tag{1.37}$$

The same expression exists for the second material, for which the analogous notations are θ-bar and V-bar. The Snellius-Descartes law $k_y = \bar{k}_y$ gives for transition from medium-1 wave to medium-2 wave.

$$\sin\bar{\theta} = \frac{k_y \bar{V}_z}{\sqrt{\omega^2 + k_y^2(\bar{V}_z^2 - \bar{V}_y^2)}} \tag{1.38}$$

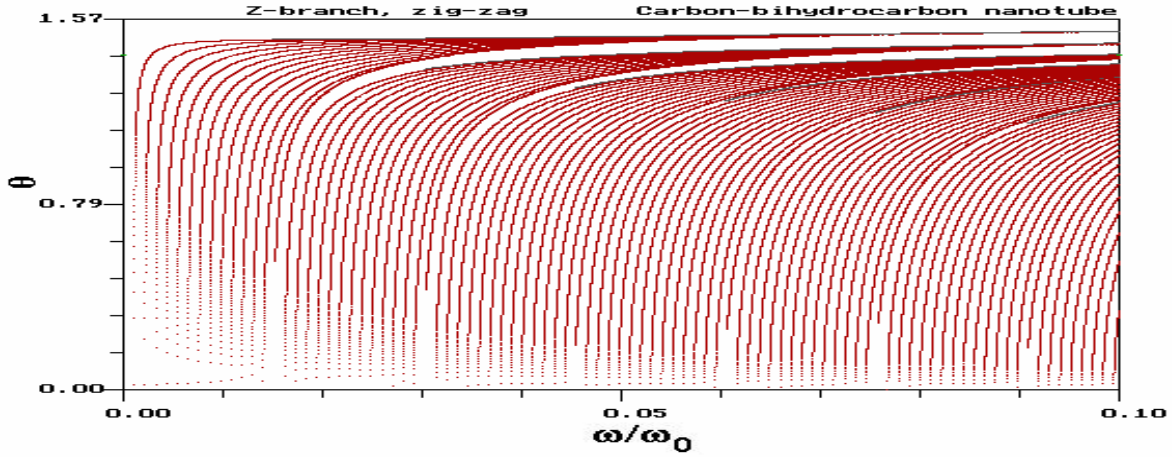

Fig.1.14: Two-dimensional flat 14-period elastic graphene-CH_2 net angular-frequency diagram. Calculated by Eqtns.1.35 and 1.36; $d_1=100d_0$, $d_2=200d_0$, $\omega = (0,0.1)\omega_0$.

The result of calculations by (1.36) for a 2D 14-periodic flat graphene-graphene or closed tube-tube system is presented in Fig.1.14. Accepted unities are ω_0 =20.48 THz and χ =330 N/m for both media. The z-wave velocity of sound in medium-2 was taken to be $1.573V_0$ and $V_z=1.388V_0$ in the acoustically less dense medium. Characteristic frequencies are of the order of teraherzs. The scale transformation $\omega \rightarrow c\omega$, d_1, $d_2 \rightarrow d_1/c$, d_2/c does not change the system band structure in the 2D case either. The number of modes inside each frequency band coincides with the number of periods in the structure.

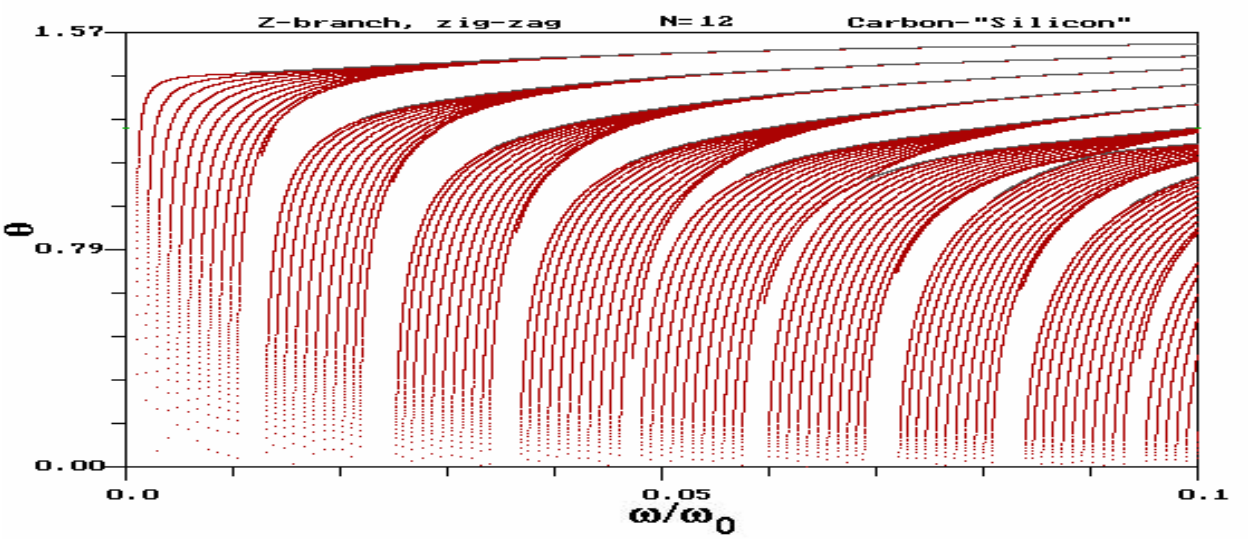

Fig.1.15: Two-dimensional flat 12-period elastic graphene-Si net. Calculated by (26), (27) angular-frequency diagram: $d_1=100d_0$, $d_2=200d_0$, $\omega = (0,0.1)\omega_0$

The width of the gaps depend directly on the difference between χ/m and $\bar{\chi}/\bar{m}$. This property and band structure may be illustrated by an imaginary system – acoustic crystal with sound velocities differed four times: $\bar{V}_z = 1.53V_z$ (Fig.1.15). In Fig.1.14, we see that both bandwidth and gap width are almost regular at small incidence angles. Increasing the frequency leads to bands touching one another and splitting again. A similar phenomenon was observed in 1D photonic crystals [11, 14] for electromagnetic field structure.

The whole intrinsic reflection range occurs in periodic systems due to the difference in wave velocities of different materials. Equation 1.38 illustrates this when $\omega^2 = k_y^2\bar{V}_y^2$ and the formula gives unity. Then the angle of whole reflection in the acoustically less dense first medium is determined by the expression,

$$\sin\theta_{\max} = \frac{V_z}{\sqrt{V_z^2 + \bar{V}_y^2 - V_y^2}} \qquad \textbf{(1.39)}$$

Waves from medium-1 that have the incidence angle bigger than θ_{max}, lose extending character and become damping after the transfer into the acoustically less dense medium-2. Wave vectors become complex $\bar{k}_z \to i\bar{k}_z$ and trigonometric functions in (1.32) become hyperbolic. In the case under study, θ_{max} equals 1.22. The upper part of the frequency-angle diagram was calculated by (1.35 over a wide frequency range. The obtained results show that hypersound bands passing into the whole reflection range degenerate into narrow lines separated by relatively wide gaps.

It is worthwhile to note a difference between sound waves and EM waves in periodic structures that appears in the immediate vicinity of the BC - the boundary microscopic structure parameters in case of hypersound. The other circumstance is the principal presence of anisotropy in the sound wave equation for all vibration branches and all lattice types. In a certain sense, the wave mechanics of hypersound is the theory of spatially dispersed waves in anisotropic media [15]. Another peculiar property of sound waves in

separated structures is the absence of exit waves when all solutions have the characteristics of standing waves.

1.3.3d. Summary

The developed simple model of vibrational dynamics of "bulk" flat and closed carbon and boron-nitride (BN) nanostructures allows immediate transition to the boundary condition problem for sound of small wavelengths in tailored nets. As for the existence of flat carbon or BN systems, we predict that they are geometrically stable and may bridge the inter-electrode space in a strong external electric field. The reason is that negative charging accompanies the process of structure adsorption onto the cathode surface. The affinity electrons captured by the net may prevent its rolling up. The linear approximation used here gives a possibility to consider the vibrations of teraherz frequencies in low-dimensional molecular nets separate from other types of sound. All vibrational branches, z, φ and ρ, obey BC of the same view. The first two branches are mutually complementary for zigzag and armchair nanotubes [13, 16]. The third branch, called the radial mode ρ, is a slow elastic wave compared with other branches. A bandwidth value of phase velocity $V_\rho = a \cdot \Delta_\rho / \pi$, found from radial frequency, is more than twenty times less (0.85km/s) than for the z-branch. The radial branch of vibrations plays a main role in heat transport but does not participate in sound energy transport.

Hypersound accompanies fast processes that occur in molecular nets during the passing of an electric current - the capture of an electron from the external medium, interaction with high energy particles and photons. On the other hand, sound irradiation in such processes may be used as the grounds for particle detecting. The periodical structures considered possess non-trivial frequency band structure for hypersound that allows us to raise the sensitivity of detection. Comparatively slow processes of adsorption also influence the hypersound band structure because adsorption bonds modify host atomic dynamics. The possible adsorption manifestation is the appearance of local states accompanied by a shape transformation of bands. If the adsorption occurs in a mixed gaseous media, each of the gas components matches the individual kind of local hypersound states. This may serve as a tag for sensor devices.

1.3.4. Conclusions

- **The PQDM proposed is able to describe complex interdependent phenomena in open and closed molecular nets: phonon structure, phonon-phonon interaction, statistics, kinetics and irradiation.**

- **Our arguments based on PQDM put in the forefront the eigenstates of weakly bounded captured phonons participating in heat energy transport through the molecular bridges.**

- **Our theoretical approach explains the nature of extremely good thermal conductivity in carbon and carbon-like materials by the existence of the soft vibration branch (low frequency ρ-branch of phonons with high DOS at thermal energies) accompanied by structure hardness (high frequency φ- and z-branches) providing large mean free path for phonons. We conclude that the radial mode contribution to heat transfer**

is dominating in the temperature interval under consideration with the supposition that the phonon-phonon interaction constant G_0 participating in the end atoms constants G_{il} does not depend on the phonon type (ρ, φ or z). Then, ρ-vibrations essentially prevail due to the large density of states in narrow low-frequency ρ-band compared with the DOS for φ- and z-vibrations. So, at actual temperatures ρ-branch of phonons determines heat propagation through the single-walled nanotube.

- **Our results are in accordance with experiments for suspensions by David Cahill et.al (Letters, (Oct. 2003)**

If we add new layers or new walls to single-walled NT, it makes the radial ρ-branch of vibrations harder (see Fig.1.5). This causes the sharp decrease in phonon density of states at the same phonon mean free path. The phonons leave the active thermal zone and heat conductivity decreases. Therefore, atomic monolayers and isolated single-walled nanotubes have to be the best thermal conductors. If we unite SWNT into the tight bundles, the radial mode quenches due to new inter-tube bonds arising. PQDM approach predicts the sufficient worsening of thermal conductivity in SWNT tight bundles comparared with free SWNT. The method of thermal conductivity enhancement in this case is "dissolving" of inter-tubes bonds and turning out the tight bundles into the system of almost free tubes.

Intercalation may be a good way to do this "dissolving" of existing Van der Waals interaction inside bundles. From F.R.Gamble et.al. (Science, 168,568(1970)), the distance between atomic layers increases more than ten times after intercalation by organic molecules. For our case it is enough to increase inter-SWNT distances three or more times and we will obtain a really significant increase in thermal conductivity.

Our proposition is to modify the experimental technique of preparing NT bundles and accompany it by intercalation. Intercalation conserves the large density of states (DOS) of acoustic (radial) phonons in the actual temperature range of frequencies. Our results show that the dominating contribution is from radial (breathing and bending) vibrational degrees of freedoms. Maybe only bending modes are important it is not possible to tell with certainty because all the degrees are present in a common sum. This we will hopefully clarify soon.

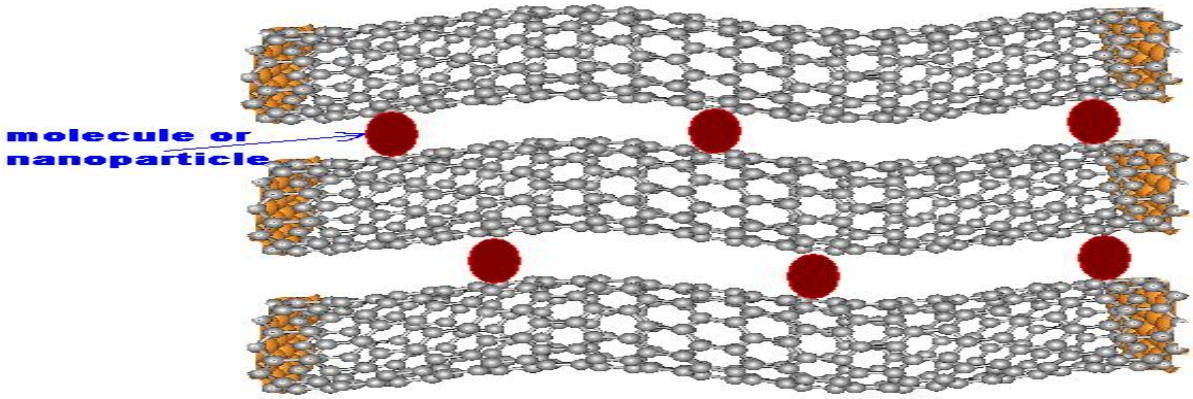

Fig.1.16: A nanotube bundle intercalated by organic molecules or nanoparticles. Intercalation conserves big acoustic (radial) phonon DOS in actual temperature range of frequencies. The distance in 10 or more Angstroms will be enough to switch on radial acoustic phonons for thermal conductivity

We also considered temperature dependencies for thermal coefficient in the entire temperature range and investigate size effects for graphene and tubulene bridges.We studied the transfer of vibration waves through the contact of differing carbon nets and nanometer sound wave interference in periodically alternating 1D or 2D molecular nets of two types. Boundary conditions for hypersound in tailored molecular nets are obtained ab initio by an averaging procedure. The intrinsic problem of vibron egenstates is calculated for carbon net periodic structures. It is shown that hypersound standing wave frequencies are grouped into typical bands divided by frequency gaps. The whole intrinsic reflection effects are considered. In both cases the boundaries between cross-linked fragments lay in the plane perpendicular to z-axes.

1.3.5. References

[1]D.G.Cahill, W.K. Ford, K.E.Goodson; G.D.Mahan, A.Majuindar; H.J.Maris, R.Merlin, S.R.Philpott. *J.Appl.Phys*., 93(2), 793 (2003).

[2]M.Born, K.Xuang Dynamical Theory of Crystal Lattice. London: Oxford Univ.Press, 1954; A.I.Anselm, Vvedenie v teoriju poluprovodnikov., M.: Nauka, 1978

[3]C.E.Bottani. *NATO Science Series*, 24,149 (2001)

[4]T. Ebessen, *Physics Today*, 6 , 26 (1996); A.Rubio, J.L.Corkill,, M.Cohen, *Phys.Rev*. B49, 5081 (1994)

[5]J. Yu, R. K. Kalia, P. Vashishta, *Chem. Phys.* 103, 15, 6697 (1995)

[6]Zh.Liu, Zh.Zhang,Q.Jang, D.Tian. *J.Phys.Condens.Matter*, 4, 6334 (1992)

[7]N.G.Chopra, A.Zettl. *Sol.St.Commun.* 105, 297 (1998); J.Hone, M.Whitney, C.Piscoti, and A.Zettl. *Phys.Rev.* B59, R2514 (2001).

[8]Yu.Maniwa et.al. *Phys.Rev.* B64, 241402 (2002)

[9]L.M.Brekhovskikh, O.A.Godin. Acoustics of layered media. M: Nauka, 1989; J.Taker and V.Rampson. Hypersound in Condensed Matter Physics. M.:Nauka, 1975

[10]UTAM Symposium on Mechanical and Electromagnetic Waves in Structured Media, Edited by R.C. McPhedran, L.C.Botten, and N.A Nicorovici. Kluwer Academic Publishers, Dordrecht, The Netherlands, 2001. Annual APS March Meeting 2003, March 3-7, 2003;Austin Convention Center; Austin, TX,USA.

[11]E.Ya.Glushko, S.L.Legusha, A.A.Zakhidov, *Proc. of the SPIE*. 5065, 97-107 (2002).

[12]E.Ya.Glushko, V.N.Khrisanov, *Low Temp.Phys.* 23, 910 (1997); E.Ya.Glushko, *Low Temp.Phys.* 26, 1130 (2000).

[13]E.Ya.Glushko, V.N.Evteev, M.V.Moiseenko, N.L.Slusarenko, and A.A.Zakhidov. Annual APS March Meeting 2003, March 3-7, 2003;Austin Convention Center; Austin, TX,USA. Quantum model of phonon transport and heat conductivity in carbon nanoclusters and nanotubes, S26-016

[14]E.Ya.Glushko, S.L.Legusha, *Proc. of the SPIE*. 5065, 47-53 (2002)

[15]V.M.Agranovich and V.L.Ginzburg, The Crystal Optics of Media with Spatial Dispersion. M.:Nauka, 1979.

Chapter 2: SYNTHESIS OF NANOSTRUCTURES

2.1 Synthesis of Zeolite Encapsulated Nanotubes

Considerable progress has been made in the synthesis of multi-walled and single-walled carbon nanotubes (SWCNT) by catalytic chemical vapor deposition (CVD) techniques. However, a typical preparation may result in a complex mixture of nanotube sizes and types. Between 1 and 3 nm in diameter there are 403 possible structures alone. To prepare one size and a single type of carbon nanotube remains a challenge. There are only 3 possible structures ((5,0), (4,2), (3,3)) for the 0.40 ±0.01 SWCNT, compared with the 403. To prepare such small diameter SWCNTs, one might employ a matrix to control the size during synthesis. It was reported that mono-sized (0.4nm) single-wall carbon nanotubes (SWCNTs) can be formed in the channels of large single crystal $AlPO_4$-5 by pyrolysis of the organic template, tripropylamine (TPA), without any other external carbon source [Tang et al, Appl. Phys. Lett., 73 (1998), 2287].

We have now prepared single-wall carbon nanotubes in the channels of UTD-1, UTD-18 and UTD-12 (shown below) which are structurally related zeolites having one-dimensional channels that run in parallel. All of these zeolites are made using various cobalticinium ions. The thermal decomposition of these organometallic templates results in cobalt catalyst as well as a carbon source for making carbon nanotubes. The dimensions of the pores dictate the size of the resulting nanotubes such that we can systematically vary the CNT diameter by using the 10, 12 or 14 MR structures.

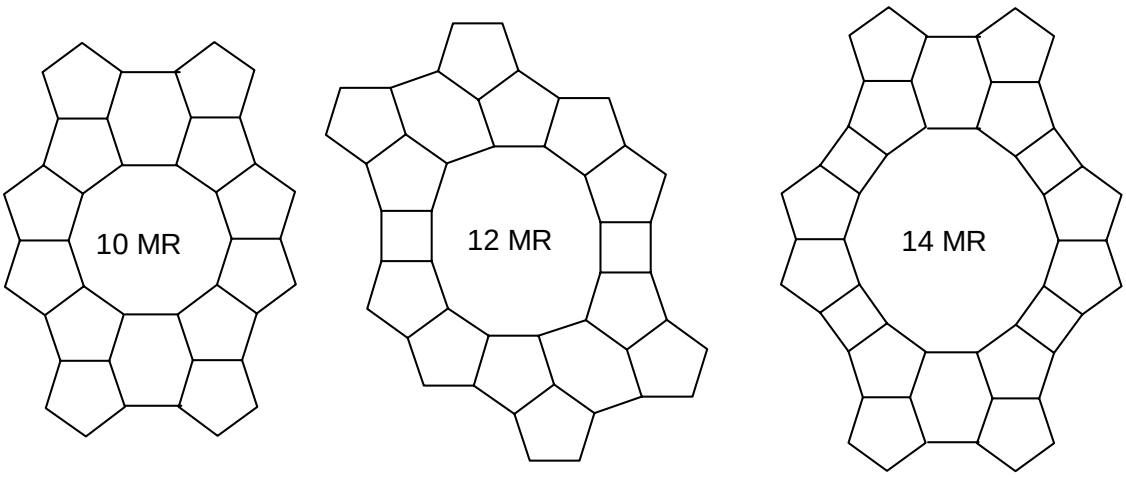

Fig. 2.1: 10, 12 or 14 MR structures

Fig. 2.2 shows the typical Raman spectra of the as synthesized UTD-1 (bottom - black) and the SWCNTs recovered after HF treatment of the UTD-1 crystals (top - purple). The Raman spectrum of the as synthesized UTD-1 shows characteristic Raman-active modes of CH_3 symmetric stretching (2912 cm^{-1}), the CH_3 anti-symmetric deformation (1430cm^{-1}), C=C stretching (1650 cm^{-1}) and the symmetric metal-ring stretching vibration (365cm^{-1}) of $Cp^*_2Co^+$ molecules. When the sample is pyrolyzed at 800°C for 5 hrs and then HF treated, new Raman peaks appeared at 1600 cm^{-1} and 432 cm^{-1} (shown in Figure 2 top purple). The

strongest low-frequency Raman mode at 432 cm^{-1} is expected to be the radial breathing A_{1g} mode. The radial breathing A_{1g} mode is not sensitive to nanotube structure but to the nanotube radius. The observed frequency of 432 cm^{-1} indicates the radius of the carbon nanotube is 0.54 nm.

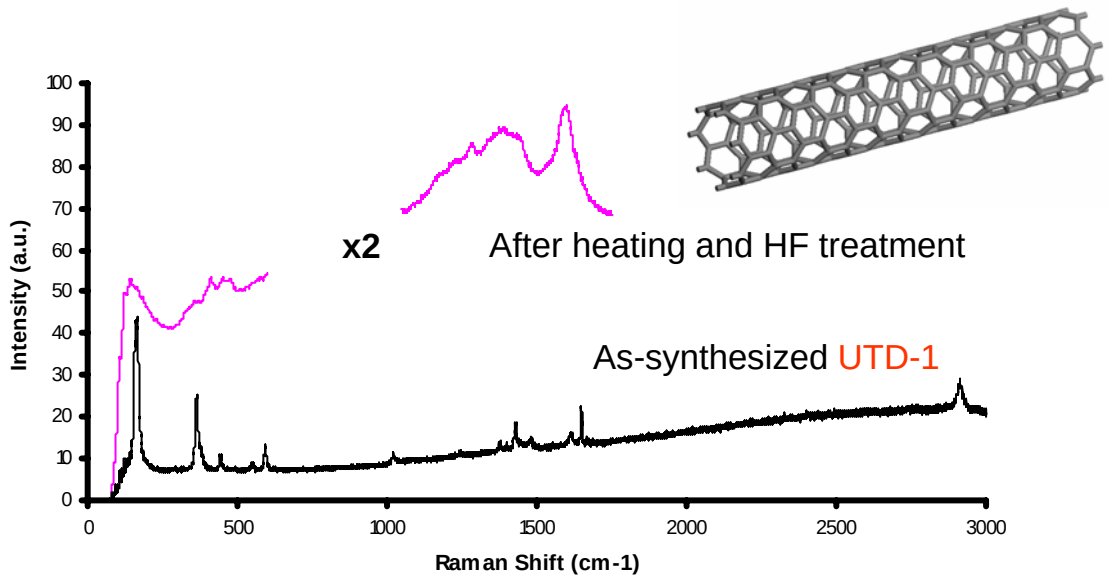

Fig.2.2: typical Raman spectra of as synthesized UTD-1 and SWCNTs recovered after HF treatment of the UTD-1 crystals

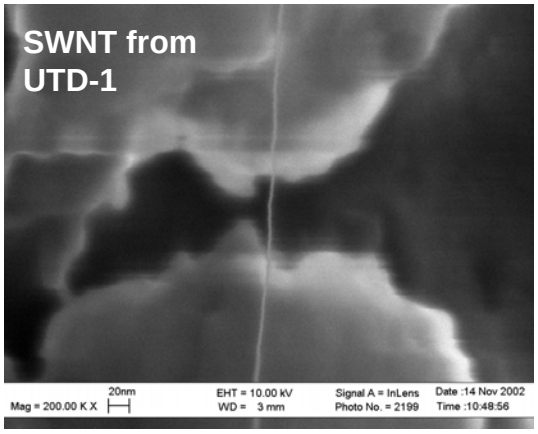

Fig.2.3: SEM image of a SWCNT obtained after HF treatment of calcined UTD-1

Fig. 2.3 shows the SEM image of a SWCNT obtained after HF treatment of calcined UTD-1. It shows the size of the carbon nanotube is less than 1 nm and at least 500nm long, consistent with the Raman spectrum. The SEM results also indicate that the SWCNTs prepared in the UTD-1 channels are stable without the silica matrix. A high resolution TEM image of the SWCNTs recovered from UTD-1 is shown in Fig.2.5. From this image an estimate of the nanotube diameter is ~0.5nm. The exact type of carbon nanotube prepared in

UTD-1 is uncertain but possible nanotubes might be the (4,4)-0.54nm, (7,0)-5.5nm and the (5,3)-0.55nm.

Zeolite UTD-18 is structurally related to SSZ-31 (polymoph C) which is comprised of elliptical 12 MR pores with dimensions of 8.6 × 5.7 Å. Fig. 2.4 shows the typical Raman spectra of the as synthesized UTD-18 (bottom - black) and the SWCNTs recovered after HF treatment of UTD-18 (top - purple). The Raman spectrum of the as synthesized UTD-18 shows characteristic Raman-active modes of C=C stretching (1650 cm^{-1}), the CH_3 anti-symmetric deformation (1480 cm^{-1}), CH_2 wag (1235 cm^{-1}) and twist (1211 cm^{-1}), C-H in phase bending (1052 cm^{-1}) and out-of-plane bending (849 cm^{-1}) and the symmetric metal-ring stretching vibration (332 cm^{-1}) of the $(EtCp)_2Co^+$ template molecules. When the zeolite is heated at 800°C for 5 hrs followed by HF treatment, new Raman peaks appear at 1606 cm^{-1} and 445 cm^{-1} (shown in Fig.2.7 top purple). The strongest low-frequency Raman mode at 445 cm^{-1} is expected to be the radial breathing A_{1g} mode. The observed frequency of 445 cm^{-1} indicates the radius of the carbon nanotube is ~0.52 nm. The higher frequency radial breathing mode and smaller SWCNT diameter compared with UTD-1 is consistent with the smaller pore size of UTD-18. Fig.2.6 shows the SWNTs recovered from UTD-18.

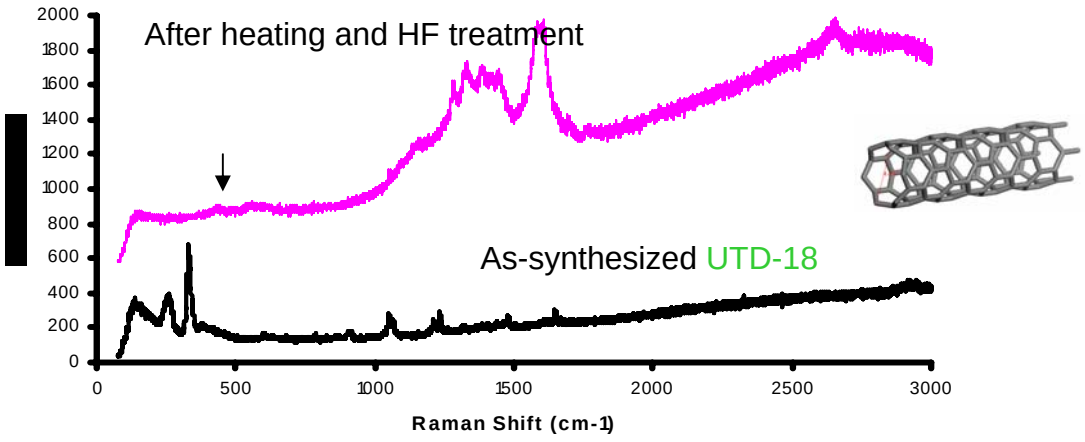

Fig.2.4: Typical Raman spectra of the as synthesized UTD-18 (black) and the SWCNTs recovered after HF treatment of UTD-18 (purple)

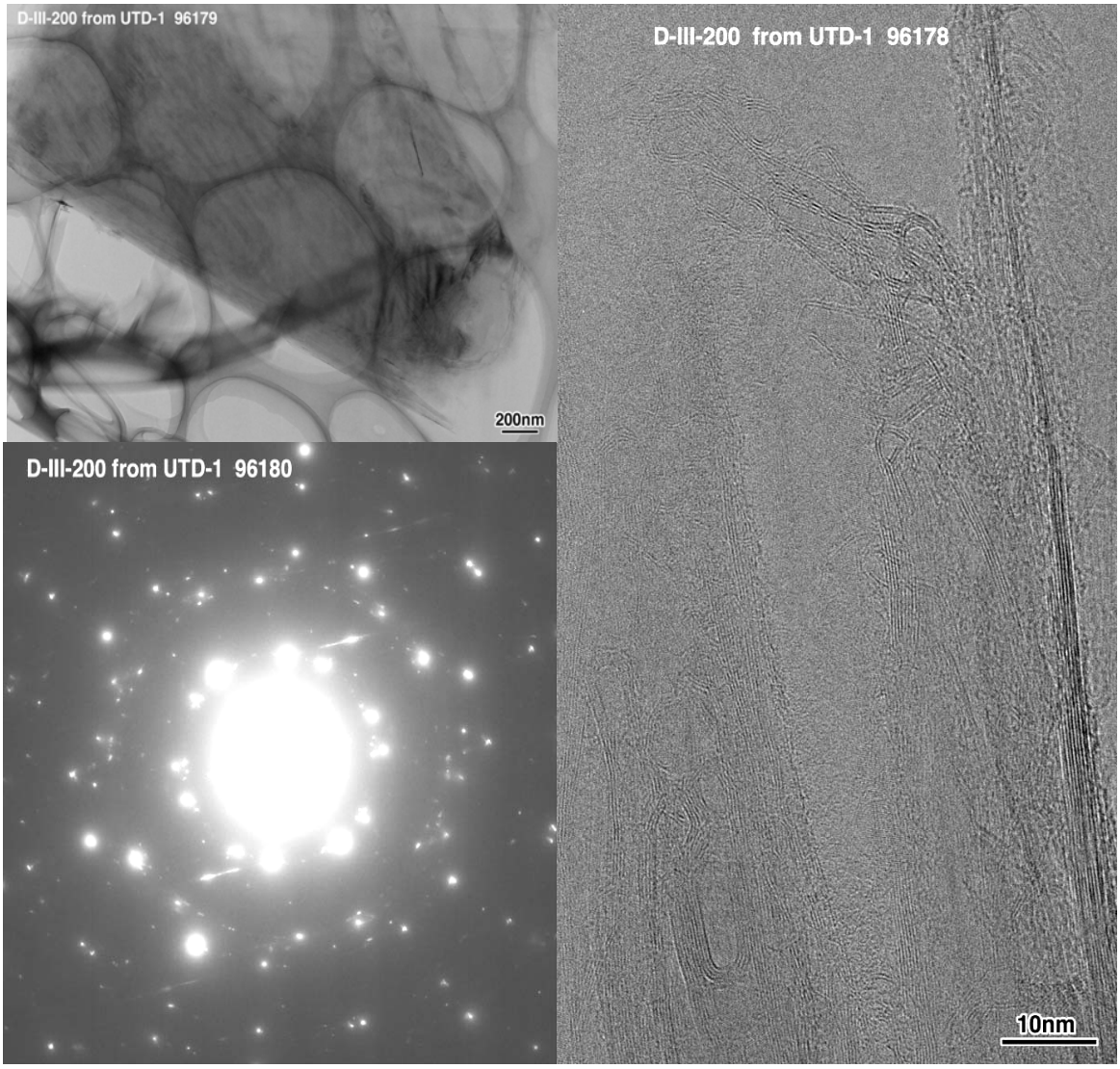

Fig.2.5: SWNT recovered from UTD-1

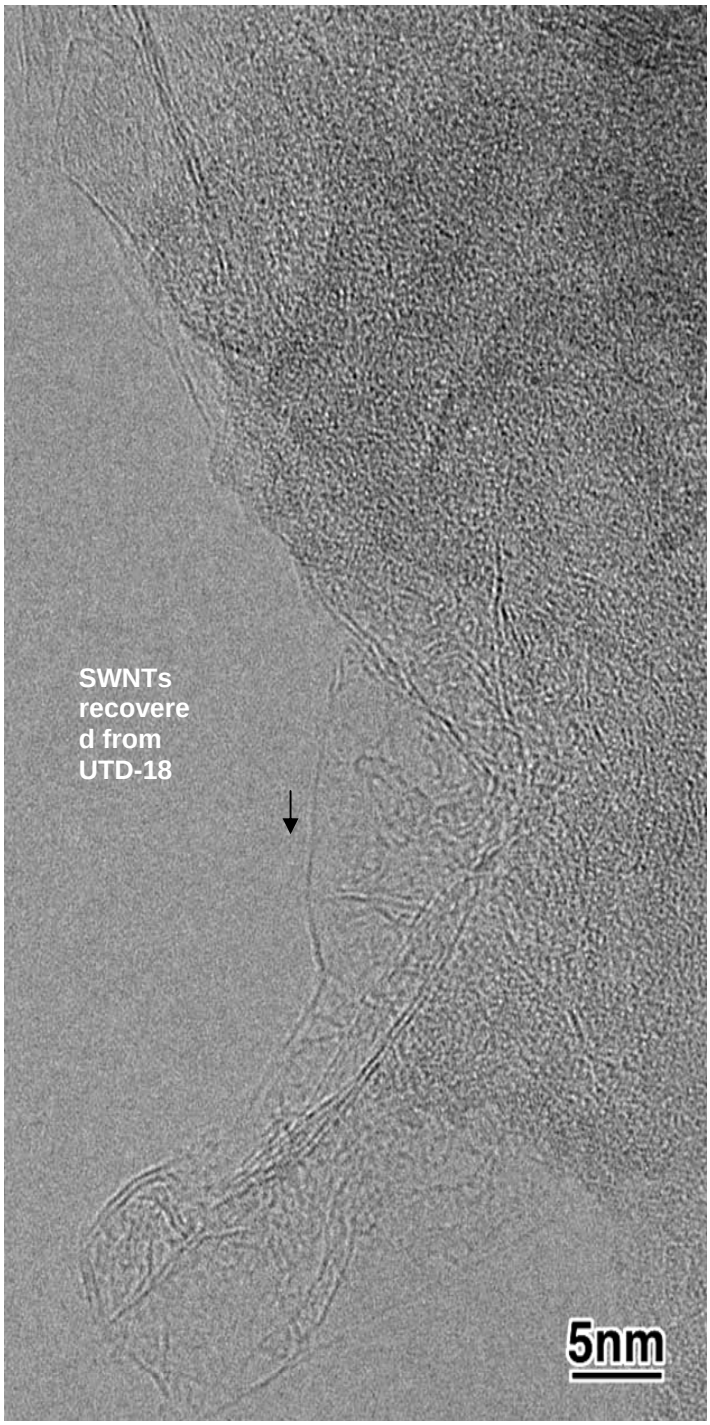

Fig.2.6: SWNTs recovered from UTD-18

Zeolite UTD-12, closely related to ZSM-48, possesses non-interpenetrating linear channels defined by 10 membered rings having dimensions of 5.3 × 5.6 Å. Fig. 2.7 shows the typical Raman spectra of as synthesized UTD-12 (bottom - black) and the SWCNTs recovered from UTD-12 after HF treatment (top - purple). The Raman spectrum of the as synthesized UTD-12 shows the characteristic Raman-active modes of C-C stretching (1421cm^{-1}), the C-C ring breath (1113cm^{-1}), C-H in-phase bending (1069cm^{-1}) and C-H out-

of-plane bending (849cm^{-1}), the symmetric metal-ring vibration (318cm^{-1}) and the ring deformation (385cm^{-1}) of the Cp_2Co^+ template molecules [30]. When the sample is pyrolyzed at 800°C for 5 hrs followed by HF treatment, new Raman peaks appeared at 1597cm^{-1} and 559cm^{-1} (shown in Fig.2.7 top purple). The strongest low-frequency Raman mode at 559cm^{-1} is expected to be the radial breathing A_{1g} mode. The observed frequency of 559cm^{-1} indicates the radius of the carbon nanotube is 0.41 nm. This could very well be the smallest carbon nanotube ever made.

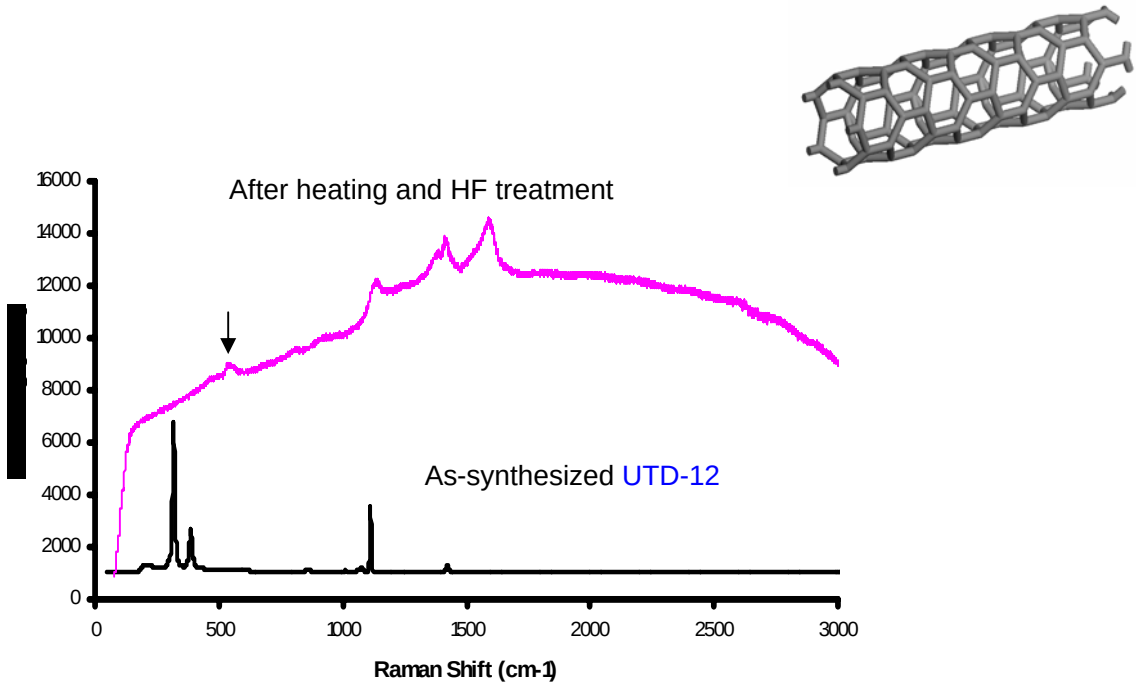

Fig.2.7 typical Raman spectra of as synthesized UTD-12 (black) and the SWCNTs recovered from UTD-12 after HF treatment (purple)

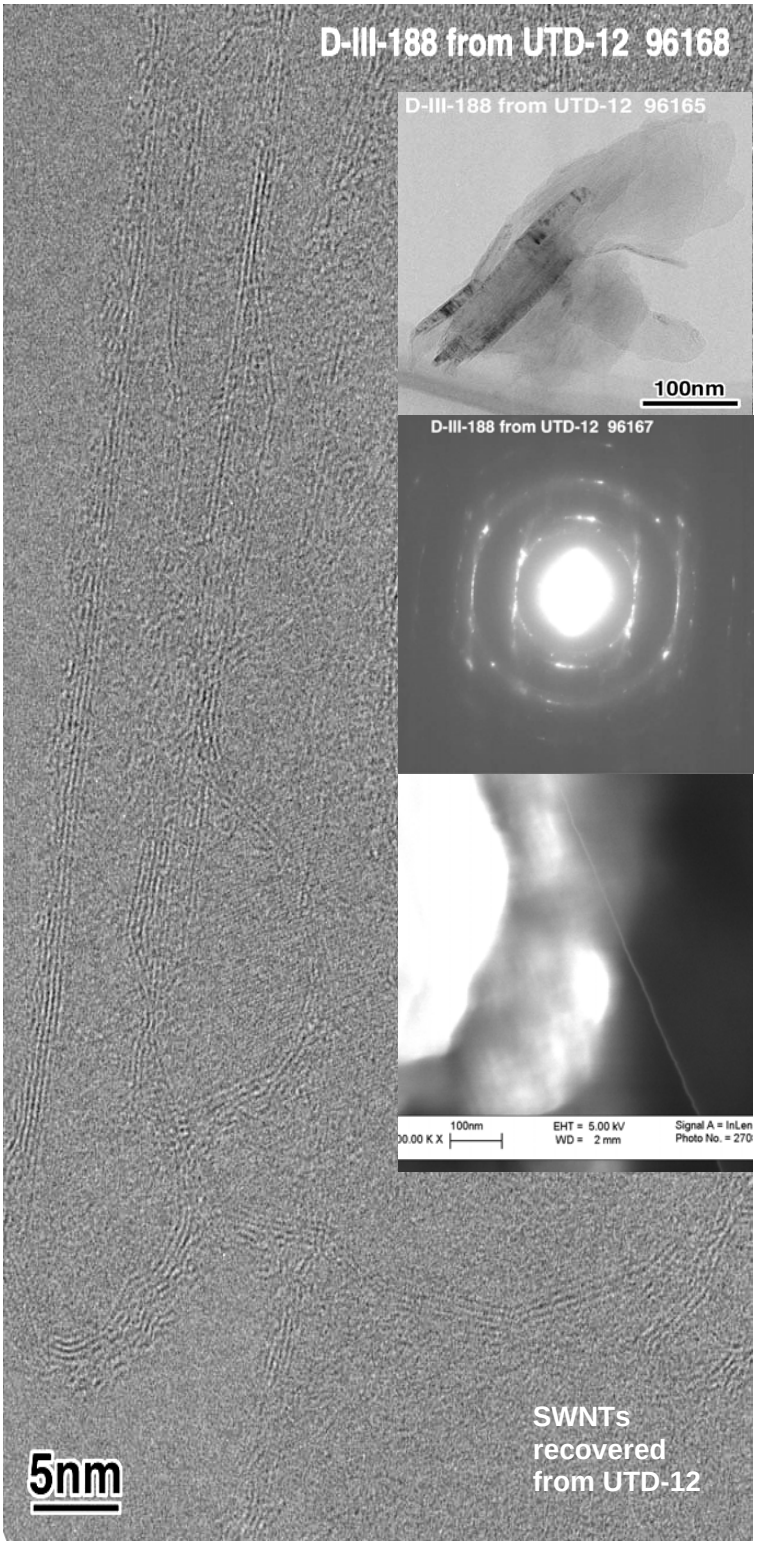

Fig.2.8: SWNTs recovered from UTD-12

CNTs this small may be metallic and superconducting. Preliminary magnetic susceptibility χT-dependence measurement of the UTD-12 (with SWCNTs) after HF treatment is shown below. Some of the unusual magnetic properties of the SWCNTs obtained

in the UTD-12 channels may be due to residual Co. However, there may be some evidence of superconductivity.

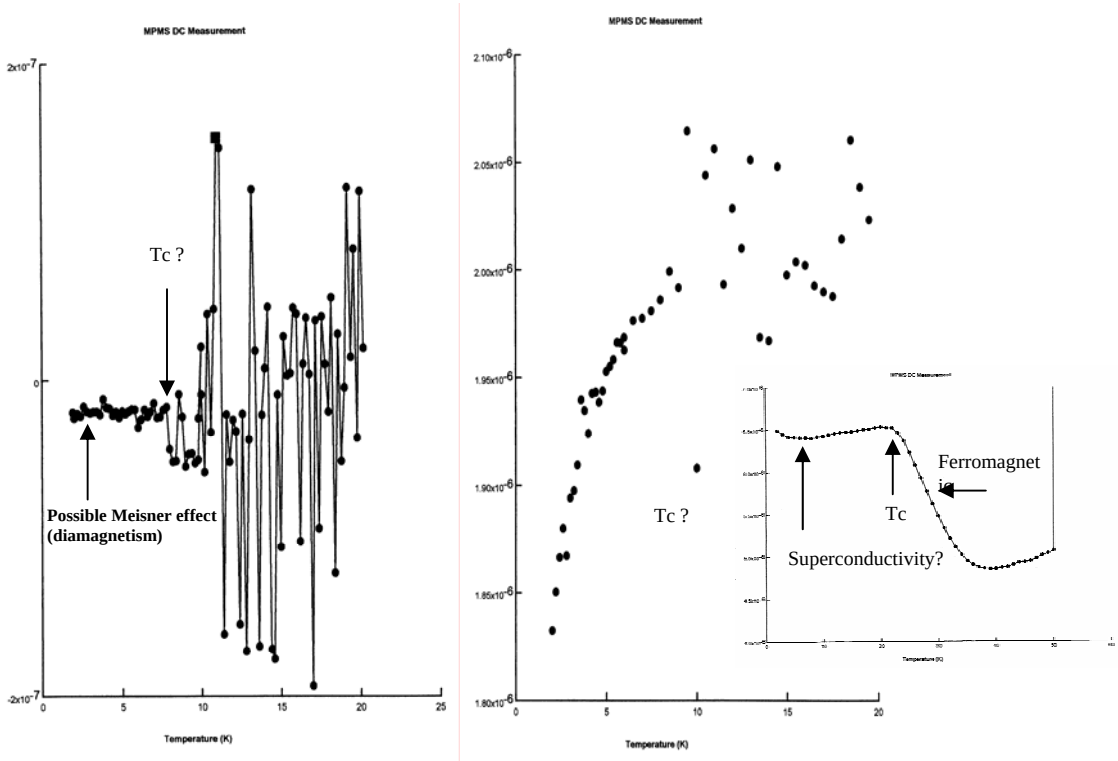

Fig.2.9

Publications

Deng, S.; Dalton, A.; Terasaki, O.; Balkus, Jr., K.J., "Carbon Nanotubes Synthesized in Zeolites UTD-1, UTD-18 and UTD-12" ***Proc. 14th Int. Zeolite Conf*****. 2004, 903-910**

Deng, S.; Dalton, A.; Terasaki, O.; Balkus, Jr., K.J., "Carbon Nanotubes Synthesized in Zeolites UTD-1, UTD-18 and UTD-12" ***Stud. Surf. Sci. Catal*****. 2004,** ***154.***

An additional paper incorporating magnetic susceptibility data and synthesis variations is possible.

Presentations

14th International . Zeolite Conference

2003 SPRING Conference

2.2 Synthesis of Conjugated Polymer-CNT Complexes

Poor heat dissipation in organic and polymeric electronic devices is a key problem that limits their performance at high current loading. It is known that addition of quite small amounts of nanotubes can improve the performance of organic devices, apparently due to improved heat dissipation via the nanotube component.

Various CNT-CNT interactions that can compromise the spectacular thermal conductivity properties of individual CNTs are shown in Fig. 2.10(a). The focus of this effort was to create new types of donor (acceptor) polymers, which could provide better unbundling of CNTs (Fig. 2.10(b)) to enhance dissipation of the heat generated in polymeric devices such as OLEDs or solar cells.

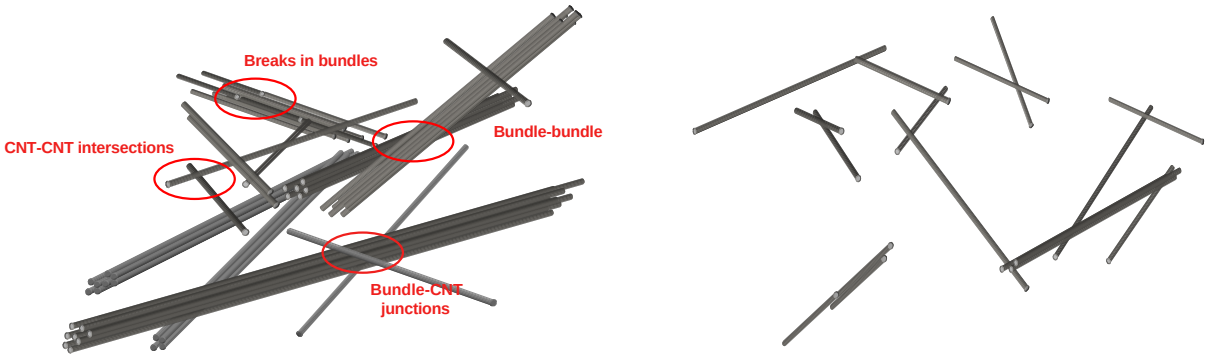

(a) **(b)**

Fig. 2.10: Representative CNT-CNT interactions that compromise high thermal conductivity of CNTs (a), and reduction of these effects due to unbundling (b).

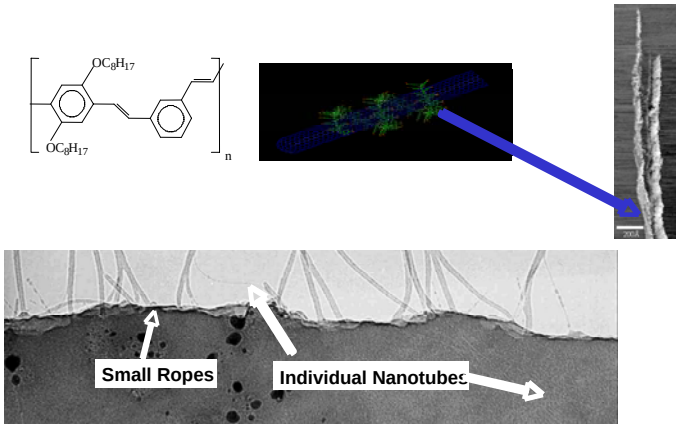

Fig.2.11: Bundle exfoliation using conjugated polymers

Several types of debundling polymer systems are known. Fig. 2.11 shows that CNTs can be effectively debundled using a phenylene-vinylene (PPV) conjugated polymer. Conjugated polymers (CP) afford the additional opportunity to introduce charge transfer to enhance CP-CNT interactions that can be "tuned" by polymer design.

Several PPV-derivatives were synthesized to determine their abilities to debundle CNTs with the goal toward enhancing thermal conductivities in CP-CNT composites. The well-studied MEH–PPV was prepared according to literature procedures and used as a reference material for the composites. The molecular weights of the samples used were 292,000 (Mn) with a polydispersity of 1.04 and 281,000 (Mn) with a polydispersity of <1.2.

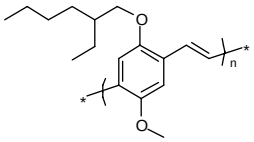

BEH-PPV

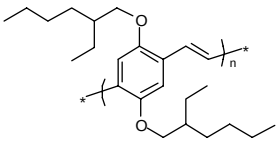

BEHM-PPV

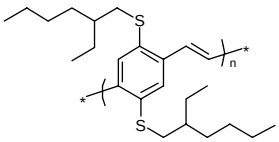

MEH-PPV

Bis-ethylhexyloxy-PPV precursor

Synthesis

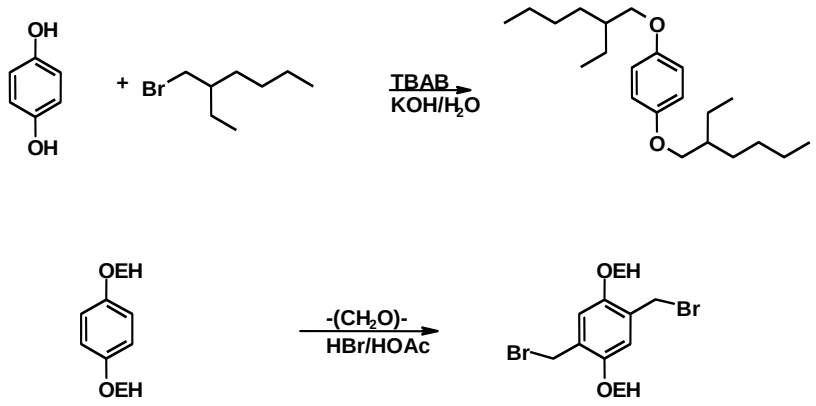

BEH-PPV precursor monomer synthesis

Bis-ethylhexylmercapto-PPV precursor

Synthesis

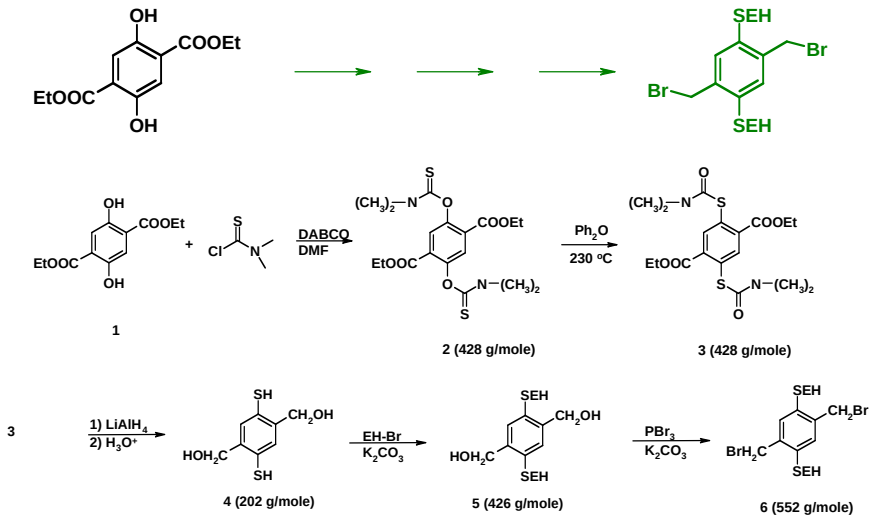

BEHM-PPV precursor monomer synthesis

Fig. 2.11

The composites were prepared using the following protocol. SWNTs were added to a solution of MEHPPV (or other CP) in THF or $CHCl_3$. The resulting suspension was stirred overnight and allowed to settle. The supernatant was then decanted and the composite film was obtained by rotary-evaporation of the solvent.

Fig. 2.12: The dramatic effect of adding SWNT to MEH-PPV (or BEH-PPV) can be seen from the accompanying figure. The pure polymer produces clear red films while the composite films exhibit a blue-green metallic sheen.

Fig. 2.13: Shows the solutions of BEHM-PPV mixed with SWNT in different concentrations. SEM images of several composite film compositions are shown below

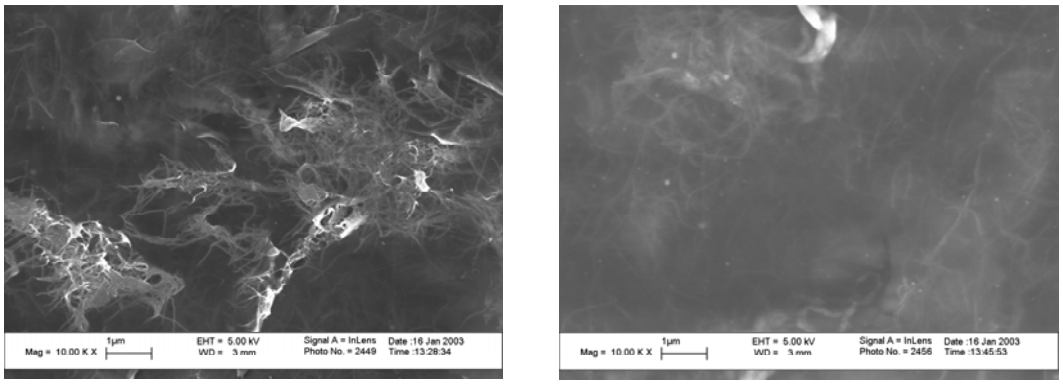

Fig. 2.14: Dispersion of 1% SWNT in MEH-PPV. Note non-uniformity

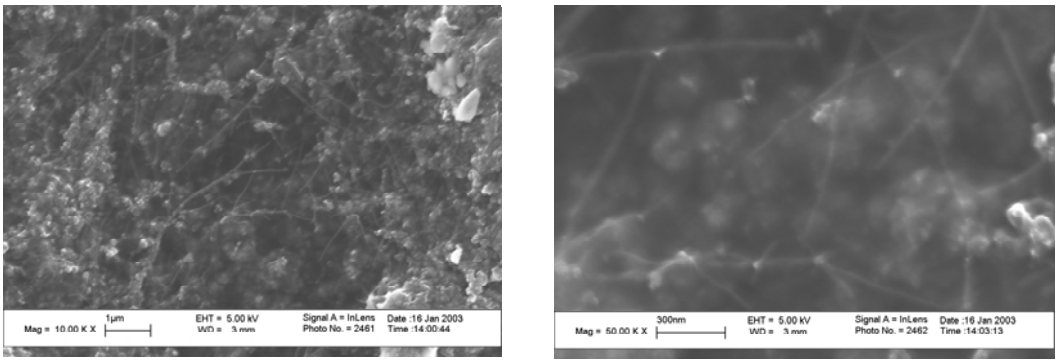

Fig. 2.15: Dispersion of 5% SWNT in MEH-PPV. Note non-uniformity

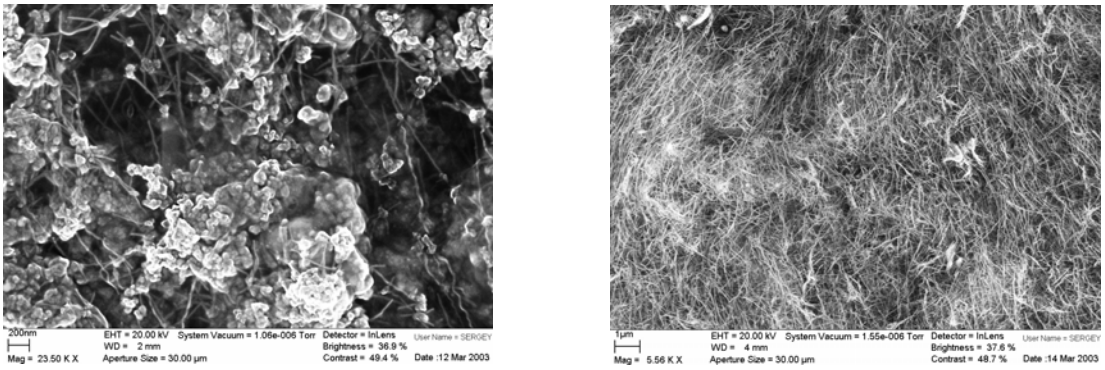

MEH-PPV **BEHM-PPV**

Fig.2.16: Enhanced dispersion of 2% SWNT in BEHM-PPV compared to 5% MEH-PPV

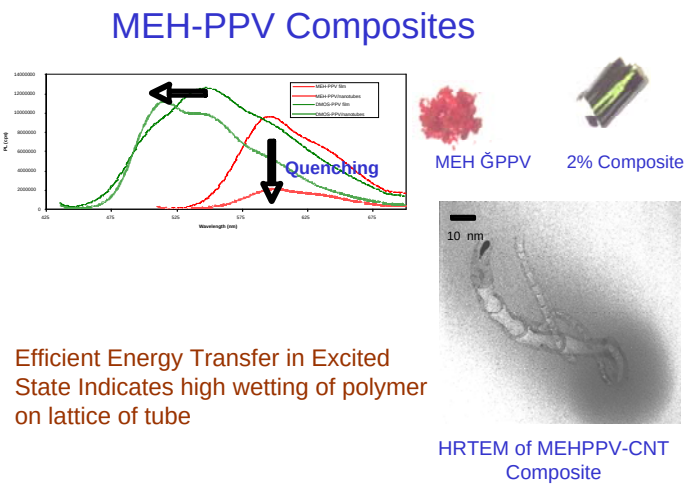

Figure 2.17: Even with modest dispersion of SWNT with MEH-PPV, the nanotubes are strongly wetted by the polymer composites as evidenced by the efficient energy transfer (quenching) in the excited state.

The hydrophobic SWNT mixed with MEH-PPV in chloroform solution gave rise to the agglomeration shown above in Fig. 2.16 (left). Better distribution of SWNT was obtained for BEHM-PPV polymer (Fig. 2.16, right). Strong anisotropy of λ(T) (Fig. 2.18) in MEH-PPV films mixed with SWNT indicates the in-plane distribution of nanotubes along the film.

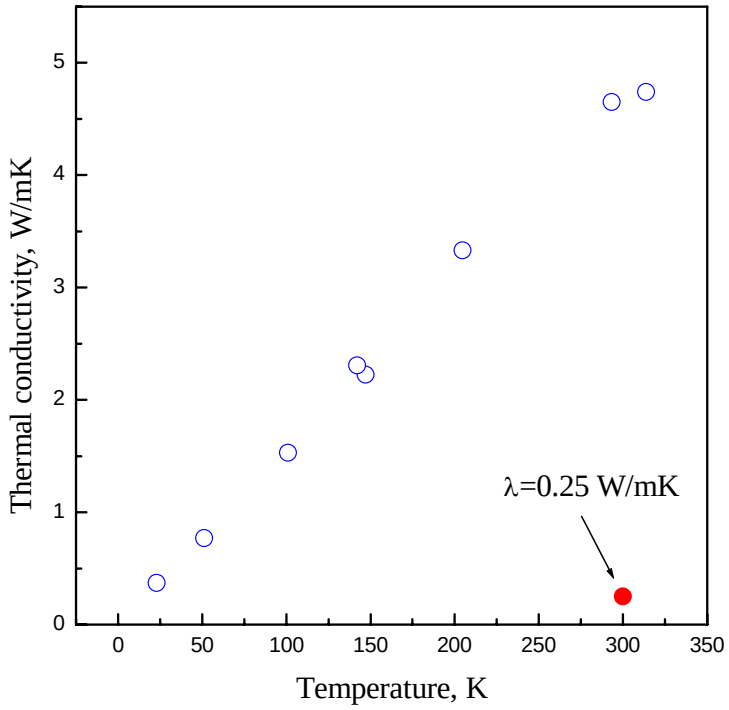

Figure 2.18: Temperature dependence of thermal conductivity of MEH-PPV conjugated polymer reinforced by 2% SWNT. Open circles shows the heat flow along the film and solid circle corresponded to the thermal conductivity perpendicular to the film surface.

The concentration dependence of the thermal conductivity perpendicular to the MEH-PPV film surface is shown below (Figure 2.19). The considerable enhancement of the thermal conductivity is much below expectations, however, perhaps because of poor distribution of SWNT in MEH-PPV matrix.

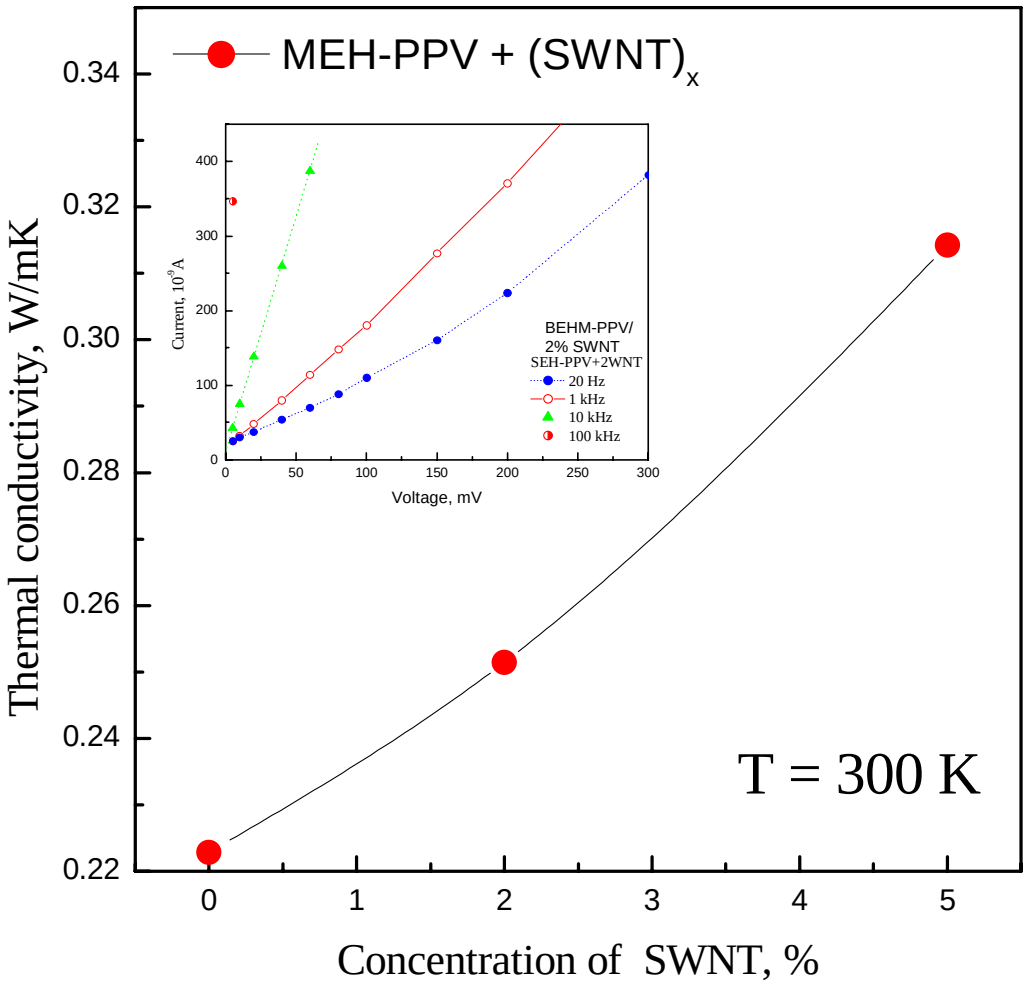

Fig. 2.19: Concentration dependence of thermal conductivity of MEH-PPV + SWNT composite. Insert shows the I-V curve for MEH-PPV +2% SWNT composite.

The high frequency dependence of the electrical conductivity shown in the insert indicates the non-ohmic interconnection between carbon nanotubes. The agglomeration and non-ohmic contacts are the main reasons causing the low thermal conductivity of the studied composites.

Chapter 3: CHARACTERIZATION AND OPTIMIZATION OF PHONON SPECTRA, THERMAL CONDUCTIVITY AND SUPERCONDUCTIVITY

3.1. Thermal Conductivity Measurements on Nanocomposites with CNTs

3.1.1. Comparative method in PPMS

To eliminate the heat losses through lead wires the comparative method was used for thermal conductivity measurements of thin CNT fibers and films. The PPMS (Quantum Design) Thermal Transport circuit was modified for the comparative method as shown in the schematic diagram below (Fig.3.1).

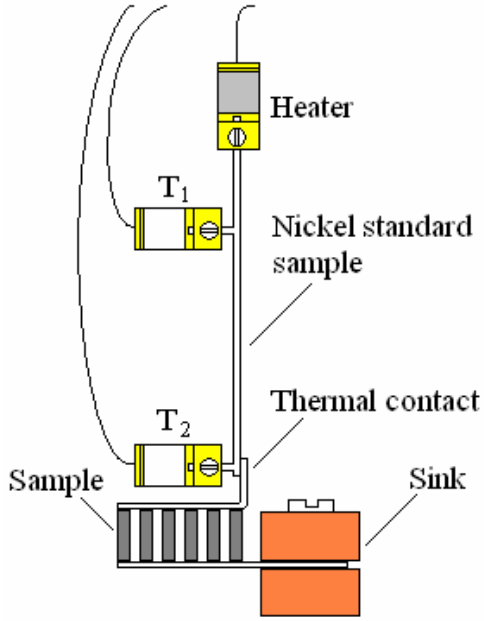

Fig.3.1: Schematic diagram of sample connection for comparative measurement of thermal conductivity using the nickel standard sample.

This method is a variation of the methodology commonly known as the cut-bar technique. In the cut-bar technique, a specimen of unknown thermal conductivity is sandwiched between two pieces of material with known thermal conductivity using a thermal grease and a pliable metal foil to eliminate interfacial thermal contact resistance between the materials. Thermocouples placed along the lengths of the three material pieces yield information on the rate of heat flow through the two reference-material sections of known conductivity. The heat-flow rate can then be used to determine thermal conductivity of the unknown specimen using the one-dimensional Fourier conduction equation:

$$Q = \lambda A \, dT/dx \qquad (3.1)$$

where Q is the rate of heat flow, λ is the thermal conductivity, A is the cross-sectional area through which the heat flows, and dT/dx is the temperature gradient. Experimentally, dT is approximated by ΔT, the finite temperature difference, and dx is approximated by Δx , the distance over which the temperature difference is measured.

In our measurement method, only one section of known material is used. Assuming that the heat flux through both samples and the Ni-standard is the same, the thermal conductivity of the unknown sample, λ_s can be calculated as:

$$Q_s = Q_R = \lambda_s A_s (\Delta T_s / L_s) = \lambda_R A_R (\Delta T_R / L_R). \qquad (3.2)$$

$G = \lambda A/L$ is the sample conductance.

The thin SWNT fibers shown in Fig.3.2, in comparison with human hair, were arranged in parallel stack to enhance the sample conductance (see Fig.3.3). The fibers were glued to gold covered copper leads by silver filled epoxy H20E (EPO-TEK) [1]. The four probe assembly shown in Fig.3.3.

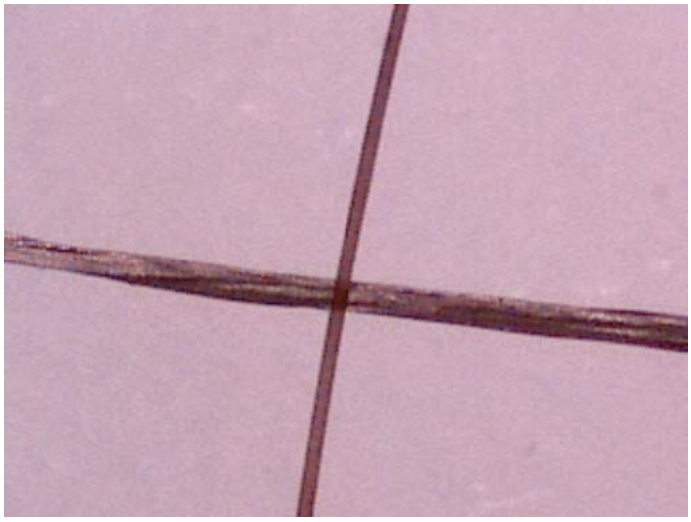

Fig.3.2: Bunch of 8 fibers prepared by coagulation method compared with human hair (vertical). The PVA polymer concentration in bunch is 35%

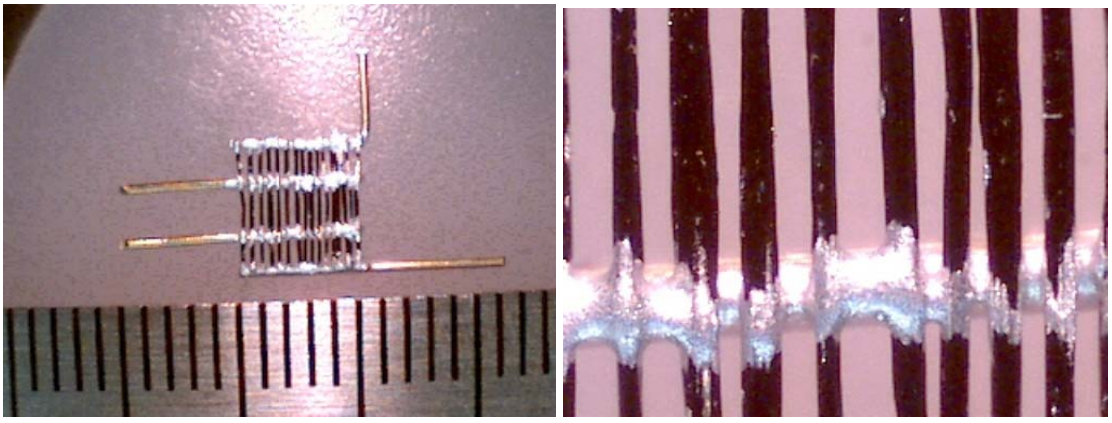

Fig.3.3: Four probe assembly of 16 fibers each comprising 8 fibers with 35% PVA.

References

[1] M.J. Hodgin. Conductive Adhesives for Thermal Management; Case Study Issues in Hybrid Microelectronics and Plastic IC Packaging. Proc. Of 28th Annual new England IMAPS Conference, Boxborough, MA., May8, 2001.

3.1.2. Tunable thermal conductivity in carbon nanotube paper

Phonon transport in one-dimensional (1D) nanostructures such as carbon nanotubes has recently received a lot of attention. The very high thermal conductivity (10,000 W/m·K) predicted theoretically for single tubes [1.2] was not achieved experimentally. Due to the phonon-phonon interaction between carbon nanotubes, the measured thermal conductivity of a collection or a mat of carbon nanotubes was found to be much lower than predicted [3].

In disordered SWNT 'mat' samples, the room temperature thermal conductivity is only 35 W/m·K [3]. However, in samples consisting of aligned SWNTs, the room-temperature thermal conductivity normalized to crystalline nanotube arrangement is above 200 W/m·K [4]. On the other hand, the thermal conductivity of a 14 nm diameter multiwall carbon nanotube (MWNT) measured by a microfabricated device [5] was about 3000 W/m·K at room temperature, which is in close agreement with the prediction value [1]. However the T^2 temperature dependence suggests that MWNT behaves rather like a 2D system thermally. The very important result of this work, for our investigation, is a decrease in thermal conductivity with an increase in the number of nanotubes in the bundle: an 80 nm diameter MWNT bundle has the thermal conductivity of about ~1200W/m·K, and a 200 nm diameter MWNT has about ~300 W/m·K respectively. The decrease mentioned above, compared to thermal conductivity in single nanotubes, is a consequence of a phonon-phonon interaction leading to the rise of umklapp processes between interconnected nanoubes in bundles or mats.

In this part of the project, we will show that charge injection in carbon nanotube bundles in bucky paper will decrease the phonon-phonon interaction between carbon nanotubes by increasing the nanotube separation as was predicted in theoretical part 1.

3.1.2a Experiment

1. *Techniques*

To measure the change in thermal conductivity, the laser flash method was chosen to measure the thermal diffusivity along a carbon nanotube paper. Thermal diffusivity *D* relate to the thermal conductivity λ by a simple equation,

$$\lambda = \rho \cdot C_v \cdot D, \qquad (3.3)$$

where ρ is the density and C_v is the heat capacity.

The design of laser flash method is very appropriate for *in situ* measurements and *D* is the most sensitive parameter, in (3.3, to structural changes in medium with low heat capacity

and density. A schematic view of the laser flash method used in this study is shown in Fig. 3.4.

A 135 mW IQ series laser module from Power Technology Inc., operated together with a build-in modulator or chopper (model SR540 with Chopper Controller), radiate a 2 mm diameter modulated beam with 830 nm wavelength. The laser beam is focused onto the sample with 50 mm focal length lens (or cylindrical lens for wide strip). The sample is mounted between two gold standoffs on a ceramic sink. The heated spot is adjustable so that it can be made occur at any position on the front surface of the prolonged specimen by using three-axis translation stages to move the sample holder (or the vacuum cryostat) together with the specimen. The periodic heating technique can provide two independent methods: frequency-variation method when the position of the heated spot is fixed just opposite to the sensing point and only the modulation frequency is changed and distance-variation method when the modulation frequency is fixed and the distance between the heated spot and the sensing point is changed. In the present study we are using distance-variation method.

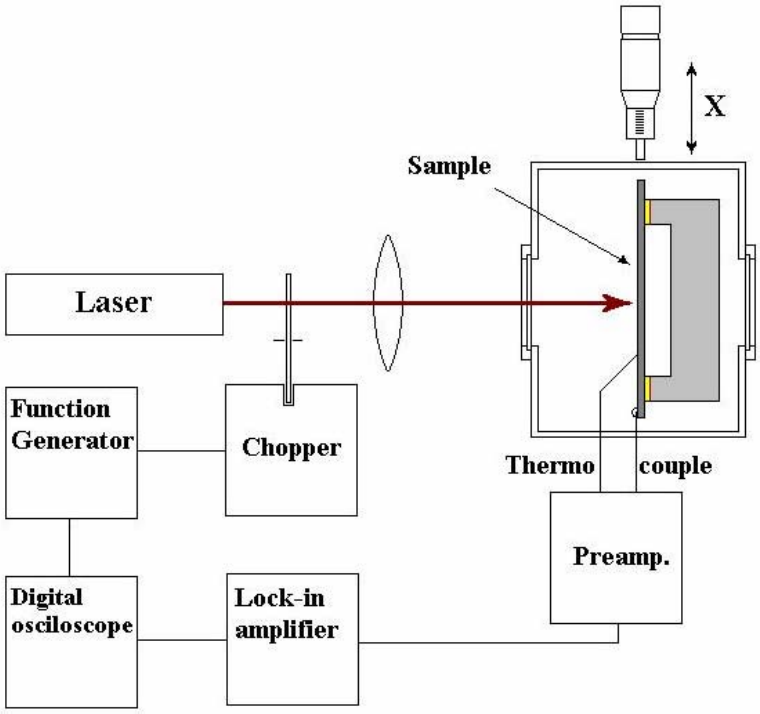

Fig.3.4: The instrumentation of laser flash technique used to measure the thermal diffusivity of SWNT bucky paper.

The measurements are made by changing the distance *x* between the fixed thermocouple tip and the laser spot in stationary conditions. This means that each measurement is done when the temperature distribution has reached its steady state and no dynamical problems arise. In our case, because of very thin and narrow bucky paper strip and very sharp thermocouple tip (d<10μm), the relaxation time was less then 1s. To reduce the thermal inertia of thermocouple we used only one (constantan) wire with additional chemical treatment. The tip of 75μm constantan wire was etched by 50% HNO_3 water solution by dipping 1 mm end in solution for 1 min. The resulted tip diameter was less then 10μm. The other wire of thermocouple is the studied carbon nanotube strip.

The thermoelectrical signal from thermocouple constantan/carbon nanotube is amplified with Tektronix differential preamplifier ADA400A with tunable band. Then the resulted signal compared with reference signal from Agilent functional generator 33220A to obtain the phase delay between two periodic signals with the same frequency: heat source signal modulated with generator 33220A and signal of thermocouple tip outstanding on distance *x*. The phase delay is read from the display of lock-in amplifier SR540 and the magnitude of thermal signal from the two channel digital storage oscilloscope Tektronix TDS 2002.

If we have a periodic point heat source which liberates heat at the rate $I_o exp(i\omega t)$, the temperature on a line at distance *x* from the heated point is related to the temperature *T(x=0)* by

$$T(x) = T(0) \cdot exp(-x/l_t) \qquad (3.4)$$

where l_t is the thermal diffusion length. The ratio of the two moduli *M* of the thermal signals taken along the lines at *x=0* and *x* is

$$M(x)/M(0) = 2\ exp(-x/l_t), \text{ or } \ln\frac{M(x)}{M(0)} = \ln(2) - x\sqrt{\pi f / D} \qquad (3.5)$$

and the phase φ of the thermal signal on the distance *x* is $\varphi = -x(\pi \cdot f/D)^{1/2}$, where *f* is the frequency of modulation of the laser beam intensity and *D* is the thermal diffusivity.

The calibration on the thin gold wire using phase shift measurement via distance shows very linear dependence and excellent agreement of thermal diffusivity, *D*=128.9 mm^2/s with the data presented in the literature, *D*=130 mm^2/s, [6]. However for CNT paper we have to take into account the high surface area and radiation losses.

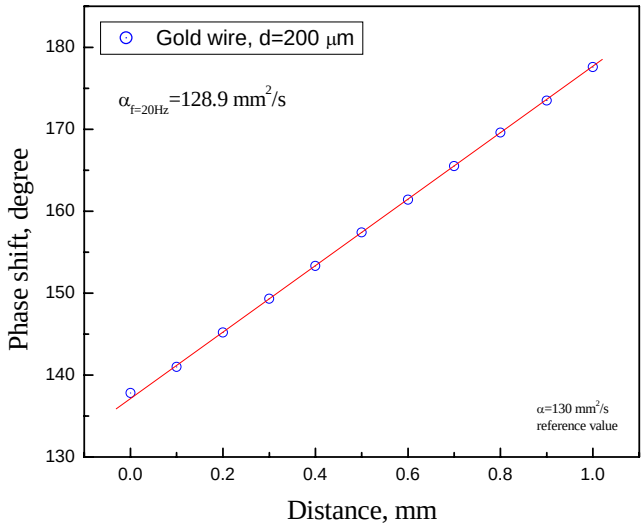

Fig.3.5: Phase shift of thermal signal chopped with the frequency 20 Hz as a function of offset between laser beam and thermocouple tip.

2. *Charge Injection*

Small diameter lithium or sodium ions seem to be ideal for ion insertion between nanotubes. 1M NaCl aqueous solution and platinum counter electrode was used to charge a

thin bucky paper strip (20x 0.5x 0.035 mm^3) in cronoamperometry regime on CHI 660B Electrochemical Station. The positive (Cl^-) or negative (Na^+) charges with current 0.1 mA was applied to CWNT strip during 1h at 0.8V. Than the sample was washed in DI water and dried in vacuum during 4 h.

3. *Results and discussion*

a. HipCO:

First, we measured the thermal diffusivity of bucky paper consisting of HipCo SWNT. Fig.3.6 shows the phase shift of the thermal signal collected at different distances. To make sure that dipping in electrolyte solution and washing in DI water do not change the thermal properties of bucky paper, we first carried out the test measurement shown by green solid circles.

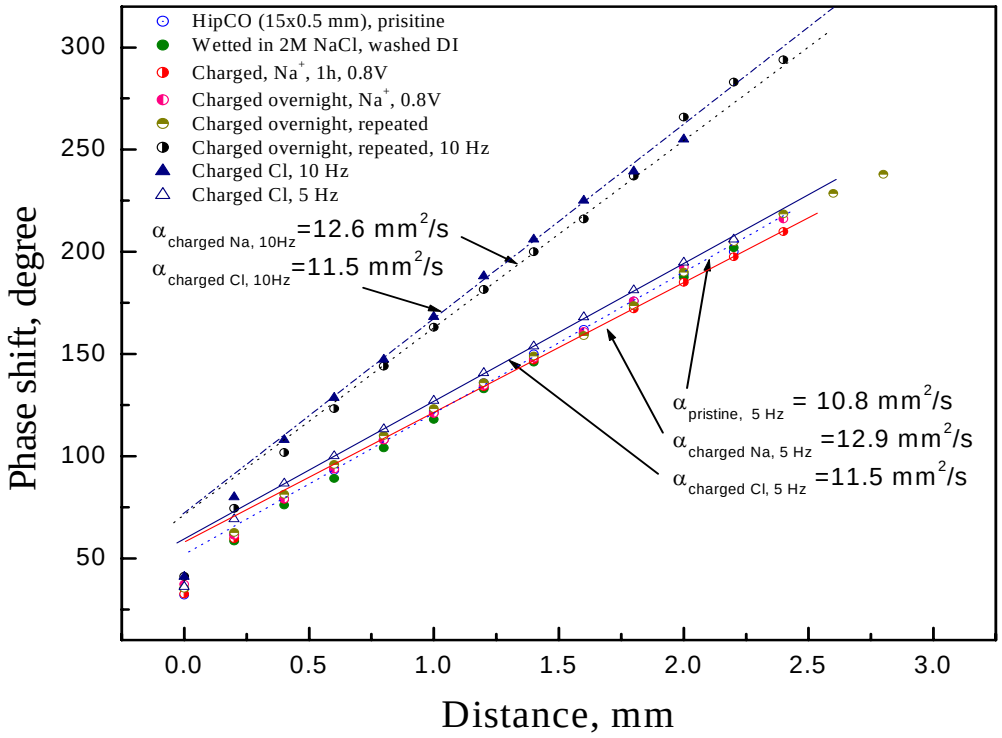

Fig.3.6: Thermal diffusivity of bucky-paper on the base of HiPCO SWNT.

b. Magnetically aligned bucky paper:

Magnetically aligned SWNT paper was obtained from National High Magnetic Field Laboratory in Florida, USA. SWNTs prepared by laser ablation technique at 1100^o C, were purified and deposited by vacuum filtration from water suspension under high magnetic field, 17T.

To overcome the dominant role of contact resistance in SWNT bucky-paper, multiple attempts were made to align disordered bunches. It is supposed that increasing the paper

density (and consequently contact surface area) and increasing the number of contacts in the alignment direction will increase the conductivity of the oriented paper significantly. Below, in Fig.3.7, the temperature dependence of resistivity for magnetically aligned "laser" SWNT bucky-paper is shown.

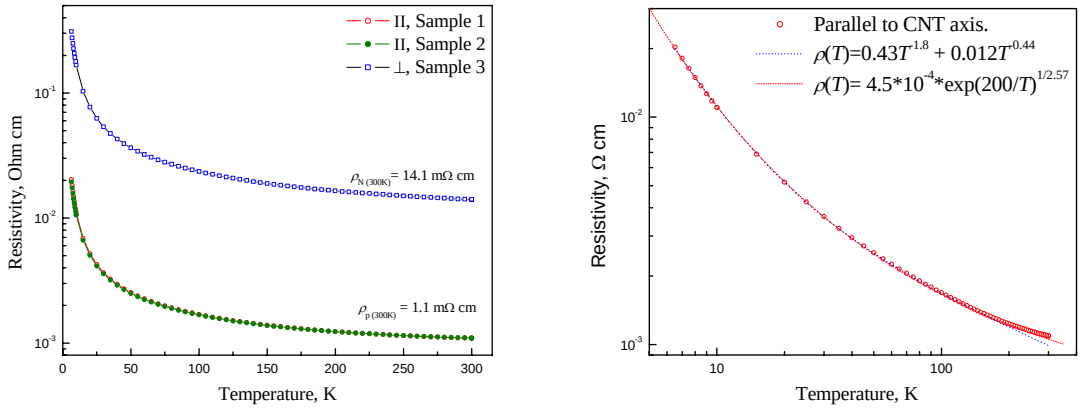

A **B**

Fig.3.7: A. The temperature dependence of conductivity of magnetically aligned SWNT bucky-paper, measured along and across alignment direction by four-probe method. The dimensions for sample 1: 15x1x0.012 mm^3, the distance between potential electrodes is 10 mm; samples 2 and 3 have length 10 mm, distance between potential electrodes 8 mm.
B. The temperature dependence of conductivity along the nanotube alignment direction. The fitting by Luttinger liquid and VRH models shown by dashed and dot lines, respectively.

Anisotropy of resistivity of $R_{perp}/R_{par} \approx 14$ is temperature independent. *R(T)* curves for samples 1 and 2 with different distance between electrodes actually have coincided. Analysis of temperature dependence of resistivity *($R_{par}(T)$)* in the framework of VRH model leads to following expression (see Fig.3.7 B),

$$R(T) = 4.5\cdot10^{-4}\cdot\exp(200/T)^{1/2.57} \qquad (3.6)$$

where the conductivity dimensionality has shifted toward a two-dimensional system. Such behavior of *R(T)* could be explained by the increase in contact area for the aligned CNT. However, it is important to mention that magnetically aligned samples were produced from "laser" SWNT. It is recognized that "laser" SWNT is less defective.

The lowering of T_o and new temperature dependences of hoping conductivity, $lnR \sim (T_o/T)^{2/5}$ was predicted in [23] for one-dimensional conductors with reduced concentrations of defects [26]. Decreasing the concentration of defects, keeps the hopping mechanism in rare short clusters, dissolved in long channels of one-dimensional conductors. However for the system of one-dimensional conductors, the weak excitations of the charge density now leads to the linear Coulomb gap with high shielding anisotropy of the Coulomb potential.

Fig.3.8 shows the thermal diffusivity measurement of magnetically aligned bucky-paper.

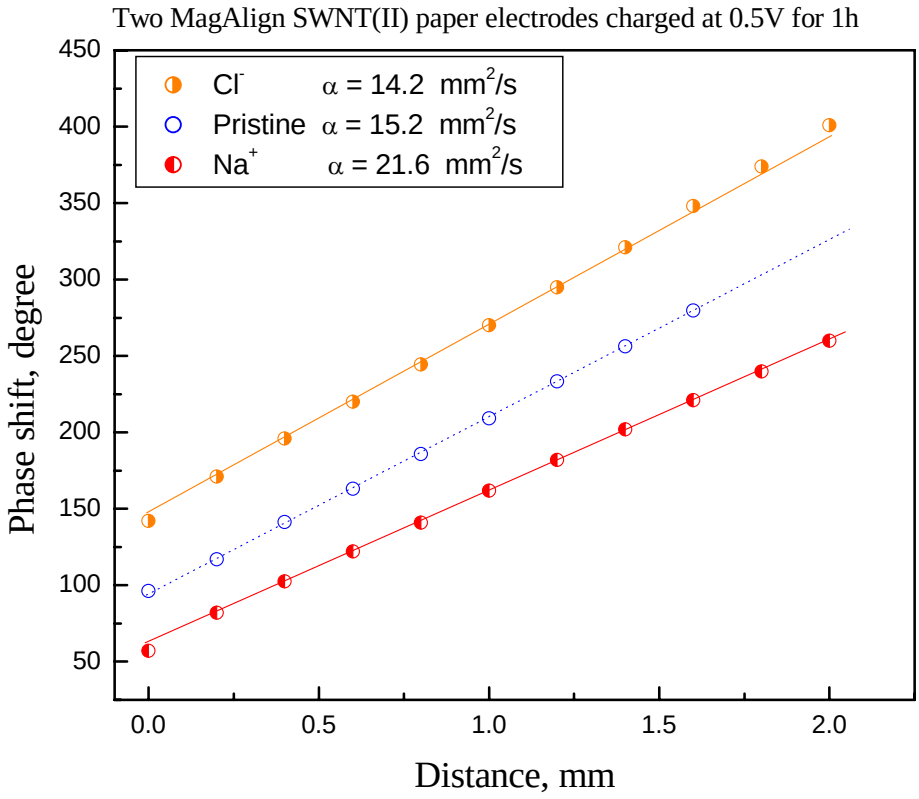

Fig.3.8: Thermal diffusivity of magnetically aligned bucky-paper.

3.1.3 References

[1] S. Berber, Y.-K. Kwon, and D. Tomanek, Phys. Rev. Lett. 84 (2000) 4613.

[2] M. A. Osman and D. Srivastava, Nanotechnology 12 (2001) 21.

[3] J. Hone, M. Whitney, C. Piskoti, and A. Zettl, Phys. Rev. B 59 (1999) R2514.

[4]J. Hone, M.C. Llaguno, M.J. Biercuk, A.T. Johnson, B. Batlogg, Z. Benes, J.E. Fischer. Appl. Phys. A 74 (2002) 339–343.

[5]P. Kim, L. Shi, A. Majumdar, and P. L. McEuen, Phys. Rev. Lett. 87 (2001) 215502.

[6] J.H. Barkyoumb, D.J. Land, Thermal diffusivity measurement of thin wires usin photothermal deflection. J.Appl.Phys. 78, 2 (1995) 905-912.

3.2. Thermal Conductivity of Thin-wall Carbon Inverse Opal

In the last decade, a new material called photonic crystal (PC) has attracted much attention from both basic and applied science viewpoint. The behavior of photons in PCs is very much like that of electrons in semiconductors [1, 2]: the photonic band structure may show forbidden gaps in which photons cannot exist. Therefore, many of the devices and concepts based on the band gap phenomena may be extended to PCs.

This novel concept was developed for various new applications of PCs such as threshold-less lasers and optical transistors [3]. However, the obstacles to obtain this kind of PCs with a complete gap in the desired spectral region represent a big challenge. PCs can be defined as mesoporous materials with a periodic distribution of submicrometric pores. Mainly, there are two parameters that determine the existence of a photonic gap. First, the refractive index contrast, defined as the ratio between the refractive indices of the material and the surrounding substance; secondly, the filling fraction, defined as the percentage volume occupied by the voids, is a very important parameter. Also, the topology of the structure will be decisive in explaining the band structure.

Among the various preparation methods of three-dimensional periodic structures, a self-assembly method utilizing sedimentation of monodispersed nanoscale spheres is the simplest. Silica opal is a type of naturally occurring photonic crystal that consist of well-ordered three dimensional arrays of SiO_2 spheres, which have diameters in the wavelength range of visible light [4]. As a consequence of periodicity they show opalescence colors that come from Bragg diffraction by the periodic distribution of particles. Bragg diffraction constitutes the fingerprint of photonic band gap (PBG) properties. However, theory predicts that inverse opals would show much better PBG properties than direct opals. Inverse opals that can be regarded as the negative replica of opals, have a well-ordered array of nanometric spherical cavities surrounded by a high refractive index material, in which both the cavities and the high refractive material is connected throughout the structure. To achieve a complete PBG, many laboratories are trying to fabricate high quality inverse opals with high contrast and filling factor [5-10].

At the same time, the unusual mesoscopic structure of the synthetic opal attracted a large effort to improve the efficiency of thermoelectric materials [11, 12]. A good thermoelectric material has low thermal conductivity κ, high electrical conductivity σ, and a high Seebeck coefficient, in order to maximize the thermoelectric figure of merit,

$$Z = \sigma S^2/\kappa \qquad (3.7)$$

where Z has units of inverse absolute temperature and is generally quoted as ZT.

For more than 40 years, the search for better thermoelectrics has not provided a material with ZT significantly larger than one. ZT of about four would make thermoelectric coolers able to compete with gas-compression technology. Assuming that the Seebeck coefficient in opal where silicon spheres replaced by thermoelectric materials will not affected by the opal structure, if the thermal conductivity is reduced much more than the electrical conductivity, the opals could be useful thermoelectric materials. Unfortunately many experimental works [7,13,14] and theoretical calculations [15] show that the overall reduction for electrons and phonons in synthetic fcc opal structures will be the same.

On the other hand such porous and highly ordered materials as inverse opals open up new opportunities for further development of multifunctional nanodevices. Particularly, at the low filling factor usually achieving by infiltration of pores by sol-gel route or Chemical Vapor Deposition (CVD), inverse opals have two independent nets of pores divided by a very thin shell: one resulting from removing SiO_2 spheres and the other consists of octahedral and tetrahedral pores reduced by thin wall covered on SiO_2 spheres but still with interconnected windows. Both nets could be tuned independently: first net by changing the SiO_2 sphere size, second net by filling factor. Moreover, at some condition they could be filled by functional materials divided by shell material.

In this part of the project we study the behavior of the heat flow through thin-wall carbon inverse opals produced by two different methods.

3.2.1. Experiment

Porous silica opals were used as templates for infiltration and carbon inverse opal synthesis as described in detail by Zakhidov *et al* [7,8,16]. Briefly, the carbon inverse opals were fabricated by infiltrating silica opal with a phenolic resin, thermally curing this resin at low temperature, dissolving the SiO_2 from the infiltrated opal with aqueous HF, and pyrolyzing the resulting phenolic inverse opal at progressively increased temperatures up to 1000^oC. The graphitic carbon inverse opal was fabricated by CVD method using 1:3 molar ratio of propylene and N_2 as the feed gas followed by silica removal with aqueous HF.

Thermal and electrical conductivity measurements were performed using Quantum Design Physical Properties Measurement System (PPMS). For these measurements for both inverse opals two samples with different geometry ($4.5x1.8x12\ mm^3$ and $6.0x2.0x17\ mm^3$) and lead distance (6 and 10 mm) have been prepared. The gold covered copper leads were glued to sample by silver filled epoxy H20E (EPO-TEK) using four-probe design: heater - thermometer T_1 - thermometer T_2 - sink. To eliminate the thermal radiation "tail" in the thermal conductivity data, usually appearing at high temperatures, the thermal conductivity measurements above 200 K were confirmed by comparative method involving the series connection of Ni-standard and studied samples. The electrical resistivity for some of samples was measured by a conventional four-probe method using Agilent HP4284A milliohmmeter. Heat capacity measurements were performed using Perkin Elmer Pyris Diamond DSC,. The surface and fracture image of inversed opal were examined by a JSM-1500 (JEOL, Japan) Scanning Electron Microscope (SEM).

3.2.2. Results and discussion

1. *Structure*

Fig.3.9 shows SEM images of cleft edges of (001) and (111) facet of the thin-walled inverse opal lattice (250 nm spheres). For both glassy carbon inverse opal fabricated by a phenolic route and graphitic carbon inverse opal fabricated by CVD route a highly periodic structure throughout the volume have been obtained. The void structure consists of an FCC arrangement of spherical carbon shells interconnected with 12 neighboring spherical shells via windows, which result from the sintering process.

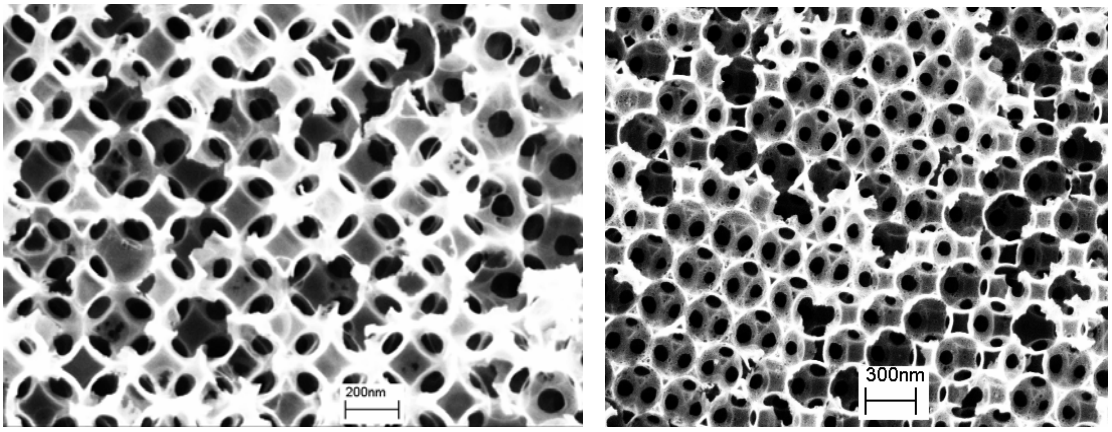

Fig.3.9: The (100) and (111) planes of surface-templated inverse opal. The rough appearance of a cleaved edge of carbon infiltrated inverse opal is due to the occurrence of fracture through hollow spheres (rather than between spheres in silica opal). The large windows interconnecting the spherical cavities are due to the sintering of the opal template.

2. *Thermal conductivity*

The temperature behaviors of thermal conductivity of both inverse carbon opals are almost similar: the linear increase at low temperatures shown in the insert of Fig.3.10 illustrates the changed slope at 20 K and the slight exponential growth above 75 K. The difference in absolute value of about 20% obtained for the whole measured range may be attributed to the difference in crystalline structure of the shells. The X-ray diffraction spectra show the higher crystallinity for CVD infiltrated samples. Moreover, SEM and TEM electron micrographs [7] indicate that the thin wall shells consist of graphite sheets that are preferentially oriented parallel to the void surface created by removal of the SiO_2 spheres.

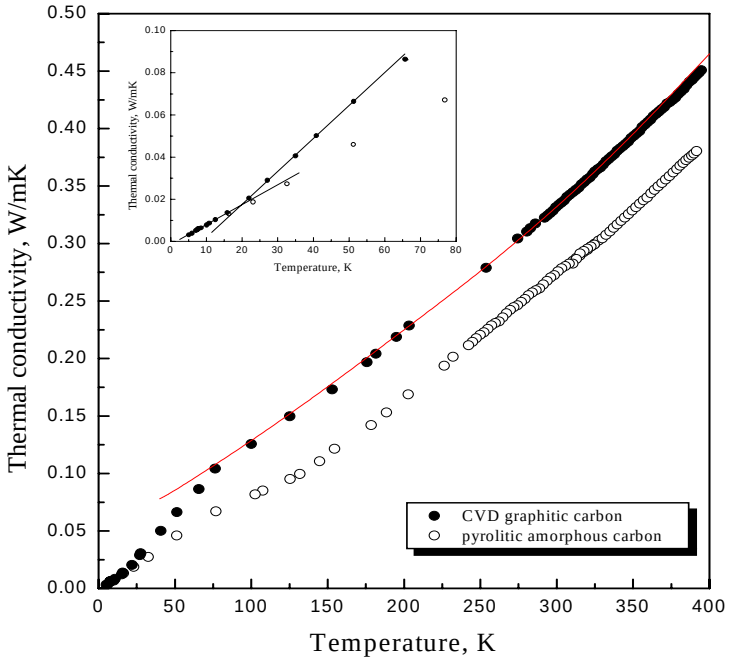

Fig.3.10: Temperature dependence of thermal conductivity of graphitic carbon (CVD) and glassy carbon (pyrolitic amorphous carbon) inverse opals.

Effective thermal conductivity. **There are a lot of approaches to calculate the thermal conductivity of porous materials and composites using the known thermal conductivity of the parent material. Within a continuum description, the effective thermal conductivity of a composite with spherical voids (*d*=3) or infinite cylindrical voids (*d*=2) and the thermal conductivity of host material κ_o can be given by the following equation [17].**

$$\kappa_{eff} = \frac{(1-p)\kappa_o}{1+p/(d-1)}, \qquad \textbf{(3.8)}$$

where *p* is the fractional volume of the voids often called the "porosity".

Another equation, taking into account the thermal conductivity of the material in pores, κ_{pores} [18] were used in [19,20] for the FCC opal,

$$\frac{\kappa_{eff}}{\kappa_o} = (1-p)\sqrt{1-p} + p^{\frac{1}{4}}\nu, \qquad \textbf{(3.9)}$$

where $\nu = \kappa_{pores}/\kappa_o$.

The continuum approach to study the effective thermal conductivity of periodic composites was examined by Albrecht *et al* [21] for a number of two-dimensional and three-dimensional lattices.

3. *Porosity*

To calculate the effective thermal conductivity, we have to first estimate the porosity of the structure. The schematic representation of the face-centered cubic structure of inverse opal is given below.

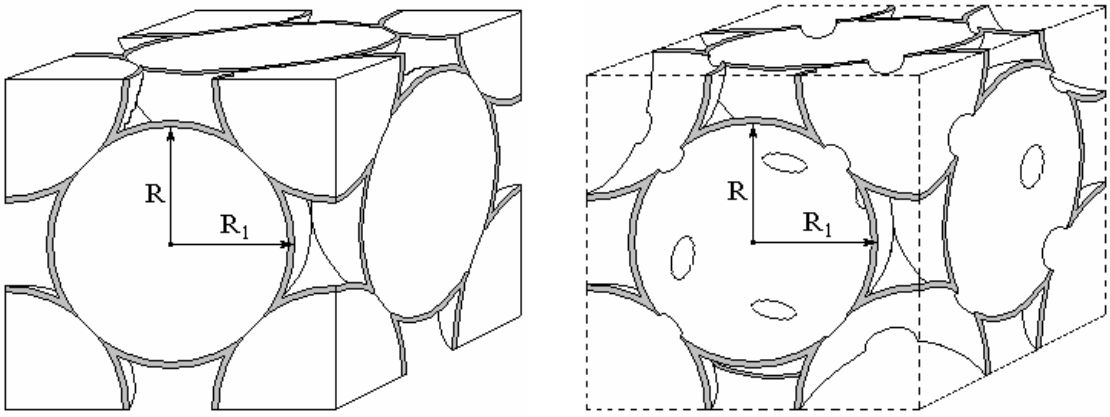

Fig.3.11: Schematic representation of surface-templated inverse opal.

The volume of the FCC structure unit is $V_{cub.} = (2\sqrt{2}\cdot R)^3 = 16\sqrt{2}\cdot R^3$, where R is SiO_2 sphere radius. The unit comprises four spheres with volume $V_{sphere} = 4\cdot (4/3)\cdot\pi\cdot R^3 = (16/3)\cdot\pi\cdot R^3$. For an opal structure we can find the commonly used filling factor F value, $F = V_{sphere}/V_{cub.} = \pi/3\sqrt{2} = 0.74$. For surface-templated inverse opal, the cubic volume filled only with thin shells of thickness $h = R_1 - R$, depends on filling conditions (Fig.3.11).

For the sample presented in Fig.3.9, D = 250 nm, and the average layer thickness is h = 10 nm. The volume of an empty sphere is, $(4/3)\pi R_1^3 - (4/3)\pi R^3 = 0.26(4/3)\pi R^3$, where R_1 was shifted by $1.08\cdot R$, $R_1 = ((R+h)/R)R = 1.08R$. The filling factor for surface-templated inverse opal is $F = 0.74\cdot 0.26 = 0.192$, and the porosity is $P = 1 - F = 0.808$.

In this calculation, we neglected the structure shrinkage at the first sintering which provided the intersphere interconnection through which the SiO_2 spheres were removed after infiltration, and we neglected the volume of these circular interfaces (12 holes per each sphere). Subtraction of the volume of 24 holes with average diameter 76 nm results in a reduction of the filling factor to 0.191. Consequently, P = 0.809.

Now we can calculate the thermal conductivity of the material of the shell (for graphitic carbon). At room temperature (T=300 K), κ_{effect} = 0.33 W/m·K (Fig.3.10). Considering that sphere voids and interstitials air filled, for (3.9 we can write,

$$\kappa_o = \frac{\kappa_{effect}}{(1-P)^{3/2}} = 3.95 W/mK \qquad \textbf{(3.10)}$$

By Albrecht approach for $\kappa_{pores}/\kappa_o = 0$ (air filling) giving $\kappa_{eff.}/\kappa_o = 0.09$ for thermal conductivity of shell material, we found very close result, $\kappa_o = 3.67$ W/m·K.

The density of measured samples is 0.22 g/cm^3. Taking into account the porosity of the studied inverse opal structure, P=19.1%, we calculate the density of the host material to be ρ = 1.15 g/cm^3 which is twice less than the density of crystalline graphite, ρ_c = 2.21 g/cm^3. Perhaps this difference is due to the porosity of the graphite layer and the extended diameter of interconnected windows appeared for the volume change at pyrolysis.

The schematic representation of graphitic shell structure in Fig.3.12 shows that for materials with high anisotropy of conductivity, both electric and thermal, the conducting path would be strongly dependent on the anisotropy factor: $\gamma = \kappa_{II}/\kappa_{\perp}$. For pyrolytic graphite at room temperature γ = 342 [22]. Heat flow from one sphere to another occurs only perpendicular to graphitic layers with thermal conductivity 5.7 W/m·K. As far as heat transferred to the surface layers of another sphere the high thermal conductivity along the graphitic layers, 1950 W/mK, shorts the heat flow near the sphere surface preventing further penetration of heat to deeper layers. In such structures, the thermal conductivity would be independent of the thickness of shell walls.

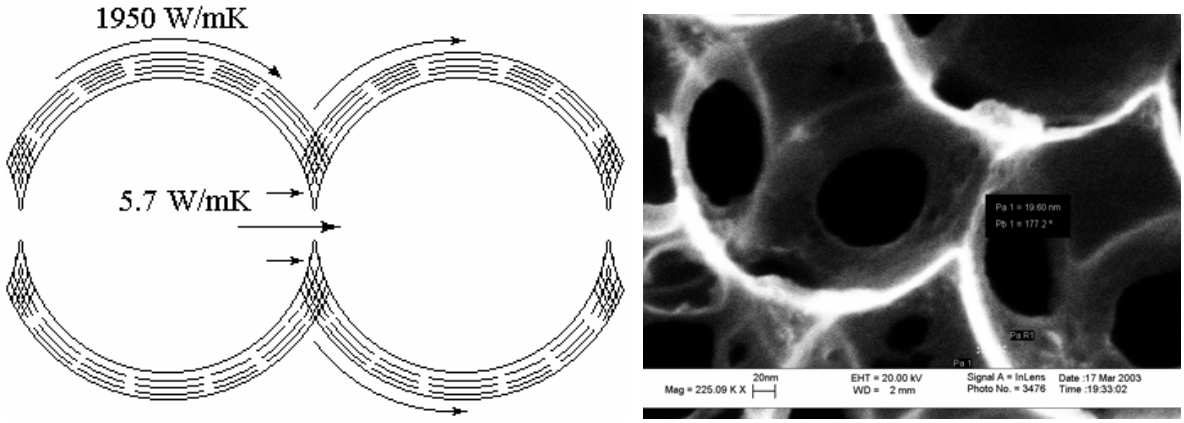

Fig.3.12: Schematic representation of heat flow through graphitic shell structure and real structure of interconnecting windows.

Electrical conductivity. **Since graphite has a high electronic conductivity, let us estimate the electronic contribution to the thermal conductivity using the Wiedemann-Franz law:**

$$\kappa/\sigma = LT \qquad (3.11)$$

where $L = 2.45 \cdot 10^{-8}$ W·Ohm/K^2 is Lorenz number.

The temperature dependence of specific resistivity of the studied inverse opal, measured by two-probe and four-probe methods, is shown in Fig.3.13. The slope of the curve is in good agreement with the data for crystalline graphite for this temperature region [23] and for carbon inverse opals with high filling factor studied in [8,24] for various heat treatment temperatures. However, the absolute value of resistivity for our inverse opals heat treated at 1000^{o}C is much lower than those obtained in [8,24]. The anisotropy factor for electrical conductivity in highly crystalline graphite is much higher than for thermal conductivity, $\gamma_e = 0.5(\Omega \cdot cm) / 0.5 \cdot 10^{-3}$ $(\Omega \cdot cm) = 10^3$ [23]. The obtained resistivity of graphitic inverse opal normalized to porosity is in good agreement with a resistivity of crystalline graphite across the graphite layers. This result shows excellent evidence that the transport properties of graphitic inverse opal are determined by the tiled structure of contacted area of the shells.

The electronic contribution to total thermal conductivity, $\lambda_{e(300K)} = 3.7 \cdot 10^{-3}$ *W/m·K,* is two orders smaller than the measured value, $\lambda_{(300K)} = 0.33$ *W/m·K.* However at low temperature, T<50K, the electronic contribution to the thermal conductivity could be predominant.

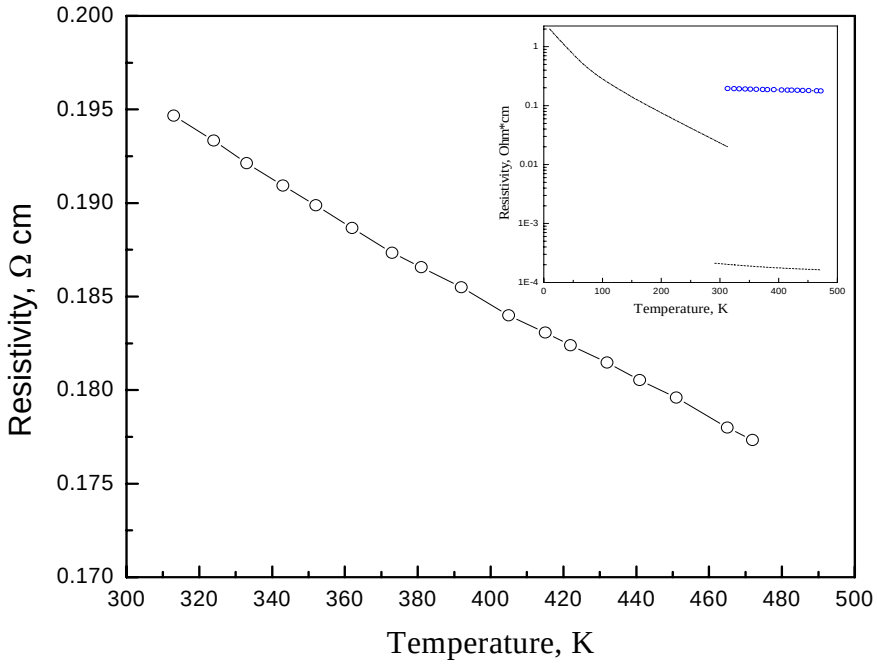

Fig.3.13: Temperature dependence of resistivity for the carbon inverse opal (carbon opal replica). The insert shows the comparative behaviour of resistivity for studied inverse opal (open circles), phenol replica with high filling factor, heat treated at 830°C [24] (dash-dot line), and POCO graphite[23].

Heat capacity. **The temperature dependence of the specific heat capacity of graphitic inverse opal is shown in Fig.3.14. Within the measured temperature range the heat capacity exhibits the smooth rise closely resembling the 2-3D behavior of of bulk planar graphite (solid line) [23]. For comparison the specific heat capacity values of POCO graphite [23] was divided to the density ratio $\rho_{POCO}/\rho_{invers\ opal}$= 1.82 g/cm^3 / 0.22 g/cm^3.**

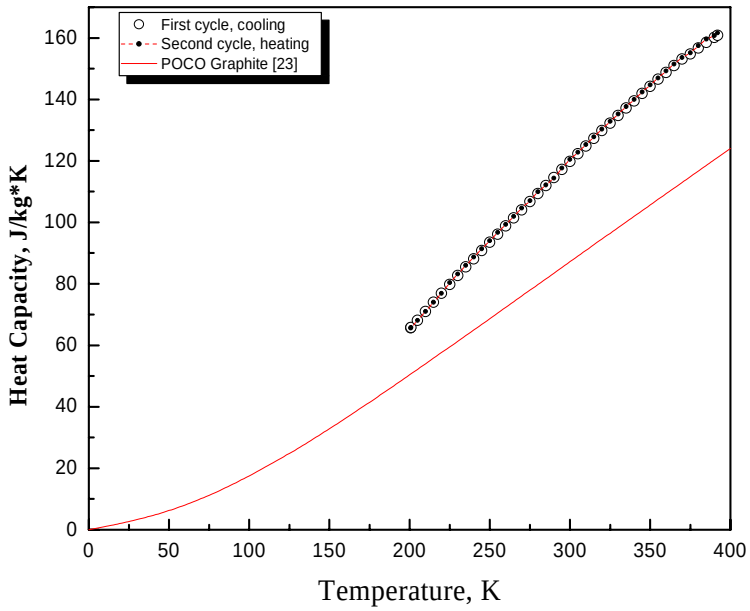

Fig.3.14: Temperature dependence of specific heat capacity, C_p of graphitic inverse opal prepared by CVD method. C_p *vs* T for pyrolitic POCO graphite was normalized to the density of studied inverse opal, (1.82 g/cm^3 / 0.22 g/cm^3).

3.2.3. Conclusion

We measured the thermal conductivity of carbon inverse opals with different crystallinity of the infiltrated carbon. The obtained thermal conductivity in both samples is extremely low, 0.33 *W/m·K*. The conducting path is strongly dependent on the anisotropy factor: $\gamma = \kappa_{II} / \kappa_{\perp}$. For highly crystalline pyrolytic graphite (γ = 342) the heat flow from one spherical shell to another occurs only perpendicular to graphitic layers with thermal conductivity 5.7 W/m·K. These interconnecting interfaces determine the whole thermal conductance of the system. The heat transferred to the surface layers of another sphere is rapidly shorted by high thermal conductivity along the graphitic layers (1950 W/m·K) thus, preventing the further penetration of heat to deeper layers. In such structures, the thermal conductivity would be independent of the thickness of shell walls.

The electronic contribution to the thermal conductivity, $\kappa_{e(300K)} = 3.7 \cdot 10^{-3}$ *W/m·K*, is negligible compared to the measured value, $\kappa_{(300K)} = 0.33$ *W/m·K*.

The low thermal conductivity with an appreciably high electronic conductivity suggests the possible application for these materials in thermoelectric cells.

3.2.4 References

1. E. Yablonovitch, Phys. Rev. Lett. 58 (1987) 2059.

2. S. John, Phys. Rev. Lett. 58 (1987) 2486.

3. S. John, T. Quang, Phys. Rev. Lett. 78 (1997) 1888.

4. J.V. Sanders. Nature 204 (1964) 1151.

5. Yu.A. Vlasov, V.N. Astratov, O.Z. Karimov, A.A. Kaplyanskii, V.N. Bogomolov, and A.V Prokofiev. Phys. Rev. B, 55 (1997) R13357.

6. C. Lopez, et al., Superlattices Microstructure. 22 (1997) 399.

7. A.A. Zakhidov, R.H. Baughman, Z. Igbal, C. Cui, I.Khayrullin, S.O.Dantas, J.Marti, and V.G. Ralchenko, Science 282, (1998) 897.

8. K. Yoshino, H. Kajii, Y. Kawagishi, M. Ozaki, A.A. Zakhidov, and R.H. Baughman. Jpn. J. Appl. Phys. 38 (1999) 4926-4929.

9. Y.A. Vlasov, N. Yao, D.J. Norris. Advanced Mater. 11 (1999) 165-169.

10. A. Stein, R.C. Schroden. Current Opinion in Solid State and Materials Science. 5 (2001) 553-564.

11. T.M. Tritt, Science 283 (1999) 804.

12. F.J. DiSalvo, Science 285 (1999) 703.

13. R.H. Baughman, A.A. Zakhidov, I.Khayrullin, Z. Igbal, P. Eklund, and G.D. Mahan, in Opals and Replicas, Proc. of the XVII Int. Conf. on Thermoelectrics, Nagoya, Japan, edited by K. Kaumoto (IEEE, New York, 1998).

14. V. N. Bogomolov, L. S. Parfen'eva, A. V. Prokof'ev, I. A. Smirnov, S. M. Samolovich, A. Jezÿowski, J. Mucha, and H. Miserek, Fiz. Tverd. Tela, (St.Petersburg) 37 (1995) 3411, [Phys. Solid State 37 (1995) 1874].

15. J.O. Sofo, G.D. Mahan, Phys. Rev. B, 62, 4 (2000) 2780.

16. A.A. Zakhidov, I.Khayrullin, R.H. Baughman, Z. Igbal, K. Yoshino, Y. Kawagishi, S. Tatsuhara. NanoStructured Materials 12 (1999) 1089-1095.

17. J.C. Maxwell, A Treaties on Electricity and Magnetism (Dover, New York, 1954), pp. 435-441.

18. E.Ya. Litovsky. Izv. AN SSSR. Inorganic Materials, 16, 3 (1980) pp.559.

19. V.N. Bogomolov, D.A. Kurdyukov, L.S. Parfen'eva, A.V Prokof'ev, S.M. Smoilovich, and I.A. Smirnov, Fiz. Tverd. Tela (St.Peterburg) 39, 392 (1997) [Phys. Solid State 39, 341 (1997)].

20. A.E. Aliev and N.Kh. Akhmedjanova. Uzbek Fiz. Jurnal. 1 (1999) 373-379.

21. J.D. Albrecht, P.A. Knipp and T.L. Reinecke. Phys.Rev. B, 63, 134303 (2001).

22. CRC Handbook of Chemistry and Physics, edited by B.R Lide, 82nd edition, 2001-2002, pp.12-221.

23. R.E. Taylor, H. Groot. Thermophysical Properties of POCO Graphite. High Temperature – High Pressures, 12, 2 (1980) 147-60.

24. K. Yoshino, H. Kajii, Y. Kawagishi, M. Ozaki, A.A. Zakhidov, R.H. Baughman. Jpn. J. Appl. Phys. 38, 1 (1999) 4926-4929.

Chapter 4: SUMMARY AND CONCLUSIONS

4.1 Summary on Carbon Nanotubes

"Modest" applications of nanotubes for thermal management (like 100-200% increase for composites with low conductivity matrices) look quite feasible.
However, in order to evaluate prospects of more aggressive goals fully exploiting the claimed potential, much more research work is needed to provide a firm understanding of issues involved. Among the problems could be:

- **Details of the physics of individual tube behavior, especially the low-T regime**
- **Microscopic picture of intertube/interlayer interactions and scattering**
- **Microscopic study of contacts with various media (leads)**
- **Possibility of (self-) assembly of contacts and environments that would be beneficial to the therm. conductivity**
- **Optimization issues given the understanding achieved**

4.2 Conclusions on Thermal Conductivity Enhancement

1. Ph-Polaritons are found to contribute to K(T) of thin films, with T-peak.
Position of T-peak depends on W op, the line width of OP and the TO-LO splitting.

2. K(T) can be 10-20 times stronger than the conventional radiative contribution to K by free photons.

3. T-peak shifts to lowest T in microcavities (L ~ 1-10 mm), which can be used in cryogenic heat transfer.
4. To create a material with high enough polaritonic K(T) at RT, compared to the usual, phonon Kph one should create an organic material with OP at 1500-2000 cm-1, which has large oscillator strength. In organic materials Kph is usually low (< 0.1-1 W/mK), the Kpol can become a main contribution.

5. One candidate for polaritonic heat pipe, can be a doped fullerene film MxC60 in which giant oscillator strength S enhancement is found, which is quadratic in doping level x: S ~x2.

6. **The strong dependence of Kpol(T) on S(x) leads to tunability of K(T) by charge transfer and thus may be used in "polariton-transistors", in which K can be amplified by charging gate G.**

7. **Phonon-Polaritons can be used for "Polariton-lasers", which will emit monochromatic and coherent IR radiation, due to Bose-Einstein condensation in microcavity.**